

ACKNOWLEDGEMENT

I would like to thank Allah for giving me strength, capability and opportunity to do this work. My deepest appreciation goes to my thesis advisor, Dr.Mohamed Antar for his continuous help, encouragement, suggestions and constructive criticism throughout my thesis work. I am also greatly indebted to my thesis co-advisor, Dr.Maged El-Shaarawi for his continuous help, valuable guidance and advice.

I would also like to thank my thesis committee members, Dr.Syed Zubair, Dr.Habib Abual Hamayel and Dr.Esmail Mokheimer for their interest, encouragement, cooperation and for the knowledge I gained when I took courses with them during my MS.

Appreciation also goes to King Fahd University of Petroleum and Minerals for supporting this work and providing all literature and computer facilities.

I would also like to thank my parents and friends for their cooperation, patience and encouragement which they gave me through out my masters' degree.

CONTENTS

ACKNOWLEDGEMENT.....	i
CONTENTS.....	ii
LIST OF TABLES.....	vii
LIST OF FIGURES.....	viii
NOMENCLATURE.....	xvi
THESIS ABSTRACT (ENGLISH).....	xx
THESIS ABSTRACT (ARABIC).....	xxi
CHAPTER I	
INTRODUCTION.....	1
1.1 General.....	1
1.2 Scope of the Present Work.....	2
CHAPTER II	
LITERATURE SURVEY.....	4
2.1 Introduction.....	4
2.2 Fluid flow and Convection Heat Transfer over Spheres.....	4
2.3 Study of Entropy Generation.....	7
2.3.1 Entropy Generation for Internal flows.....	7
2.3.2 Entropy Generation for External flows.....	16

CHAPTER III

GOVERNING EQUATIONS.....	23
3.1 Introduction.....	23
3.2 Governing Equations.....	24
3.2.1 Governing Boundary Layer Equations.....	27
3.2.2 Boundary conditions.....	28
3.3 Deriving Entropy Generation Equation.....	31
3.3.1 Constant wall temperature case.....	32
3.3.2 Constant Heat Flux Case.....	33

CHAPTER IV

NUMERICAL REPRESENTATION OF THE GOVERNING EQUATIONS.....	35
4.1 Introduction.....	35
4.2 Numerical Grid.....	35
4.3 Finite difference representation of the derivatives.....	38
4.4 Finite difference representations of governing equations.....	39
4.4.1 Finite difference representation of meridional momentum equation.....	39
4.4.2 Finite difference representation of continuity equation.....	41
4.4.3 Finite Difference representation of energy equation.....	42
4.5 Finite difference representation of boundary conditions.....	43
4.6 Finite difference representation of the entropy generation equation.....	44
4.6.1 Uniform wall temperature case.....	44
4.6.2 Uniform heat flux case.....	45

CHAPTER V

SOLUTION METHODOLOGY.....	47
5.1 Introduction.....	47
5.2 Numerical Grid.....	48
5.3 Criteria for Convergence.....	49
5.4 Solution procedure.....	50

CHAPTER VI

RESULTS AND DISCUSSIONS FOR THE FORCED CONVECTION.....	54
6.1 Introduction.....	54
6.2 Range of different controlling parameters.....	54
6.3 Results for uniform wall temperature (Forced convection case).....	57
6.3.1 Meridional velocity profiles.....	57
6.3.2 Radial Velocity Profiles.....	62
6.3.3 Temperature Profile.....	62
6.3.4 Local entropy generation profiles.....	64
6.3.5 Local and overall average entropy generation profiles.....	73
6.3.6 Bejan number and Irreversibility Ratio.....	80
6.4 Results for uniform heat flux (Forced convection case).....	84
6.4.1 Meridional and radial velocity profiles.....	84
6.4.2 Temperature Profile.....	86

6.4.3 Local entropy generation profiles.....	88
6.4.4 Average entropy generation profiles.....	95
6.4.5 Bejan number and Irreversibility ratio.....	102
CHAPTER VII	
RESULTS AND DISCUSSIONS FOR MIXED CONVECTION.....	107
7.1 Introduction.....	107
7.2 Uniform wall temperature Case (Mixed convection).....	107
7.2.1: Meridional and radial velocity profiles.....	108
7.2.2: Temperature profile.....	110
7.2.3: Local entropy generation profiles.....	110
7.2.4: Local and overall average entropy generation profiles.....	120
7.2.5 Bejan number and Irreversibility Ratio.....	125
7.3 Uniform heat flux Case (Mixed convection).....	127
7.3.1: Meridional and radial velocity profiles.....	127
7.3.2: Temperature profile.....	129
7.3.3: Local and overall average entropy generation profiles.....	131
7.3.4: Local and overall average entropy generation profiles.....	137
7.3.5 Bejan number and Irreversibility Ratio.....	142
CHAPTER VIII	
CONCLUSIONS AND RECOMMENDATIONS.....	146

8.1 Conclusions.....	146
8.2 Recommendations for future work.....	148
APPENDIX.....	149
REFERENCES.....	167

LIST OF TABLES

Table-6.1: Values of E_{c_m} for different combinations of Mach number and temperatures (for air)	57
Table A-1: Comparing Simplified and Un-Simplified entropy generation equation.....	166

LIST OF FIGURES

Fig 3-1a: Schematic diagram showing the boundary layer over a sphere (ideal case), for Forced flow.....	25
Fig 3-1b: Schematic of the flow over a sphere for forced flow.....	25
Fig 3-2: Coordinate System.....	26
Fig 4.1: Numerical Grid.....	36
Fig.6.1: Transition of flow over a sphere from laminar to turbulent.....	56
Fig 6-2: Meridional Velocity Profile at different meridional locations for a given Reynolds number.....	59
Fig 6-3: Effect of Reynolds number on Meridional velocity profiles at two different meridional stations.....	59
Fig 6-4a: Meridional velocity profile over the sphere surface at different radial locations.....	60
Fig 6-4b: Comparing the U-velocity of present work with that of previous work.....	61
Fig 6-5: Wall shear stress in meridional direction for a given Reynolds number.....	61
Fig 6-6: Radial velocity profile at different meridional locations.....	63
Fig 6-7: Temperature profile at different meridional locations for a given Reynolds number.....	63
Fig 6-8: Variation of heat transfer entropy generation with radial distance for different meridional stations.....	65
Fig 6-9: Variation of heat transfer entropy generation with radial distance for different	

Reynolds number at a given Eckert number.....	65
Fig 6-10: Variation of heat transfer entropy generation over the surface of the sphere at different radial locations.....	66
Fig 6-11: Variation of fluid friction entropy generation with radial distance for different meridional stations.....	68
Fig 6-12: Variation of fluid friction entropy generation with radial distance for different Reynolds number at a given meridional location.....	68
Fig 6-13: Variation of fluid friction entropy generation with radial distance for different Eckert number and meridional locations for a given Reynolds number.....	69
Fig 6-14: Comparing total entropy generation profile along radial direction for different Reynolds number.....	71
Fig 6-15: Variation of entropy generation over the sphere surface at different radial (Z) locations for a given Reynolds number.....	71
Fig 6-16: Comparing heat transfer, fluid friction and total entropy generation at a particular meridional location.....	72
Fig 6-17: Comparing entropy generation profile for different Eckert number.....	72
Fig 6-18: Variation of local average entropy generation over the sphere surface for given Reynolds and Eckert numbers.....	74
Fig 6-19: Comparing local average entropy generation profiles for different Reynolds numbers.....	74
Fig 6-20: Variation of local average fluid friction entropy generation over the sphere for different Eckert numbers and a given Reynolds number.....	76
Fig 6-21: Effect of Reynolds number on overall average entropy generation.....	77

Fig 6-22: Effect of Reynolds number on overall average entropy generation for different Eckert numbers.....	77
Fig 6-23: Effect of Eckert number on average fluid friction entropy generation for different Reynolds numbers.....	79
Fig 6-24: Effect of Eckert number on overall average entropy generation for different Reynolds numbers.....	79
Fig 6-25: Effect of Eckert number on irreversibility ratio for different Reynolds number.....	82
Fig 6-26: Effect of Reynolds number on irreversibility ratio for different Eckert number.....	82
Fig 6.27: Effect of Eckert number on Bejan number for different Reynolds number.....	83
Fig 6-28: Effect of Reynolds number on Bejan number for different Eckert numbers....	83
Fig 6.29: Meridional velocity profile at different meridional locations and for a given Reynolds number.....	85
Fig 6.30: Radial velocity profile at different meridional locations.....	85
Fig 6-31: Sphere wall temperature profile for different Reynolds numbers.....	87
Fig 6-32: Temperature profile at different meridional locations for two different Reynolds numbers.....	87
Fig 6-33: Variation of heat transfer entropy generation with radial distance at different meridional stations, UHF case.....	89
Fig 6-34: Variation of heat transfer entropy generation with radial distance for different Reynolds numbers.....	89
Fig 6-35: Variation of fluid friction entropy generation with the radial distance at	

different meridional stations.....	91
Fig 6-36: Variation of fluid friction entropy generation with the radial distance for different Reynolds numbers and at a given meridional location.....	91
Fig 6-37: Variation of total entropy generation with the radial distance for different meridional locations.....	93
Fig 6-38: Comparing total entropy generation profile for different Reynolds numbers...	93
Fig 6-39: Variation of entropy generation over the sphere surface at different radial (Z) locations for a given Reynolds number.....	94
Fig 6-40: Comparing heat transfer and total entropy generation at a particular meridional location and Eckert number.....	94
Fig 6-41: Variation of local average heat transfer entropy generation for different Reynolds numbers.....	96
Fig 6-42: Variation of local average entropy generation for different Reynolds number..	96
Fig 6-43: Comparing local average entropy generation profile for different Eckert numbers and a given Reynolds number.....	98
Fig 6-44: Effect of Reynolds number on average entropy generation profile for different Eckert numbers.....	99
Fig 6-45: Effect of Eckert number on average fluid friction entropy generation for different Reynolds number.....	100
Fig 6-46: Effect of Eckert number on average entropy generation profile for different Reynolds numbers.....	101
Fig 6-47: Effect of Eckert number on irreversibility ratio for different Reynolds number.....	103

Fig 6-48: Effect of Reynolds number on irreversibility ratio for different Eckert number.....	104
Fig 6-49: Effect of Eckert number on Bejan number for different Reynolds number....	105
Fig 6-50: Effect of Reynolds number on Bejan number for different Eckert number....	106
Fig 7-1: Variation of meridional velocity with radial distance for two different meridional stations.....	109
Fig 7-2: Variation of meridional velocity over the sphere surface.....	109
Fig 7-3: Variation of radial velocity with radial distance at different radial locations....	111
Fig7-4:Temperature profile for different Grashof number at given meridional station..	111
Fig 7-5: Variation of local heat transfer entropy generation with radial distance for two selected meridional angles.....	113
Fig 7-6: Variation of local heat transfer entropy generation with radial distance for different Reynolds numbers.....	113
Fig 7-7: Variation of local heat transfer entropy generation for different Grashof numbers.....	115
Fig 7-8: Variation of local fluid friction entropy generation with radial distance at two different meridional stations.....	115
Fig 7-9: Variation of local entropy generation with radial distance and at two meridional stations.....	116
Fig 7-10: Variation of local entropy generation for different Grashof numbers.....	116
Fig 7-11: Local entropy generation for different Grashof number over the surface of the sphere.....	118
Fig 7-12: Comparing heat transfer and fluid friction entropy generation for different	

Grashof number along radial direction.....	118
Fig 7-13: Comparing entropy generation profile for different Grashof number and Eckert number at a given $Re (= 5000)$ and at $\theta = 1050$	119
Fig 7-14: Variation of local average entropy generation over the sphere surface for a given Reynolds and Eckert number.....	121
Fig 7-15: Comparing local average entropy generation profile for different Reynolds numbers and Grashof numbers and for a given Eckert number.....	121
Fig 7-16: Variation of local average entropy generation for given Reynolds and Eckert number and different Grashof numbers.....	123
Fig 7-17: Variation of local average entropy generation over the sphere surface for a different Eckert number.....	124
Fig 7-18: Effect of Reynolds number on overall average entropy generation profile for different Grashof numbers.....	124
Fig 7-19: Effect of Reynolds number on irreversibility ratio for different Grashof numbers.....	126
Fig7-20:Effect of Reynolds number on Bejan number for different Grashof numbers...	126
Fig 7-21: Meridional velocity profile for two different meridional stations.....	128
Fig 7-22: Meridional velocity profile for different Grashof number over the sphere surface.....	128
Fig 7-23: Radial velocity profile for different Grashof number at different radial locations.....	130
Fig 7-24: Temperature profile for different Grashof number at given meridional station.....	130

Fig 7-25: Variation of local heat transfer entropy generation for different Grashof numbers.....	132
Fig 7-26: Variation of local heat transfer entropy generation for different Reynolds and Grashof numbers.....	132
Fig 7-27: Variation of heat transfer entropy generation along radial direction for different Grashof numbers.....	134
Fig 7-28: Variation of local fluid friction entropy generation at two different meridional stations.....	134
Fig 7-29: Variation of local entropy generation for different Grashof numbers.....	136
Fig 7-30: Variation of local entropy generation along radial direction for different Grashof numbers.....	136
Fig7-31:Variation of local average entropy generation for different Grashof number...	138
Fig 7-32: Comparing heat transfer and fluid friction entropy generation for different Grashof numbers.....	138
Fig 7-33: Variation of local average entropy generation over the sphere surface for a given Reynolds and Eckert number.....	139
Fig 7-34: Comparing local average entropy generation profile for different Reynolds numbers and Grashof numbers for a given Eckert number.....	139
Fig7-35:Variation of local average entropy generation for different Grashof numbers..	141
Fig 7-36: Effect of Reynolds number on overall average entropy generation for different Grashof number.....	141

Fig 7-37: Effect of Reynolds number on irreversibility ratio for different Grashof numbers.....143

Fig7-38:Effect of Reynolds number on Bejan number for different Grashof numbers...143

NOMENCLATURE

a sphere radius

Be Bejan number, $\frac{S_{HT}}{S_{avg}}$

c specific heat of fluid at constant pressure

Ec_m modified Eckert number, $Ec = \frac{U_{\infty}^2}{C_p t_w}$

g gravitational acceleration

Gr Grashof number = $\left(\frac{g \beta \Delta t a^3}{\nu^2} \right)$ for UWT and
= $\left(\frac{16g\beta qa^4}{k\nu^2} \right)$ for UHF

h local heat transfer coefficient based on area of sphere surface

IR Irreversibility ratio, $\frac{S_F}{S_{HT}}$

k thermal conductivity of fluid

m number of steps of the numerical mesh network in the X direction

n number of steps of the numerical mesh network in the Z direction

Nu average Nusselt number

Nu_{θ} Local Nusselt number $\left(= \frac{2ah}{k} \right)$

Pr Prandtl number of fluid $\left(= \frac{\mu c}{k} \right)$

q	Local heat flux at sphere surface
r	radial coordinate ($= z + a$)
r_0	$a \sin \theta$
R	dimensionless radial coordinate ($= r/a$)
R_0	dimensionless radius of circular cross section of the sphere by a plane perpendicular to the main stream, $\frac{2r_0}{a Re}$
Re	Reynolds number ($= 2U_\infty a / \nu$)
s_x	wall shear stress in meridional direction
S_x	dimensionless wall shear stress in meridional direction ($= s_x \sqrt{Re/2} / (\rho U_\infty^2)$)
\dot{s}_{gen}'''	entropy generation per unit volume
S_{gen}	dimensionless entropy generation due to both heat transfer and fluid friction
S_{avg}	dimensionless average entropy generation
S_{HT}	heat transfer entropy generation
S_F	fluid friction entropy generation
t	temperature
t_w	wall temperature
t_∞	free steam temperature
T	dimensionless temperature, $T = kt / (aq)$ for constant heat flux case and $T = \frac{t}{t_w}$ for isothermal case.
T_w	dimensionless wall temperature, $T_w = kt_w / (aq)$ for constant heat flux case, $T_w = 1$ for isothermal case

- u meridional (x direction) component of velocity
- u^* potential velocity component in x direction $(=U_{\infty} \text{Sin}\theta[1 + a^3 / (2r^3)])$
- U dimensionless meridional component of velocity $(=u/U_{\infty})$
- U^* dimensionless potential velocity component in the x direction $(=u^*/U_{\infty})$
- U_{∞} free stream velocity
- w radial (z direction) velocity component
- w^* radial velocity component for the potential flow $(=-U_{\infty} \text{Cos}\theta[1 + a^3 / r^3])$
- W dimensionless radial velocity component $(=w/U_{\infty})$
- W^* dimensionless radial velocity component for potential flow $(=w^*/U_{\infty})$
- x distance along circle concentric with the circular generator of the sphere surface measured from the stagnation line $(=r\theta)$
- x_0 distance along circular generator of the sphere surface measured from the stagnation line $(=a\theta)$
- X dimensionless meridional distance along any circle concentric with sphere measured from the stagnation line $(=2x/Re a)$
- X_0 dimensionless meridional distance along the surface of the sphere measured from the stagnation point $(=2x_0/Re a)$
- z distance from the surface measured normal to the wall in the radial direction $(=r-a)$
- Z dimensionless distance perpendicular to the wall in the radial direction $(=z/a)$

Greek symbols

- δ Boundary layer thickness

θ Center angle measured from the frontal stagnation line

μ Dynamic fluid viscosity

α Thermal diffusivity

ϕ Third spherical coordinate

Subscripts

s at separation point

o on sphere surface

THESIS ABSTRACT

Name : Mohammed Gayazullah

Thesis Title : ENTROPY GENERATION AROUND A SOLID SPHERE IN A GAS
STREAM

Major Field : Mechanical Engineering

Date of Degree: December, 2004

The problem of entropy generation for the convection heat transfer over a solid sphere is studied numerically using a finite difference technique. The governing energy and momentum equations are numerically solved. The effect of controlling parameters like Reynolds number (Re), Grashof number (Gr) and Eckert number (Ec_m) on the velocity components as well as the temperature within the boundary layer is investigated for both Forced and Mixed Convection. The entropy generation is calculated for both Forced and Mixed Convection and for the two boundary conditions, namely uniform heat flux and uniform wall temperature. In both the cases, the effects of various Controlling parameters like Re , Gr , and Eckert number (Ec_m) on entropy generation is investigated. And the condition in which the entropy generation becomes minimum is established.

ملخص البحث

الإسم: محمد غياث الله

عنوان الرسالة: تولد الانتروبي حول كرة من الصلب في وسط غازي

متحرك

المجال الرئيسي: الهندسة الميكانيكية

تاريخ الدرجة: ديسمبر 2004

تم في هذه الدراسة تحليلاً عددياً لتولد الإنتروبي حول كرة من الصلب في وسط يتم فيه انتقال الحرارة بالحمل وذلك بطريقة عددية باستخدام طريقة الفروق المحدودة. وقد تم حل معادلات الكتلة و كمية الحركة و بقاء الطاقة عددياً. كما تمت دراسة تأثير العناصر المؤثرة مثل رقم رينولدز و رقم جراشوف و رقم إيكارت علي منحنيات السرعة و درجة الحرارة في الطبقة المتاخمة في حالتي الحمل القسري و الحمل المركب. و قد تم حساب تولد الإنتروبي لحالتي الحمل القسري و الحمل المركب مع تطبيق حالتي ثبات درجة الحرارة أو ثبات تكثيف الحرارة على سطح الكرة. وفي كلتا الحالتين تمت دراسة تولد الإنتروبي كنتيجة لتغيير العناصر المؤثرة و قد تم تحديد المدي الذي تكون فيه الإنتروبي عند قيمتها الدنيا.

CHAPTER I

INTRODUCTION

1.1 General

At the root of the growing interest in the thermodynamic irreversibility of heat transfer lies the emphasis placed today on energy conservation and the efficient use of energy. In any power plant, for example, the thermodynamic nonideality (irreversibility) of any of its engineering components causes a decrease in the net power output of the cycle. Hence from an engineering point of view, it is essential to first identify the irreversibility associated with various components and, second, to design for less irreversibility in order to avoid the imminent loss of available power.

Engineering components and devices for heat transfer are inherently irreversible, that is they are associated with entropy generation. The task of conserving useful energy rests heavily on our ability to produce thermodynamically efficient heat transfer processes and equipment for such processes. Entropy generation may be due to variety of sources, primarily heat transfer across temperature gradients in addition to viscous effects. The foundation of knowledge of entropy production goes back to Clausius' and Kelvin's studies on the irreversible aspects related to the second law of thermodynamics. Since then the theories based on these foundations have rapidly developed.

1.2 Scope of the Present Work

Flow and convection heat transfer study over a sphere has gained enormous interest of researchers for many years. The present work is aimed at studying in detail the entropy generation around a solid sphere, which is kept in an air stream. The practical application of this analysis is found in solid fuel burning and evaporation, in some manufacturing systems such as in packed beds of spherical bodies, and in heat transfer in electronic components which are nearly spherical. In order to augment the heat transfer, entropy generation should be minimized. Entropy generation is positive and finite as soon as the temperature or velocity gradients are present in the medium. Few of the sources of entropy generation are fluid friction, solid friction, flow impact, heat transfer across finite temperature difference, plastic deformation, etc.

In the present work, a finite difference method has been developed to analyze the flow field, convective heat transfer and entropy generation around a solid sphere. The method used here needs less computer time and storage in comparison with the numerical methods discussed in the literature for the flow and heat transfer analysis, and it also handles wide range of Reynolds number, Grashof number and Eckert number. To the best of author's knowledge, this is the first attempt to study entropy generation over a sphere as will be demonstrated in the next chapters.

This chapter included an introduction and the scope of the present study. Chapter II presents the Literature survey. Chapter III will be devoted to the problem formulation, non-dimensional form of governing equations as well as the boundary layer

simplification. In Chapter IV, the grid system and finite-difference forms of the governing equations are presented. The overall solution methodology and the method employed for calculating the engineering parameters are discussed in Chapter V. The results for forced convection case are presented and discussed in Chapter VI and for mixed convection case in Chapter VII. Finally conclusions and recommendations are presented in Chapter VIII followed by references and the appendix. The appendix presents the detailed derivation of the entropy generation equation and non-dimensionalizing of the entropy generation for both Uniform wall temperature and Uniform heat flux cases.

CHAPTER II

LITERATURE SURVEY

2.1 Introduction

The present literature survey will be classified into two different parts. First, the fluid flow and heat transfer over sphere with and without rotation, both for forced and mixed convection. Second, the entropy generation analysis for external and internal flows over bodies of different shapes with different boundary conditions.

2.2 Fluid flow and Convection Heat Transfer over Spheres

Jia and Gogos [1] studied the laminar natural convection heat transfer from isothermal spheres numerically for wide range of Grashof numbers ($10^1 < Gr < 10^8$) and for Prandlt numbers 0.72 and 7.0. They noticed that a plume with a mushroom-shaped front forms above the sphere whose length and thickness decrease with increasing Gr. At higher Gr ($Gr \geq 10^7$ and $Pr = 0.72$), flow separation and an associated recirculation vortex exist in the wake of the sphere. The vortex size increases with Gr and this vortex is responsible for the sharp increase in the local Nusselt number near the top of the sphere.

Mixed convection boundary layer flow about a sphere with constant surface temperature was studied by **Nazar et al. [2]**. They used mixed convection parameter (Gr/Re^2) ranging between -4.0 to 20. They found that the aiding flows delay separation and can, if the aiding flow is strong enough, suppress it completely. The opposing flow on the other hand, brings the separation point nearer to the lower stagnation point of the sphere. The results also showed that the values of the local skin friction coefficient are lower and those of the local heat transfer coefficient are higher for $Pr=6.8$ than $Pr=0.7$ when buoyancy parameter is fixed. They also showed that in the case of aiding flow, an increase in the buoyancy forces results in a decrease of the temperature field and a decrease in the thermal boundary-layer thickness, and an opposite behaviour for opposing flow.

Pruppacher[3] investigated numerically the steady incompressible flow around a sphere and solved Navier-Stokes equations for $20 \leq Re \leq 40$ and found that the eddy length and separation angle increase with increasing Reynolds number. Axisymmetric laminar boundary-layer flow around a rotating sphere was investigated numerically by **El-Bedeawi[4]** and **El-Shaarawi et al. [5]** for a value of Reynolds number of 10000 over a wide range of the spinning parameter (upto $Ta/Re^2=10000$). They reported that for the range of spin parameter considered, the separation point always lies behind the equatorial plane and shifts forward as the value of the parameter Ta/Re^2 increases. **El-Shaarawi et al. [6]** studied the mixed convection about a rotating sphere maintained at uniform surface heat flux for wide ranges of Re ($1000 \leq Re \leq 10,000$), Gr ($-10^9 \leq Gr \leq 10^9$), and Ta/Re^2 ($0 \leq Ta/Re^2 \leq 10,000$). They reported that the aiding free convection causes an

increase in velocities (meridional and radial) as compared with the isothermal case ($Gr = 0$), while an opposing free convection causes a decrease in these velocity components. They also found that an aiding/opposing flow causes a reduction/increase in the wall temperature.

Lepalec and Daguene[7] applied a power series of several variables to study the laminar mixed convection about an isothermal rotating sphere in a stream of arbitrary direction with respect to the axis of rotation, so that the velocity profile is essentially three dimensional. Boundary layer equations were numerically solved and the results for different values of rotation parameter and buoyancy parameter were obtained. The results showed that the opposing flow produces a larger velocity gradient at the wall with an accompanying increase in the friction factor and the local heat transfer rate that has a higher value at higher rotation speeds. They also developed solutions for heat and mass transfer from a rotating sphere placed coaxially in an upward flowing stream. The theoretical results developed by boundary-layer analysis were verified by experiments utilizing an electrochemical reaction at the surface of an electrically charged sphere [8].

Mixed convection about a sphere was also investigated experimentally by **Yuge**[9] for small Reynolds and Grashof numbers. **Chen and Mucoglu**[10] studied mixed, forced and free convection heat transfer from isothermal spheres in air. It was reported that both the local friction factor and local Nusselt number increase with increase in buoyancy force for aiding flow and decrease with increasing buoyancy force for opposing flow. They also investigated the mixed convection case for uniform heat

flux boundary conditions for both aiding and opposing flows, and found that both the local wall shear and the local Nusselt number increase with increasing buoyancy force for assisting flow, where as for opposing flow, the local wall shear and Nusselt number decrease with increasing buoyancy force [11].

Tang and Johnson[12] performed an experimental study and flow visualization for mixed convection about a sphere and proved that the mixed and natural convection depend on sphere diameter. **Antar et al. [13]** studied mixed convection for the flow over a liquid sphere and found that the results approach those of a solid sphere as the liquid/gas viscosity ratio increases.

Oscillating viscous flow over a sphere was studied by **Alassar and Badr [14]** and results were presented for periodic variation of the drag coefficient, surface vorticity and pressure distributions for Reynolds numbers ranging from 5 to 200. They showed that at early phase angles, higher Re will produce longer recirculation regions and the trend reversal takes place at later stages. The time variation of the velocity field during one complete oscillation has been presented in the form of stream line and equivorticity patterns.

2.3 Study of Entropy Generation

2.3.1 Entropy Generation for Internal flows

Bejan [15] studied the entropy generation in convective heat transfer in a pipe flow, boundary-layer flow over flat plate, single cylinder in cross flow and flow in the

entrance region of a flat rectangular duct. In pipe flow with negligible axial conduction effect ($Pe \gg 4$), the value of $EcPr/\tau$ (where, $\tau = \Delta T/T$) increases gradually to the point where viscous effects dominate N_s^{\min} (entropy generation number). Peclet number Pe , governs the importance of irreversibility associated with conduction in the axial direction. For $Pe < 4$ the axial conduction contribution dominates the radial conduction effect. In all cases the pipe wall region acts as strong concentrator of irreversibility. As the aggregate duty parameter $B_o \left(B_o = \frac{q/L}{U_\infty (k\mu T_\infty Pr^{1/3})^{1/2}} \right)$ increases, the optimum tube radius decreases (Re increases) and minimum entropy generation N_s^{\min} also decreases.

Shohel et al. [16] studied the second law characteristics of heat transfer and fluid flow due to forced convection of steady laminar flow of incompressible fluid inside circular and parallel plate channels. For different cases, the entropy generation number (N_s) and Bejan number (Be) were derived. The results for both Newtonian and non-Newtonian fluids were obtained. The entropy generation number (N_s) was plotted against different parameters such as distance between plates, radius of cylinder and Brinkman number ($EcPr$).

Haddad et al. [17] studied the entropy generation due to laminar forced convection in the entrance region of a concentric annulus. The effect of different flow parameters on thermal, viscous, and total entropy generation was studied for different thermal boundary conditions. The viscous term was included in the entropy generation equation although it was neglected in the temperature profile, in order to study the

contribution of both viscous and thermal entropy on total entropy generation. Entropy generation was found to be inversely proportional to both Reynolds number and the dimensionless entrance temperature. Total entropy generation was found to be increasing with increasing Eckert number and/or radius ratio, and decreasing for increasing Reynolds number. Finally it was found that thermal entropy generation was dominant over viscous entropy generation.

Entropy generation in Poiseuille-Benard flow using a control volume method was investigated by **Abbassi et al. [18]**. Variation of entropy generation and Bejan number as functions of Rayleigh number and irreversibility distribution ratio (ϕ) were investigated. It was found that the limiting value of ϕ is a decreasing function of Ra. The maximum entropy generation is localized at areas where the heat exchange between the walls and the flow is maximum. The contour plots showed that the regions of maximum entropy generation coincides exactly with regions of maximum Nusselt numbers. Hence the augmentation of energy exchanged between the walls and the flow contribute to the augmentation of entropy generation via the increase of temperature gradient near the walls. Hence it was concluded that the entropy generation is largely higher near the walls than that in the central flow.

Tasnim et al. [19] studied mixed convection and entropy generation in a vertical annular space with isothermal boundary conditions. For a particular group parameters, average entropy decreases with the increase of radius ratio (Π), shows its minimum and again increase with further increase of Π . Fluid friction irreversibility increased and heat

transfer irreversibility decreased with increase in Π . Hence a minimum entropy generation for a particular Π_{opt} was obtained. The ratio of Brinkman number to dimensionless temperature (Br/Ω) indicate the relative importance of viscous effect on irreversibility. At lower Br/Ω , minimum entropy generation occurs at higher Π . Average entropy generation number increases with the increase of Br/Ω for a particular value of Π .

Sahin [20] analytically investigated the second law analysis of laminar viscous flow through a duct subjected to a constant wall temperature. He used two fluids, water and glycerol in order to show the temperature dependence on the viscosity. He analysed the entropy generation for different duct lengths and fluid inlet temperatures considering the variation of viscosity with temperature. In this study, three dimensionless terms were derived namely, Π_1 (modified Stanton number), Π_2 (dimensionless group, $Ec/St Re$), and ψ (dimensionless entropy generation). A reasonably accurate empirical correlation of liquid viscosity with the temperature was taken from the literature so as to check the change of viscosity with temperature. The results showed that the effect of viscosity change due to temperature on the entropy generation for water was insignificant where as this change was significant for glycerol. For constant viscosity flow in the duct, entropy generation increased along the length of the duct. It was stated that for a certain length of the duct there were minimum exergy losses. It was also found that increasing the dimensionless temperature difference between the inlet fluid and surface temperature, increased entropy generation, hence there is certain fluid inlet temperature exists for which the exergy losses are minimum.

Sahin [21] has also studied the entropy generation in turbulent flow through a smooth duct subjected to constant wall temperature. Similar to the case for laminar flow, this time also the temperature dependence of the viscosity was taken into consideration in the analysis. A comparison of results between temperature-dependent and constant viscosity cases showed that the constant viscosity assumption may yield a considerable amount of deviation in entropy generation from those of the temperature dependent viscosity cases, especially when high viscous fluids are considered. He used the same nondimensional terms as in the laminar case, and found that the entropy generation per unit heat transfer rate decreases initially and then increases along the duct length. It was also found that the entropy increased with the increase in the dimensionless temperature difference between the inlet fluid and surface temperature.

San et al [22] investigated the entropy generation for combined forced convection heat and mass transfer in a two dimensional channel with constant heat flux boundary condition. For laminar case, the entropy generation was obtained as a function of velocity, temperature, concentration gradients and the physical properties of the fluid. The optimum plate spacing was determined, considering that either the mass flow rate or the channel length is fixed. For the turbulent regime, a control volume approach that uses heat and mass transfer correlations was developed to obtain the entropy generation and optimum plate spacing. At plate spacing less than the optimum value, the entropy generation increased sharply. The end for the generation due to mass diffusion has a

similar form to that due to heat transfer and both are linearly dependent on the channels spacing.

Tasnim et al [23] studied the entropy generation in a vertical concentric channel with temperature dependent viscosity for laminar flow with isothermal boundary conditions. The results showed that for a particular group of parameters, magnitude of $N_{s,av}$ (average entropy generation number) decreases with an increase of the radius ratio (Π), they showed that it reaches a minimum value for a particular value for Π , and increases with further increase in the radius ratio. Π dependent nature of fluid friction and heat transfer irreversibility was found opposite in character. Fluid-friction irreversibility increased and heat-transfer irreversibility decreased with the increase in radius ratio. The magnitude of Π , where entropy generation is minimum, was termed as Π_{opt} . At lower Br/Ω (Brinkman number / dimensionless temperature difference), minimum entropy generation occurred at higher Π . It was also found that at smaller radius ratio ($\Pi < 2.0$), average entropy generation rate was the same in magnitude for all group parameters.

Numerical predictions of entropy generation for mixed convection flows in a vertical channel with transverse fins was studied by **Cheng et al [24]**. A control volume-based finite-difference method was used to solve the governing equations which were expressed in stream function-vorticity form. The results showed that the larger gradients of velocity and temperature at the fin tips and wall surfaces result in relatively high entropy generation in these areas. In general, highest entropy generation rates appear in

the immediate neighborhood of the fin tips. Effect of Reynolds number on entropy generation rates show that higher Reynolds number result in higher entropy generation.

Second-law analysis of rectangular channels with square pin fins was studied experimentally by **Sara et al [25]**. Various fin ratios and inter fin distance ratios were used, and optimum pin fin arrays that minimize entropy generation were determined. The results showed that the heat transfer increased by the use of fins, while causing the increase in friction factor due to fins. It was also found that smaller the interfin spacing ratio, the higher is the entropy generation number. This entropy generation number also increased with increasing Reynolds number. Smaller entropy generation numbers were obtained at lower Reynolds number, higher clearance ratio and higher interfin spacing ratio.

Shohel and Fraser [26] examined analytically the effects of radiation heat transfer on mixed convection through a vertical channel in the presence of transverse magnetic field. The location where the temperature gradient is zero is the idle point for the temperature entropy generation, where it will be also zero, and this was found to be at the center of the channel. Entropy generation profile was found to be symmetric about the centerline of the channel due to the symmetric distributions of velocity and temperature. For all the group parameters, each wall acts as a strong concentrator of entropy generation because of the high near wall gradients of velocity and temperature. Minimum entropy generation number was also found for different group parameters, Br/Ω (i.e. ratio of Brikman number to dimensionless temperature difference).

Shohel and Fraser [27] also investigated the first and second law characteristics of forced convection fluid flow and heat transfer inside a channel having two parallel plates with finite gap between them. No entropy generates in the center line of the duct for all the group parameters. N_s (entropy generation number) increases along vertical distance(Y). Bejan number was also plotted against Y , and it was found to be maximum at the center line and then drops slowly toward walls. Group parameter, Br/Ω (i.e. ratio of Brikman number to dimensionless temperature difference) has a significant effect on the entropy generation.

Yilbas et al. [28] used CFD techniques to study natural convection and entropy generation in a square cavity with differential top and bottom wall temperatures. They showed that the entropy generation amplified when circulation along the x-axis increases and the entropy generation becomes minimum for a particular Rayleigh number. It was shown that the entropy generation is considerably high near the heated walls due to fluid friction and heat transfer, as expected.

Baytas [29] studied the entropy generation for natural convection in an inclined porous cavity using Darcy's law and Bousinesq-incompressible approximation. Two opposite walls were kept at different temperatures and the other two were thermally insulated. The effect of inclination angle on the flow and heat transfer characteristics and the entropy generation was studied by varying angle from 0° to 360° and dimensionless Rayleigh number from 10^2 to 10^4 . The isotherms, the patterns of stream lines and their

corresponding entropy generation maps, the variation of entropy generation due to heat transfer and fluid friction irreversibility versus inclination angle for different Rayleigh numbers were presented. The results showed that when Ra decreases, heat transfer irreversibility begins to dominate the fluid friction irreversibility .

Shuja et al. [30] investigated the mixed convection in a square cavity due to heat generating rectangular body for different exit port locations, and studied the irreversibility generation. Fifteen different locations of exit port were introduced while air is used as an environment in the cavity. It was found that non-uniform cooling of the solid body occurs for some exit port locations and in those cases, heat transfer reduces while irreversibility increases in the cavity.

Magherbi et al. [31] studied the variation of total entropy generation at the onset of natural convection for the case of a square cavity with top and bottom walls with adiabatic boundary condition. The evolution of entropy generation, and the Bejan number in transient state were studied for different Rayleigh number and irreversibility distribution ratio. The results show that the dimensionless total entropy generation has a maximum value at the onset of the transient state, then decreases to reach a constant value in the steady state. This of constant value is for the small Ra values. For high Ra, an oscillation of the entropy generation was observed before reaching the steady state. These fluctuations in total entropy at high Ra number indicate that the flow exhibits oscillatory behavior which depends on the boundary conditions. Results also showed that

the Bejan number takes a minimum value in the beginning of the transient state which decreases with increasing Ra number and irreversibility distribution ratio.

Mahmud and Islam [32] investigated the laminar free convection and entropy generation inside an inclined wavy enclosure bounded by two isothermal wavy walls and two adiabatic straight walls at different Rayleigh numbers and orientations, using a finite volume technique. As an alternative irreversibility distribution parameter Bejan number was used, which is the ratio of the heat transfer irreversibility to total entropy generation. At very low Ra, fluid is almost motionless in the cavity. Near wall concentration of Bejan number indicates the region of high irreversibility.

Budair [33] investigated the case of impulsively started Couette flow. In his paper, he solved the one-dimensional volumetric entropy generation equation. It was shown that the entropy generation in the space between the plates is more considerable at initial times of motion than at later times, which showed that the frictional losses are much more than those incurred later in the motion in the steady state. For isothermal process, the dissipation energy will be only due to frictional losses as the case under consideration. The localized entropy generation is always near the vicinity of the plate. And this level of generation, how ever, decreases with time.

2.3.2 Entropy Generation for External flows

Bejan[15] studied the entropy generation in fundamental convective heat transfer problems such as pipe flow, boundary layer flow over flat plate, single cylinder in cross flow and flow in the entrance region of a flat rectangular duct. It was found that for the

laminar flow over a flat plate the higher the duty parameter $\left(B_o = \frac{q/L}{U_\infty (k\mu T_\infty \text{Pr}^{1/3})^{1/2}} \right)$,

the higher the optimum Re (plate length), and the lower is the minimum entropy generation number. In other words, if the total heat transfer rate q' is constant and the flow velocity increases, the optimum plate length decreases and the minimum attainable entropy generation rate increases. Similar results were obtained for the cylinder in cross flow, as the duty parameter increases, the optimum Reynolds increases and the minimum entropy generation number decreases.

Abu-Hijleh [34] studied numerically the entropy generation for the laminar mixed convection over an isothermal heated cylinder for different values of Reynolds number (1 to 200), buoyancy parameter ($\kappa = 0$ to 10) and cylinder diameter (10^{-5} to 7.5). The general trend shows that the entropy generation number (N_s) decreases with D and increases with both κ (Gr_D/Re_D^2) and Re. For all values of Re_D , the N_s was lowest for $\kappa = 0$ which results from a zero temperature difference between the cylinder and incoming flow so the entropy is generated only by viscous effects. Finally, the results showed that there is significant increase in entropy generation due to mixed convection over pure convection, especially at small cylinder diameters. The difference between the entropy generated due to mixed and pure convection decreases with increasing cylinder diameter.

Abu-Hijleh et al. [35] investigated the entropy generation due to laminar natural convection over isothermal cylinder. Local and total entropy generations were calculated for Rayleigh numbers ranging from 1 to 10^7 and three cylinder radii ranging from 10^{-3}

to 10^{-1} . An increase in Ra and thus higher temperature difference between the cylinder and surroundings, results in increase in value of total entropy generation, and use of larger cylinder radius results in lower temperature difference and in turn lower entropy generation for same value of Ra. The analysis of local entropy profiles revealed that the location of maximum entropy generation was dependent on size of the cylinder.

Abu-Hijleh et al. [36] studied entropy generation due to laminar natural convection over a heated rotating cylinder with isothermal boundary condition. Higher value of buoyancy parameter $\kappa (Gr_D/Re_D^2)$ results in the increase in heat transfer which is desired in heat exchangers, but usually at the expense of higher entropy generation, i.e. lower thermodynamic efficiency. In this study, they found that the use of very high values of κ results in minimal increase in entropy generation, thus heat transfer rates increase without lowering efficiency. Overall results showed that the total entropy generation decreased with the increase in cylinder radius. The contribution of conduction and viscous parts in total entropy generation were also studied in the paper. Entropy generation due to conduction effect was dominant at medium cylinder radius with an exception for the combination of low Reynolds number and buoyancy parameter, where the viscous contribution becomes dominant.

Abu-Hijleh [37] investigated numerically the entropy generation due to laminar forced convection heat transfer from an isothermal horizontal cylinder covered with an orthotropic layer. The different parameters used for the study are non-dimensional porous layer thickness (R_p), non-dimensional pressure loss coefficient (K_r – radial and K_θ –

tangential) and Reynolds number ($Re_D = 5$ to 150). K_r has a minimal effect on the total entropy generation. Only at high values of R_p and low values of K_θ , does a changing K_r result in noticeable change in N_s . Which indicates that K_θ is the dominating factor of the two pressure loss coefficients. Finally, the addition of orthotropic porous layer reduces heat transfer as well as the entropy generation. The general trend in entropy generation reduction was similar to that of the total entropy generation from the cylinder. There was an optimum porous layer beyond which the total entropy generation did not decrease.

Abu-Hijleh [38] performed study on optimized use of baffles for reduced natural convection heat transfer from a horizontal cylinder. The aim was to optimize the number, size and location of the baffles for maximum natural convection heat transfer, that is Nusselt number for a wide range of Rayleigh number. Optimal tangential location for a single baffle and two baffles were found while comparing the data with uniform baffles for different baffle heights and Rayleigh number. The results showed that the use of baffles result in more thermodynamically efficient system. Entropy generation was mainly found due to thermal effects rather than the viscous effects, While the use of baffles on large cylinder diameters reduced the total entropy generation as a whole.

Haddad et al. [39] studied the entropy generation due to laminar forced convection flow past a parabolic cylinder. It was reported that the thermal entropy generation increased as the temperature increased, while both the viscous and thermal entropy generation decreased as Reynolds number increased. Viscous contribution to entropy generation was dominant for all values of Mach number. And an increase in Mach number results in an increase in entropy generation as a whole. As thermal effects

played a secondary role for parabolic profile, the reduction in entropy generation should focus on controlling the hydrodynamics of the flow and not the temperature field.

Iswar [40] studied the second law analysis of convective droplet burning, in which he studied the entropy generation equation applicable to chemically reacting flows and considered multiphase combustion like burning of particles in fluid stream. It was determined that for droplet burning at low Reynolds numbers the entropy generation is minimized by comparing two terms: one involving the mass loss from the droplet and the other involves the drag force.

Carrington [41] used control volume method to establish the rate of entropy generation due to heat and mass transfer in a fluid stream, accompanied by fluid friction for internal and external flows. They showed that the application of Gibbs equation in its extensive representation leads to error because it fails to recognize the need for local thermodynamic equilibrium. The main work done in this paper was to evaluate the papers by others and then resolve the errors in their studies of entropy generation.

Shuja et al. [42] used CFD to investigate the flow and entropy analysis over a solid rectangular body with constant heat flux for three different fluids. It was found that the fluid properties has a considerable effect on entropy generation, and that the entropy generation due to heat transfer well exceeds the entropy generation due to fluid friction. It was also shown through entropy contours that the shear flow close to the top surface and stagnation flow in the solid body contribute more to the flow irreversibility as compared

to the total flow field, i.e. the circulation behind the solid body appears to be contributing less in entropy generation. The entropy generation in the field due to convective heat transfer becomes negligible when compared to the entropy generation in the solid body due to conduction effect.

Shuja et al. [43] studied vortex shedding over a rectangular cylinder with ground effect and extended the study to include the entropy generation in the solution domain. The results in the 3-D plots showed that the entropy generation due to heat transfer increases with time. Entropy generation due to fluid friction remains almost uniform with time except at long heating periods and with reducing gap heights. Moreover, the total entropy generation due to fluid friction and heat transfer increases considerably for small gap height, which is the height between the cylinder and ground.

Lin and Lee [44] performed second law analysis on a flat plate-fin array under crossflow, from which the entropy generation was evaluated. The results showed that the increase in cross flow fluid velocity would enhance the heat transfer or equivalently, reduce the heat transfer irreversibility. Owing to the simultaneous increase in drag force exerting on the fin bodies, the hydrodynamic irreversibility increase as well. An optimal Reynolds number was thereby found for wide range operating conditions. Optimal design/operational conditions under fixed base areas constraint or fin volume constraint were searched for on the basis of entropy generation minimization. The fin volume and total base area were found to be insignificant geometrical factors.

Shuja et al. [45] analyzed the heat transfer and irreversibility for the flow through a protruding bluff body for a transient case. Heat transfer characteristics were examined using normalized Stanton number. Normalized St attains the lowest values in the central region of the rear surface in the span-wise direction because of the less convection cooling of the surface. Alternatively as the distance from the center of the body increased in the span wise direction Normalised Stanton number reach a maximum value. It was found that the heat transfer in the region of the top and bottom edges of the bluff body is enhanced due to the convection effect. The entropy contours were found densely populated around the body especially for the fluid friction contribution, because the viscous dissipation is considerably high around the body. Irreversibility increased gradually as the heating progresses but becomes steady after some time due to steady heating cycle. The heat transfer to irreversibility ratio (Q/I) decreases rapidly as the heating progresses.

To the best of the author's knowledge, the study of entropy generation over a solid sphere is not available in the literature. Hence in the present study, the entropy generation for the laminar flow about a sphere is investigated for uniform wall temperature and uniform heat flux boundary conditions.

CHAPTER III

GOVERNING EQUATIONS

3.1 Introduction

In this chapter, the governing equations that describe the fluid flow and heat transfer as well as the entropy generation for the flow over a sphere are presented. This includes the detailed derivation of these equations starting from the Navier Stokes equations as well as the energy equation for spherical polar coordinates. Transformation of the governing equations to the orthogonal curvilinear coordinates, non-dimensionalization and order of magnitude analysis is carried on to simplify the equations [46], and entropy generation equation are presented in Appendix-A.

The major assumptions employed in the derivation of the governing equations and entropy generation equations are:

1. Laminar, axisymmetric, steady flow and steady heat transfer
2. Viscous dissipation, thermal radiation and buoyancy effects are neglected in energy equation
3. Fluid is Newtonian with constant properties
4. Reynolds number is large enough to allow the use of boundary layer theory but small enough so as not to induce turbulence
5. Body forces are negligible

6. No chemical reactions
7. Surface active impurities and turbulence are absent
8. The flow outside the boundary layer is potential flow around a sphere
9. Eckert number is small enough to keep the flow incompressible

A schematic of the flow patterns is shown in the figure: 3.1.

3.2 Governing Equations:

In this work, the orthogonal curvilinear coordinate systems is used as shown in the Fig: 3.2, where the x-axis is measured along the surface of the sphere starting from the stagnation point and extends in the meridional direction till the rear stagnation point. The z-axis passes through the center of the sphere, where its zero starts from the surface of the sphere. The detailed transformation of the governing equations to its orthogonal curvilinear coordinates is presented in Antar [46].

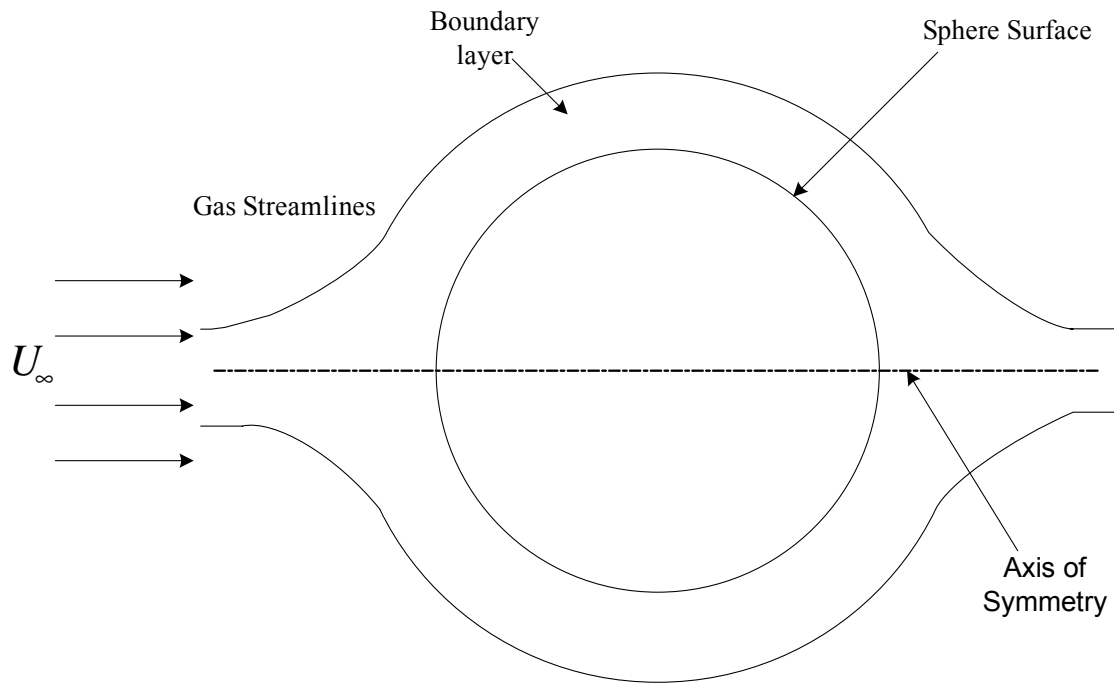


Fig 3-1a: Schematic diagram showing the boundary layer over a sphere (ideal case), for forced flow

Fig 3-1b: Schematic of the flow over a sphere for forced flow

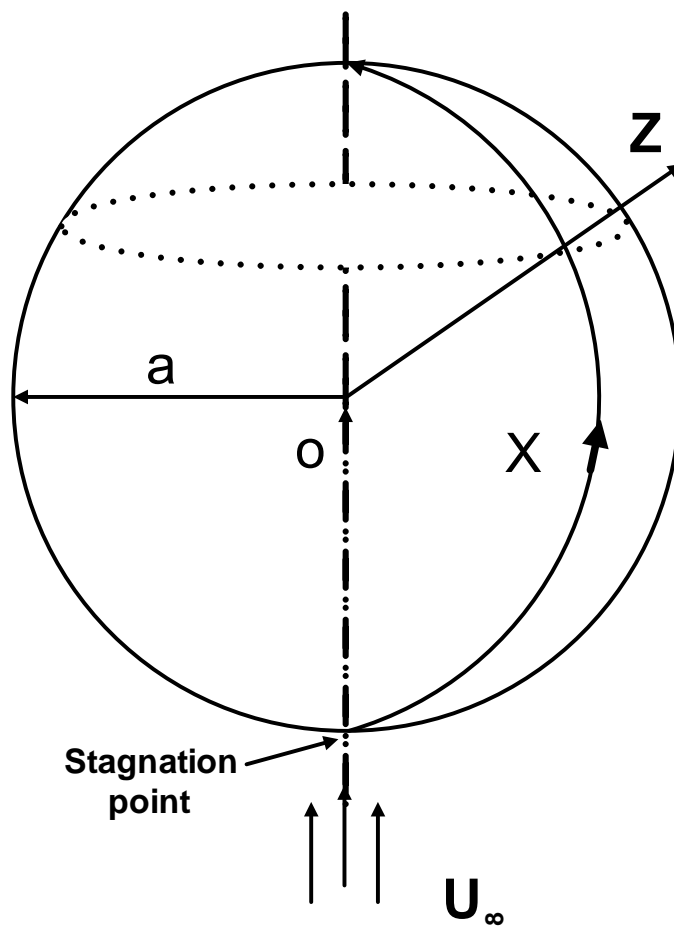


Fig 3-2: Coordinate System

3.2.1 Governing Boundary Layer Equations:

The dimensionless parameters for the governing equations are as follows:

$$\begin{aligned}
 z = aZ & \qquad \frac{\partial t}{\partial z} = \frac{\partial t}{a\partial Z} \\
 X = \frac{2x}{a \operatorname{Re}} & \qquad \frac{\partial t}{\partial x} = \frac{2}{a \operatorname{Re}} \frac{\partial t}{\partial X} \\
 U = \frac{u}{U_\infty} & \qquad \frac{\partial u}{\partial x} = \frac{2U_\infty}{a \operatorname{Re}} \frac{\partial U}{\partial X} \qquad \frac{\partial w}{\partial x} = \frac{2U_\infty}{a \operatorname{Re}} \frac{\partial W}{\partial X} \\
 w = WU_\infty & \qquad \frac{\partial w}{\partial z} = \frac{U_\infty \partial W}{a\partial Z} \\
 \frac{w}{a+z} = \frac{U_\infty W}{a(1+Z)} & \qquad \frac{u}{a+z} = \frac{U_\infty U}{a(1+Z)} \\
 P = \frac{p}{\rho U_\infty^2} & \qquad \operatorname{Pr} = \frac{\nu}{\alpha} \\
 \operatorname{Re} = \frac{2U_\infty a}{\nu} & \\
 T = \frac{t}{t_\infty} &
 \end{aligned} \tag{3.1}$$

Based on the assumptions stated in section 3.1, the governing equations in the orthogonal curvilinear coordinate system in dimensionless form as given by [6, 46, and 48] are:

Continuity equation:

$$U \frac{\partial U}{\partial X} + \frac{\text{Re} W}{2} \frac{\partial W}{\partial Z} + \frac{U}{R_o} \frac{dR_o}{dX_o} + \text{Re} \frac{W}{1+Z} = 0 \quad (3.2)$$

Momentum conservation in meridional direction

$$U \frac{\partial U}{\partial X} + \frac{\text{Re} W}{2} \frac{\partial U}{\partial Z} = U^* \frac{\partial U^*}{\partial X} + \frac{\partial^2 U}{\partial Z^2} \pm \frac{\text{Gr}}{8 \text{Re}} T \sin \theta \quad (3.3)$$

Momentum conservation in the azimuthal direction:

$$U \frac{\partial V}{\partial X} + \frac{\text{Re} W}{2} \frac{\partial V}{\partial Z} + \frac{UV}{R_o} \frac{dR_o}{dX_o} = \frac{\partial^2 V}{\partial Z^2} \quad (3.4)$$

Energy equation for forced flow:

$$U \frac{\partial T}{\partial X} + \frac{\text{Re} W}{2} \frac{\partial T}{\partial Z} = \frac{1}{\text{Pr}} \frac{\partial^2 T}{\partial Z^2} \quad (3.5)$$

3.2.2 Boundary conditions:

Examining the boundary layer equations presented in the last section leads to the determination of the required number of boundary conditions needed to make the problem investigated well-posed and amenable to numerical solution. The second derivative with respect to X is absent from the momentum equation and only the first derivative of U is present. Therefore, the boundary condition at one end is required in the meridional direction, namely at the front stagnation point. The derivatives with respect to

Z are second order, that is, two boundary conditions should be used along the radial direction. These two boundary conditions can be determined at two locations, namely one at the surface of the sphere where the value of U is zero due to no slip condition on the sphere surface and the other one is at the edge of the boundary layer where the value of U can be taken equal to the value of potential flow around a sphere. Only the first derivative of W with respect to Z is present. Hence only one boundary condition is required and can be determined at the surface of the sphere where the value of W is zero (no fluid suction or blowing).

Similarly by investigating the energy equation, it is clear that the first derivative of temperature with respect to X is present and hence only one boundary condition in the meridional direction is required and two boundary conditions in Z-direction.

Meridional as well as radial potential velocity components which are applied at the edge of the boundary layer can be obtained from the theoretical potential flow around a stationary sphere [49]. Considering the sphere radius as 'a', stream function as ψ and the potential function as ϕ we have:

$$\psi = \frac{1}{2} u_{\infty} r^2 \sin^2 \theta \left(1 - \frac{a^3}{r^3} \right) \quad (3.6)$$

and

$$\phi = u_{\infty} r \cos \theta \left(1 + \frac{a^3}{2r^3} \right) \quad (3.7)$$

Meridional and radial velocity components for the potential flow are related to the previous two equations by the following relations:

$$u^* = -\frac{1}{r} \frac{\partial \psi}{\partial \theta} = u_\infty \left(1 + \frac{a^3}{2(a+z)^3} \right) \sin \theta \quad (3.8)$$

and

$$w^* = -\frac{\partial \phi}{\partial r} = -u_\infty \left(1 - \frac{a^3}{2(a+z)^3} \right) \cos \theta \quad (3.9)$$

using the non-dimensional parameters defined in (3.1), we get the following dimensionless form of the potential flow velocity components:

$$\left. \begin{aligned} U^* &= \left(1 + \frac{1}{2(1+Z)^3} \right) \sin \theta \\ W^* &= -\left(1 - \frac{1}{(1+Z)^3} \right) \sin \theta \end{aligned} \right\} \quad (3.10)$$

Similarly the dimensionless boundary conditions can be written as:

$$\left. \begin{aligned} \text{for } Z = 0, X = 0 \text{ (Stagnation point): } & U = W = V = 0, T = 0 \\ \text{for } Z = \infty, X \geq 0 \text{ (far away from the Sphere): } & U = U^*, W = W^*, V = T = 0 \\ \text{for } Z > 0 \text{ and } X = 0 \text{ (Stagnation line): } & W = W^*, U = V = 0 \\ \text{for } Z = 0, X > 0 \text{ (Sphere surface): } & U = W = 0, V = 0 \text{ and } T=1 \text{ (UWT)} \end{aligned} \right\} \quad (3.11)$$

and $T = \frac{kt}{aq}$ (UHF)

Now having the governing equations and boundary conditions in dimensionless form, the problem is well posed and amenable to numerical solution.

3.3 Deriving Entropy Generation Equation:

The entropy generation is a result of both heat transfer and viscous dissipation. Viscous dissipation should be considered for the cases where it is not negligible. It is some times useful in thermodynamic design to learn which effect is dominant in overall entropy generation. Hence in the present study both the heat transfer and viscous entropy generation terms will be considered. The entropy generation per unit volume as given by Bejan [15] for the case with both heat transfer and viscous dissipation is expressed as:

$$\begin{aligned} \dot{S}_{gen} = \frac{k}{t^2} & \left[\left(\frac{\partial t}{\partial r} \right)^2 + \left(\frac{1}{r} \frac{\partial t}{\partial \theta} \right)^2 + \left(\frac{1}{r \sin \theta} \frac{\partial t}{\partial \phi} \right)^2 \right] \\ & \left\{ 2 \left[\left(\frac{\partial w}{\partial r} \right)^2 + \left(\frac{1}{r} \left(\frac{\partial u}{\partial \theta} \right) + \frac{w}{r} \right)^2 + \left(\frac{w}{r} + \frac{u \cos \theta}{r} \right)^2 \right] \right. \\ & + \frac{\mu}{t} \left. + \left[r \frac{\partial}{\partial r} \left(\frac{u}{r} \right) + \frac{1}{r} \frac{\partial w}{\partial \theta} \right]^2 + \right. \\ & \left. \left[r \frac{\partial}{\partial r} \left(\frac{v}{r} \right) \right]^2 + \left[\frac{\sin \theta}{r} \frac{\partial}{\partial \theta} \left(\frac{v}{\sin \theta} \right) \right]^2 \right\} \end{aligned} \quad (3.12)$$

The above equation after non-dimensionalising is given as (the details derivation is shown in Appendix-A):

$$\Rightarrow \dot{S}_{gen}^m = \frac{1}{T^2} \left[\left(\frac{\partial T}{\partial Z} \right)^2 + \frac{4}{Re^2} \left(\frac{\partial T}{\partial X} \right)^2 \right] + \frac{U_\infty^2 \mu}{a^2 t} \left\{ \begin{aligned} & 2 \left[\left(\frac{\partial W}{\partial Z} \right)^2 + \frac{4}{Re^2} \left(\frac{\partial U}{\partial X} \right)^2 + \frac{W^2}{(1+Z)^2} + \frac{4}{Re} \left(\frac{\partial U}{\partial X} \right) \frac{W}{(1+Z)} \right. \\ & \left. + \frac{W^2}{(1+Z)^2} + \frac{U^2 Cot^2 \theta}{(1+Z)^2} + \frac{2WUCot\theta}{(1+Z)^2} \right] \\ & + \left(\frac{\partial U}{\partial Z} \right)^2 + \frac{U^2}{(1+Z)^2} - 2U \frac{\partial U}{\partial Z} \frac{1}{1+Z} + \frac{4}{Re^2} \left(\frac{\partial W}{\partial X} \right)^2 \\ & + \frac{4}{Re} \left(\frac{\partial U}{\partial Z} \frac{1}{1+Z} - \frac{U}{(1+Z)^2} \right) \left(\frac{\partial W}{\partial X} \right) \end{aligned} \right\} \quad (3.13)$$

3.3.1 Constant wall temperature case:

Consider that $T = \frac{t}{t_w}$ then $\frac{\partial t}{\partial z} = t_w \frac{\partial T}{\partial z}$ and $\frac{\partial t}{\partial x} = t_w \frac{\partial T}{\partial x}$ (3.14)

Using the other non-dimensional parameters defined in the (3.1) , we get:

$$\frac{\partial t}{\partial z} = \frac{t_w}{a} \frac{\partial T}{\partial Z}, \quad \frac{\partial t}{\partial x} = \frac{2t_w}{a Re} \frac{\partial T}{\partial X} \quad \text{and} \quad \frac{\partial u}{\partial z} = \frac{U_\infty}{a} \frac{\partial U}{\partial Z} \quad (3.15)$$

After substituting the above non-dimensional terms we can write the entropy generation equation for the case of constant wall temperature as:

$$\Rightarrow \dot{S}_{gen}^m = \frac{1}{T^2} \left[\left(\frac{\partial T}{\partial Z} \right)^2 + \frac{4}{\text{Re}^2} \left(\frac{\partial T}{\partial X} \right)^2 \right] + \frac{\text{Pr} Ec_m}{T} \left\{ \begin{aligned} & 2 \left[\left(\frac{\partial W}{\partial Z} \right)^2 + \frac{4}{\text{Re}^2} \left(\frac{\partial U}{\partial X} \right)^2 + \frac{W^2}{(1+Z)^2} + \frac{4}{\text{Re}} \left(\frac{\partial U}{\partial X} \right) \frac{W}{(1+Z)} \right. \\ & \left. + \frac{W^2}{(1+Z)^2} + \frac{U^2 \text{Cot}^2 \theta}{(1+Z)^2} + \frac{2WUCot\theta}{(1+Z)^2} \right] \\ & + \left(\left(\frac{\partial U}{\partial Z} \right)^2 + \frac{U^2}{(1+Z)^2} - 2U \frac{\partial U}{\partial Z} \frac{1}{1+Z} \right) + \frac{4}{\text{Re}^2} \left(\frac{\partial W}{\partial X} \right)^2 \\ & + \frac{4}{\text{Re}} \left(\frac{\partial U}{\partial Z} \frac{1}{1+Z} - \frac{U}{(1+Z)^2} \right) \left(\frac{\partial W}{\partial X} \right) \end{aligned} \right\} \quad (3.16)$$

3.3.2 Constant Heat Flux Case:

The non-dimensional temperature is given by: $T = \frac{kt}{aq}$, i.e. $t = \frac{aqT}{k}$ (3.17)

After non-dimensionalising the entropy generation equation with the above listed terms we get,

$$\Rightarrow \dot{S}_{gen}^m = \frac{1}{T^2} \left[\left(\frac{\partial T}{\partial Z} \right)^2 + \frac{4}{\text{Re}^2} \left(\frac{\partial T}{\partial X} \right)^2 \right]$$

$$+ \frac{\text{Pr} Ec_m T_w}{T} \left\{ \begin{aligned} & 2 \left[\left(\frac{\partial W}{\partial Z} \right)^2 + \frac{4}{\text{Re}^2} \left(\frac{\partial U}{\partial X} \right)^2 + \frac{W^2}{(1+Z)^2} + \frac{4}{\text{Re}} \left(\frac{\partial U}{\partial X} \right) \frac{W}{(1+Z)} \right. \\ & \left. + \frac{W^2}{(1+Z)^2} + \frac{U^2 \text{Cot}^2 \theta}{(1+Z)^2} + \frac{2WUCot\theta}{(1+Z)^2} \right] \\ & + \left(\left(\frac{\partial U}{\partial Z} \right)^2 + \frac{U^2}{(1+Z)^2} - 2U \frac{\partial U}{\partial Z} \frac{1}{1+Z} \right) + \frac{4}{\text{Re}^2} \left(\frac{\partial W}{\partial X} \right)^2 \\ & + \frac{4}{\text{Re}} \left(\frac{\partial U}{\partial Z} \frac{1}{1+Z} - \frac{U}{(1+Z)^2} \right) \left(\frac{\partial W}{\partial X} \right) \end{aligned} \right\} \quad (3.18)$$

Where Ec_m is the modified Eckert number as given by **Haddad et al. [17]**

$$\text{And } Ec_m = \frac{U_\infty^2}{C_p t_w}, \quad \text{Pr} = \frac{\mu C_p}{k} \quad (3.19)$$

$$S_{avg} = \iint S_{gen} dx dz \quad (3.20)$$

CHAPTER IV

NUMERICAL REPRESENTATION OF THE GOVERNING

EQUATIONS

4.1 Introduction:

The governing equations developed in the previous chapter are nonlinear second order equations. Since there is no analytical solution for this type of equations, approximate methods of solution are used to solve them. The method used in this work is the finite difference approximation. In this method governing equations are first transformed to finite difference equations by dividing the domain of solution to a grid of points in the form of a mesh and the derivatives are expressed along each mesh point, referred to as a node. Therefore the differential governing equations can be written for a set of nodes of the grid converting them to algebraic equations that are linearized and then solved by an appropriate technique for matrix inversion. In this chapter, the finite difference representation of the governing equations as well as their boundary conditions are presented.

4.2 Numerical Grid:

Figure-4.1 shows the numerical grid which is used in solving the governing equations. The grid consists of two sets of perpendicular lines which represent the

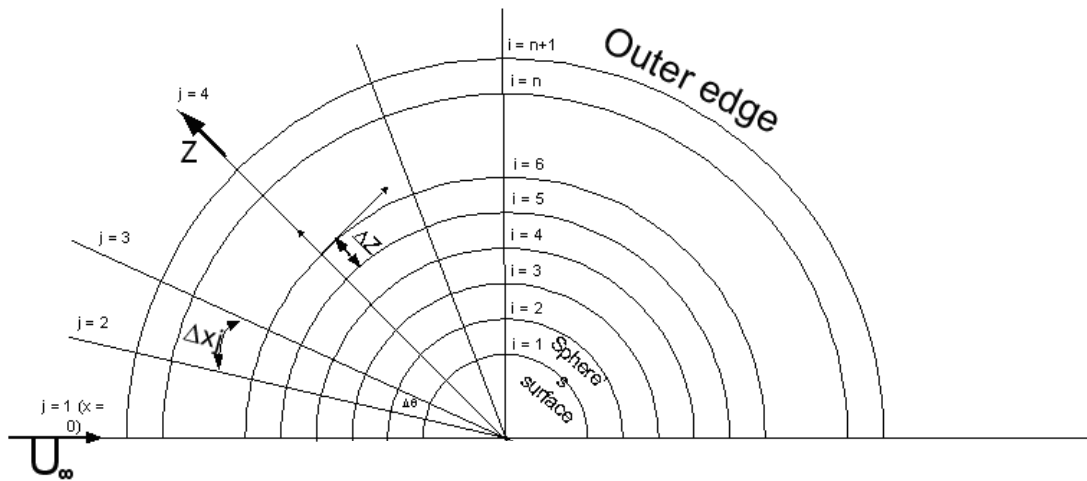


Fig 4.1: Numerical Grid

meridional direction (circles) and the radial direction (straight lines). The intersections of these lines constitute the spatial mesh points (nodes) where the solutions of the governing equations are obtained. The circles are concentric and start from the surface of the sphere with constant Z values and extend until the edge of the boundary layer is reached. The straight lines pass through the center of the sphere and each of them is a constant X -line (at a constant angle).

The spatial grid consists of $(n+1)$ points in the radial direction where the first one being on the sphere ($Z=0$) and the last one is located outside the boundary layer edge. On the other hand, the grid has $(m+1)$ meridional stations starting from $X = 0$ (at the front stagnation line) and extending until the angle of flow separation. The index i represents the radial value of the mesh points (Z direction) starting with $i = 1$ at the surface of the sphere ($Z=0$) till $i = n+1$ in the free stream while the index j represents the meridional value of the mesh points (X -direction) starting from $j=1$ at the front stagnation line ($X=0$) till the point of separation where $j = m+1$. Therefore, the finite-difference representation of the spacial mesh points will be as follows:

$$\left. \begin{aligned} Z_i &= (i-1)\Delta Z & \text{where } i &= 1, 2, 3, \dots, n+1 \\ X_j &= (j-1)\Delta X & \text{where } j &= 1, 2, 3, \dots, m+1 \end{aligned} \right\} \quad (4.1)$$

The order by which the numerical solution is obtained starts by solving the meridional momentum equation for $U_{i,j+1}$, then the continuity equation has to be solved for $W_{i,j+1}$. Therefore, the term found in the meridional momentum equation will be represented by $W_{i,j}$ (i.e. from the previous meridional step), while in the continuity equation U will be expressed as $U_{i,j+1}$ since it would have been already obtained from the solution of the preceding momentum equation. Both the U and W in the energy equation

are represented at the $(i,j+1)$ points since the flow field is assumed to be steady with constant physical properties, and energy equation is the last to solve in the pure forced convection case (after solving the momentum and continuity equation and hence the flow field components are all known). However in the mixed convection case, the energy equation is solved for a particular value of Grashof number to get the unknown values of T at all points of meridional station. Now using the computed values of T , the meridional momentum equation is solved to get the U velocity. Now the continuity equation is solved to get the W component of velocity. This procedure is repeated till the separation point is reached.

4.3 Finite difference representation of the derivatives:

The finite difference representation of the various derivatives present in the governing equations can be written as follows:

$$\left. \begin{aligned}
 \frac{\partial U}{\partial X} &= \frac{U_{i,j+1} - U_{i,j}}{\Delta X_i} \\
 \frac{\partial U}{\partial Z} &= \frac{U_{i,j+1} - U_{i-1,j+1}}{\Delta Z} \\
 \frac{\partial^2 U}{\partial Z^2} &= \frac{U_{i+1,j+1} - 2U_{i,j+1} + U_{i-1,j+1}}{\Delta Z^2} \\
 \frac{\partial W}{\partial X} &= \frac{W_{i,j+1} - W_{i,j}}{\Delta X_i} \\
 \frac{\partial W}{\partial Z} &= \frac{W_{i+1,j+1} - W_{i,j+1}}{\Delta Z}
 \end{aligned} \right\} (4.2)$$

$$\frac{\partial T}{\partial X} = \frac{T_{i,j+1} - T_{i,j}}{\Delta X_i}$$

$$\frac{\partial T}{\partial Z} = \frac{T_{i+1,j+1} - T_{i,j+1}}{\Delta Z}$$

$$\frac{\partial^2 T}{\partial Z^2} = \frac{T_{i+1,j+1} - 2T_{i,j+1} + T_{i-1,j+1}}{\Delta Z^2}$$

4.4 Finite difference representations of governing equations:

4.4.1 Finite difference representation of meridional momentum equation:

$$U \frac{\partial U}{\partial X} + \frac{\text{Re}W}{2} \frac{\partial U}{\partial Z} = U^* \frac{\partial U}{\partial X} + \frac{\partial^2 U}{\partial Z^2} \pm \frac{\text{Gr}}{8 \text{Re}} T \sin \theta \quad (4.3)$$

$$\Rightarrow U_{i,j} \frac{U_{i,j+1} - U_{i,j}}{\Delta X_i} + \frac{\text{Re}W_{i,j}}{2} \frac{U_{i+1,j+1} - U_{i-1,j+1}}{2\Delta Z} =$$

$$\frac{9}{8} \sin(j\Delta\theta) \cdot \text{Re} \cos(j\Delta\theta) + \frac{U_{i+1,j+1} - 2U_{i,j+1} + U_{i-1,j+1}}{\Delta Z^2} \pm \frac{\text{Gr}}{4 \text{Re}} T_{i,j+1} \sin(j\Delta\theta) \quad (4.4)$$

Rearranging equation (4.6):

$$U_{i-1,j+1} \left(\frac{-W_{i,j} \text{Re}}{4\Delta Z} - \frac{1}{\Delta Z^2} \right) + U_{i,j+1} \left(\frac{U_{i,j}}{\Delta X_i} + \frac{2}{\Delta Z^2} \right) + U_{i+1,j+1} \left(\frac{W_{i,j} \text{Re}}{4\Delta Z} - \frac{1}{\Delta Z^2} \right) = \frac{(U_{i,j})^2}{\Delta X_i}$$

$$+ \frac{9}{8} \text{Re} \sin(j\Delta\theta) \cos(j\Delta\theta) \pm \frac{\text{Gr}}{4 \text{Re}} T_{i,j+1} \sin(j\Delta\theta) \quad (4.5)$$

$$\text{let: } C(i) = \left(\frac{-W_{i,j} \text{Re}}{4\Delta Z} - \frac{1}{\Delta Z^2} \right) \quad (4.6)$$

$$A(i) = \left(\frac{U_{i,j}}{\Delta X_i} + \frac{2}{\Delta Z^2} \right)$$

$$B(i) = \left(\frac{W_{i,j} \text{Re}}{4\Delta Z} - \frac{1}{\Delta Z^2} \right)$$

$$D(i) = \frac{(U_{i,j})^2}{\Delta X_i} + \frac{9}{8} \text{Re} \sin(j\Delta\theta) \cos(j\Delta\theta) \pm \frac{Gr}{4 \text{Re}} T_{i,j+1} \sin(j\Delta\theta)$$

Now the meridional momentum equation can be written as:

$$\begin{array}{l}
 \text{For } i = 1: \quad C_1 U_0 + A_1 U_1 + B_1 U_2 = D_1 \\
 \text{For } I = 2: \quad C_2 U_1 + A_2 U_2 + B_2 U_3 = D_2 \\
 \text{For } I = 3: \quad C_3 U_2 + A_3 U_3 + B_3 U_4 = D_3 \\
 \text{For } I = n: \quad C_n U_{n-1} + A_n U_n + B_n U_{n+1} = D_n
 \end{array}
 \quad \left. \vphantom{\begin{array}{l} \\ \\ \\ \\ \end{array}} \right\} \quad (4.7)$$

These equations can be expressed in matrix form as:

$$\begin{bmatrix}
 A_1 & B_1 & & & & & & & & & & \\
 C_2 & A_2 & B_2 & & & & & & & & & \\
 & C_3 & A_3 & B_3 & & & & & & & & \\
 & & \cdot & \cdot & \cdot & & & & & & & \\
 & & & \cdot & \cdot & \cdot & & & & & & \\
 0 & & & & \cdot & \cdot & \cdot & & & & & \\
 & & & & & & & C_{n-1} & A_{n-1} & B_{n-1} & & \\
 & & & & & & & C_n & A_n & & &
 \end{bmatrix}
 \begin{bmatrix}
 U_1 \\
 U_2 \\
 U_3 \\
 \cdot \\
 \cdot \\
 \cdot \\
 U_{n-1} \\
 U_n
 \end{bmatrix}
 =
 \begin{bmatrix}
 D_1 \\
 D_2 \\
 D_3 \\
 \cdot \\
 \cdot \\
 \cdot \\
 D_{n-1} \\
 D_n
 \end{bmatrix}
 \quad (4.8)$$

where $D_n = D_n - B_n U_{n+1}$

4.4.2 Finite difference representation of continuity equation:

$$\frac{\partial U}{\partial X} + \frac{\text{Re} \partial W}{2 \partial Z} + \frac{U}{R} \frac{dR}{dX} + \text{Re} \frac{W}{1+Z} = 0 \quad (4.9)$$

$$\Rightarrow \frac{U_{i+1,j+1} + U_{i,j+1} - U_{i+1,j} - U_{i,j}}{2\Delta X_{i+1/2}} + \frac{\text{Re} W_{i+1,j+1} - W_{i,j+1}}{2 \Delta Z} + \frac{\text{Re}(W_{i+1,j+1} + W_{i,j+1})}{2(1+Z_{i+1/2})} + \frac{(U_{i+1,j+1} + U_{i,j+1}) \text{Re} \cot(j\Delta\theta)}{4(1+Z_{i+1/2})} = 0 \quad (4.10)$$

Rearranging:

$$W_{i,j+1} \frac{\text{Re} \left(\frac{1}{1+Z_{i+1/2}} - \frac{1}{\Delta Z} \right)}{2} + W_{i+1,j+1} \frac{\text{Re} \left(\frac{1}{1+Z_{i+1/2}} + \frac{1}{\Delta Z} \right)}{2} = - \frac{U_{i+1,j+1} + U_{i,j+1} - U_{i+1,j} - U_{i,j}}{2\Delta X_{i+1/2}} - \frac{(U_{i+1,j+1} + U_{i,j+1}) \text{Re} \cot(j\Delta\theta)}{4(1+Z_{i+1/2})} \quad (4.11)$$

$$\text{let: } A(i) = \frac{\text{Re} \left(\frac{1}{1+Z_{i+1/2}} - \frac{1}{\Delta Z} \right)}{2} \quad (4.12)$$

$$B(i) = \frac{\text{Re} \left(\frac{1}{1+Z_{i+1/2}} + \frac{1}{\Delta Z} \right)}{2}$$

$$D(i) = - \frac{U_{i+1,j+1} + U_{i,j+1} - U_{i+1,j} - U_{i,j}}{2\Delta X_{i+1/2}} - \frac{(U_{i+1,j+1} + U_{i,j+1}) \text{Re} \cot(j\Delta\theta)}{4(1+Z_{i+1/2})}$$

Equations can be represented for a given j as:

$$\text{for } i = 1: \quad A_1 W_1 + B_1 W_2 = D_1 \quad (W_1 = 0 \text{ for sphere surface}) \quad (4.13)$$

$$\text{for } i = 2: \quad A_2 W_2 + B_2 W_3 = D_2$$

$$\text{for } i = n-1: \quad A_{n-1} W_{n-1} + B_{n-1} W_n = D_{n-1}$$

$$\text{for } i = n: \quad A_n W_n + B_n W_{n+1} = D_n$$

4.4.3 Finite Difference representation of energy equation:

$$U \frac{\partial T}{\partial X} + \frac{\text{Re}W}{2} \frac{\partial T}{\partial Z} = \frac{1}{\text{Pr}} \frac{\partial^2 T}{\partial Z^2} \quad (4.14)$$

$$U_{i,j} \frac{T_{i,j+1} - T_{i,j}}{\Delta X_i} + \frac{\text{Re}}{2} W_{i,j} \frac{T_{i+1,j+1} - T_{i-1,j+1}}{2\Delta Z} = \frac{1}{\text{Pr}} \frac{T_{i+1,j+1} - 2T_{i,j+1} + T_{i-1,j+1}}{(\Delta Z)^2} \quad (4.15)$$

Rearranging:

$$\begin{aligned} T_{i-1,j+1} \left(-\frac{\text{Re Pr } W_{i,j+1}}{4\Delta Z} - \frac{1}{\Delta Z^2} \right) + T_{i,j+1} \left(\frac{2}{\Delta Z^2} + \frac{U_{i,j} \text{ Pr}}{\Delta X_i} \right) \\ + T_{i+1,j+1} \left(\frac{\text{Re Pr } W_{i,j+1}}{4\Delta Z} - \frac{1}{\Delta Z^2} \right) = \frac{U_{i,j} \text{ Pr } T_{i,j}}{\Delta X_i} \end{aligned} \quad (4.16)$$

for a given j , let:

$$C(i) = -\frac{\text{Re Pr } W_{i,j+1}}{4\Delta Z} - \frac{1}{\Delta Z^2} \quad (4.17)$$

$$A(i) = \frac{2}{\Delta Z^2} + \frac{U_{i,j} \text{ Pr}}{\Delta X_i}$$

$$B(i) = \frac{\text{Re Pr } W_{i,j+1}}{4\Delta Z} - \frac{1}{\Delta Z^2}$$

$$D(i) = \frac{U_{i,j} \text{ Pr } T_{i,j}}{\Delta X_i}$$

Hence the equation (4.16) can be written as:

$$B(i) T_{i+1,j+1} + A(i) T_{i,j+1} + C(i) T_{i-1,j+1} = D(i) \quad (4.18)$$

$$\text{For } i = 1: \quad B_1 T_2 + A_1 T_1 + C_1 T_0 = D_1$$

$$T_{1,j} = 1 \text{ (UWT) and } T_w = \frac{-1}{\Delta T / \Delta Z} \text{ (UHF)}$$

4.6 Finite difference representation of the entropy generation equation:

4.6.1 Uniform wall temperature case:

As soon as the temperature and velocity gradients are available in the domain, the entropy generation is calculated.

The non dimensional temperature for the case of constant wall temperature as given earlier is:

$$T = \frac{t}{t_w}$$

The entropy equation for the case of uniform wall temperature case from equation (3.20) and using finite difference terms of equation (4.2), is given as:

$$\begin{aligned}
\dot{S}_{gen}^m = & \frac{1}{T_{i,j}^2} \left[\left(\frac{T_{i+1,j+1} - T_{i,j+1}}{\Delta Z} \right)^2 + \frac{4}{\text{Re}^2} \left(\frac{T_{i,j+1} - T_{i,j}}{\Delta X_i} \right)^2 \right] \\
& + \frac{\text{Pr} Ec_m}{T_{i,j}} \left\{ \left[\left(\frac{W_{i+1,j+1} - W_{i,j+1}}{\Delta Z} \right)^2 + \frac{4}{\text{Re}^2} \left(\frac{U_{i,j+1} - U_{i,j}}{\Delta X_i} \right)^2 + \frac{2W_{i,j}^2}{(1+Z_{i,j})^2} \right. \right. \\
& \left. \left. + \frac{4}{\text{Re}} \left(\frac{U_{i,j+1} - U_{i,j}}{\Delta X_i} \right) \frac{W_{i,j}}{(1+Z_{i,j})} \right. \right. \\
& \left. \left. + \frac{U_{i,j}^2 \text{Cot}^2(J\Delta\theta)}{(1+Z_{i,j})^2} + \frac{2W_{i,j}U_{i,j} \text{Cot}(J\Delta\theta)}{(1+Z_{i,j})^2} \right] \right. \\
& \left. + \left(\frac{U_{i,j+1} - U_{i-1,j+1}}{\Delta Z} \right)^2 + \frac{U_{i,j}^2}{(1+Z_{i,j})^2} - 2U_{i,j} \left(\frac{U_{i,j+1} - U_{i-1,j+1}}{\Delta Z} \right) \frac{1}{1+Z_{i,j}} \right. \\
& \left. + \frac{4}{\text{Re}^2} \left(\frac{W_{i,j+1} - W_{i,j}}{\Delta X_i} \right)^2 \right. \\
& \left. + \frac{4}{\text{Re}} \left(\left(\frac{U_{i,j+1} - U_{i-1,j+1}}{\Delta Z} \right) \frac{1}{1+Z_{i,j}} - \frac{U_{i,j}}{(1+Z_{i,j})^2} \right) \left(\frac{W_{i,j+1} - W_{i,j}}{\Delta X_i} \right) \right\} \quad (4.21)
\end{aligned}$$

4.6.2 Uniform heat flux case:

The non-dimensional temperature for the case of constant heat flux as given earlier is:

$$T = \frac{kt}{aq}, \text{ i.e. } t = \frac{aqT}{k}$$

The entropy generation equation is given by:

$$\begin{aligned}
\dot{S}_{gen}^m = & \frac{1}{T_{i,j}^2} \left[\left(\frac{T_{i+1,j+1} - T_{i,j+1}}{\Delta Z} \right)^2 + \frac{4}{\text{Re}^2} \left(\frac{T_{i,j+1} - T_{i,j}}{\Delta X_i} \right)^2 \right] \\
& + \frac{\text{Pr} Ec_m T_{wi,j}}{T_{i,j}} \left\{ \left[\left(\frac{W_{i+1,j+1} - W_{i,j+1}}{\Delta Z} \right)^2 + \frac{4}{\text{Re}^2} \left(\frac{U_{i,j+1} - U_{i,j}}{\Delta X_i} \right)^2 + \frac{2W_{i,j}^2}{(1+Z_{i,j})^2} \right. \right. \\
& \left. \left. + \frac{4}{\text{Re}} \left(\frac{U_{i,j+1} - U_{i,j}}{\Delta X_i} \right) \frac{W_{i,j}}{(1+Z_{i,j})} \right. \right. \\
& \left. \left. + \frac{U_{i,j}^2 \text{Cot}^2(J\Delta\theta)}{(1+Z_{i,j})^2} + \frac{2W_{i,j} U_{i,j} \text{Cot}(J\Delta\theta)}{(1+Z_{i,j})^2} \right] \right. \\
& \left. + \left(\frac{U_{i,j+1} - U_{i-1,j+1}}{\Delta Z} \right)^2 + \frac{U_{i,j}^2}{(1+Z_{i,j})^2} - 2U_{i,j} \left(\frac{U_{i,j+1} - U_{i-1,j+1}}{\Delta Z} \right) \frac{1}{1+Z_{i,j}} \right. \\
& \left. + \frac{4}{\text{Re}^2} \left(\frac{W_{i,j+1} - W_{i,j}}{\Delta X_i} \right)^2 \right. \\
& \left. + \frac{4}{\text{Re}} \left(\left(\frac{U_{i,j+1} - U_{i-1,j+1}}{\Delta Z} \right) \frac{1}{1+Z_{i,j}} - \frac{U_{i,j}}{(1+Z_{i,j})^2} \right) \left(\frac{W_{i,j+1} - W_{i,j}}{\Delta X_i} \right) \right\} \quad (4.22)
\end{aligned}$$

CHAPTER V

SOLUTION METHODOLOGY

5.1 Introduction:

This chapter is aimed at presenting the detailed method of solution for the problem under investigation where the finite difference form of the derived governing equations written at each node.

Wide range of controlling parameters like Reynolds number, Grashof number and Eckert number are used to study their effect on the velocity, temperature and entropy generation variation. As soon as the velocity and temperature gradients are obtained, entropy generation is calculated.

The numerical scheme in the whole domain is obtained by marching in the meridional(X) direction starting from the front stagnation point where the velocity and temperature profiles are assumed to be known. The solution then proceeds in this direction step by step till the point of flow separation is reached. At each meridional station, system of equations are solved to obtain U , W and then T along this line starting from the surface of the sphere up to the edge of the boundary layer, which is obtained by comparing the value and tangent of meridional velocity component with its free stream value. Upon obtaining the required velocity and temperature profiles, the entropy generation is calculated.

The average entropy generation at each meridional station is calculated which is the local average. Then the solution is advanced to the next meridional station. The process is repeated till the separation point is reached. Total average is the average of entropy generation for the whole domain from the front stagnation line till the separation point.

5.2 Numerical Grid:

The numerical grid parameters are selected to be variable and have small values in the meridional direction especially at the points where high gradients are expected as in the case of the flow near the separation point. Along each meridional station, the grid size is assumed constant ($\Delta Z = 0.001$) where a minimum number of mesh points was given and the convergence criterion was tested at the outer point, if the convergence criterion was met, the solution proceeds to the next meridional step, otherwise the number of steps is increased by 2 and the solution is repeated along this meridional step. This process is repeated till the criterion which is presented in the next section is met. The solution proceeds in the marching X direction with equal grid size (1^0) until the point of separation is reached then the program adjusts itself and return one meridional step back to reduce the X-direction grid size to (0.1^0) in order to accurately determine the point of flow separation.

5.3 Criteria for Convergence:

Two criteria are supposed to be met during the solution, the first is at each meridional step to determine the boundary layer thickness whereas the other is to determine the point of external flow separation.

For the flow around a solid sphere, a minimum number of mesh points in the Z-direction for a certain meridional step was chosen to be 20 ($n=20$). Upon calculating the meridional velocity component along this line, the tangent of the velocity at the upper most point was calculated and the slope of the velocity ($\partial U / \partial Z$) is calculated at the uppermost point ($n+1$). Then the slope of the potential flow around a sphere is calculated at the same point and the two values are compared. If both slopes are matched within a certain arbitrarily specified tolerance (a value of 0.005 was chosen in the present work) the solution is supposed to be convergent and this would determine the edge of the boundary layer. Otherwise, the number of radial steps (n) is increased by two and the procedure is repeated until the matching criterion is met.

Fluid particles over the sphere accelerate in the region $0 \leq \theta \leq 90$ and decelerate in the region where $\theta > 90$, hence the pressure decreases in the accelerated region and then increases in the decelerated region [46]. Since the external pressure is imposed at the boundary layer, the transformation of the pressure into kinetic energy takes place in the accelerated region and a great deal of the kinetic energy of the particles adjacent to the wall is consumed to move against the friction forces. In the decelerated region, the remainder of the kinetic energy is too small to keep those fluid particles moving in the

region of high pressure, so, they would be eventually arrested and the external pressure would force them to move in the opposite direction separating from the surface of the sphere and the point of flow separation can be detected by the condition that the velocity gradient at the wall vanished or $(\partial U / \partial Z = 0)$. Therefore the flow separation would be accompanied by a vanishing velocity gradient; a large boundary layer thickness due to the increase in the number of radial steps is required to satisfy the matching criterion at the edge of the boundary layer and a larger value to the radial velocity components because of the increasing outward direction of the flow.

A computer code is developed such that a constant meridional step is followed in the marching X-direction until flow separation occurs where zero or negative unexpected value of U can be obtained. Then a finer mesh is used in X-direction (i.e. for ΔX) and the point of separation is obtained.

5.4 Solution procedure:

The governing finite difference equations obtained in Chapter IV are governed by some controlling parameters, namely, Reynolds number, Grashof number, Prandtl number and Eckert number. So these controlling parameters should be fixed each time the program is run. The solution starts by selecting appropriate values for these parameters. For forced convection problem the solution proceeds as follows:

1. The program starts in the marching X-direction, the variables at the first meridional station ($j = 1$, i.e. at the front stagnation line) are known where boundary layer thickness is assumed zero. Hence U , W , and T are known and specified at this first station ($U = 0$, $T = 1$, and W is obtained from the potential flow distribution). So the code starts to obtain the solutions at the line $j = 2$ assuming a number of radial grid points of 20.
2. In the forced convection regime, the finite difference equations arranged in a form of a matrix for U values are solved first and then followed by solving the continuity equation to get W values.
3. The matching criterion at the uppermost point is checked. If the criterion is not met, the number 'n' is increased by 2 and the solution is repeated again.
4. Steps 2 and 3 are repeated till the convergence criterion is met. Then the energy equation is solved and the temperature distribution along this line ($X = \text{constant}$) is obtained.
5. The obtained values are reported and prepared to be the initial values of the next meridional step.
6. The local average entropy generation at each meridional station is calculated and reported.
7. The solution then proceeds in the marching X-direction repeating the same previous steps (2 through 5) until the separation point is reached where finer mesh is used (smaller increments in X-direction) and the angle of separation is estimated as explained previously in section 5.3.

8. After obtaining the velocity and temperature profiles, the entropy generation can now be calculated for the given controlling parameters. The local entropy generation is first calculated at each meridional station.
9. Then the total average entropy generation is calculated by integrating over the whole domain from the stagnation line till the separation point.

In the mixed convection regime, the solution methodology is as follows:

1. The program starts in the marching X-direction, the variables at the first meridional station ($j = 1$, i.e. at the front stagnation line) are known where boundary layer thickness is assumed zero. Hence U , W , and T are known and specified at this first station ($U = 0$, $T = 1$, and W is obtained from the potential flow distribution). So the code starts to obtain the solutions at the line $j = 2$ assuming a number of radial grid points of 20.
2. In the mixed convection regime, the finite difference equations arranged in a form of a matrix for energy equation to get T values.
3. After obtaining the T values, the meridional momentum equation is solved to get the U values.
4. After getting the values of U , the continuity equation is solved to obtain the W velocity component.
5. The convergence criterion is checked as described previously for forced convection regime, and then the obtained values are reported and prepared to be the initial values of the next meridional step.
6. The local entropy generation at each meridional station is calculated and reported.

7. The solution then proceeds in the marching X-direction repeating the same previous steps (2 through 6) until the separation point is reached where finer mesh is used (smaller increments in X-direction) and the angle of separation is estimated as explained previously in section 5.3.
8. After obtaining the velocity and temperature profiles, the entropy generation can now be calculated for the given controlling parameters. The local average entropy generation is first calculated at each meridional station.
9. Then the total average entropy generation is calculated by integrating over the whole domain from the stagnation line till the separation point.

CHAPTER VI

RESULTS AND DISCUSSIONS FOR THE FORCED CONVECTION

6.1 Introduction:

In this chapter, the results of solving the governing equations and computing the local and average entropy generation are presented for the forced convection case. These clarify the effect of the controlling parameters like Reynolds number, Grashof number and Eckert number on the flow field and entropy generation.

6.2 Range of different controlling parameters:

The different controlling parameters like Reynolds number, Grashof number and Eckert number considered in this study are presented and their range is justified in this section.

Range of Reynolds number: The range of Re considered here is $10^3 < Re < 10^5$. The value of Re in this range is large enough to justify the use the boundary layer approximation but small enough to keep the flow laminar. The transition from laminar to turbulent for fluid flow over a sphere starts from $Re = 3 \times 10^5$ and flow become fully turbulent for $Re = 5 \times 10^5$ [49].

As seen from the Fig-6.1, at $Re = 3 \times 10^5$ the coefficient of drag over the sphere decreases abruptly which marks the start of flow transition.

Range of Grashof number: The range of Grashof number selected in this study is $-10^9 < Gr < 10^9$. This range is selected to represent cases of aiding and opposing flow and to keep the flow laminar [6].

Range of modified Eckert number: $10^{-7} < Ec_m < 10^{-1}$. The *Eckert number* is the ratio of kinetic energy to enthalpy change across a layer. It's a measure of importance of viscous dissipation. A large *Eckert number* implies a large kinetic energy available to be converted to heat through viscous dissipation; for a smaller Re , more energy will be dissipated. The heat generated by dissipation is relatively important if the temperature difference in the flow field is small to begin with. Eckert number is important in studying the aerodynamic heating in supersonic boundary layers, or high speed gas bearings.

This range of Ec_m is selected to keep the flow incompressible [17]. As the Eckert number is increased, the Mach number of the flow increases, and at $Ma \geq 0.3$ the flow becomes compressible. Table 6.1 gives the different values of Eckert number resulting from different combination of Temperature (T) and Mach number (M). As seen from this table, we can say that the range of Ec_m considered in this study, that is $10^{-7} < Ec_m < 10^{-1}$, to keep the flow incompressible is justified. And for $Ec_m > 10^{-1}$ the flow becomes compressible.

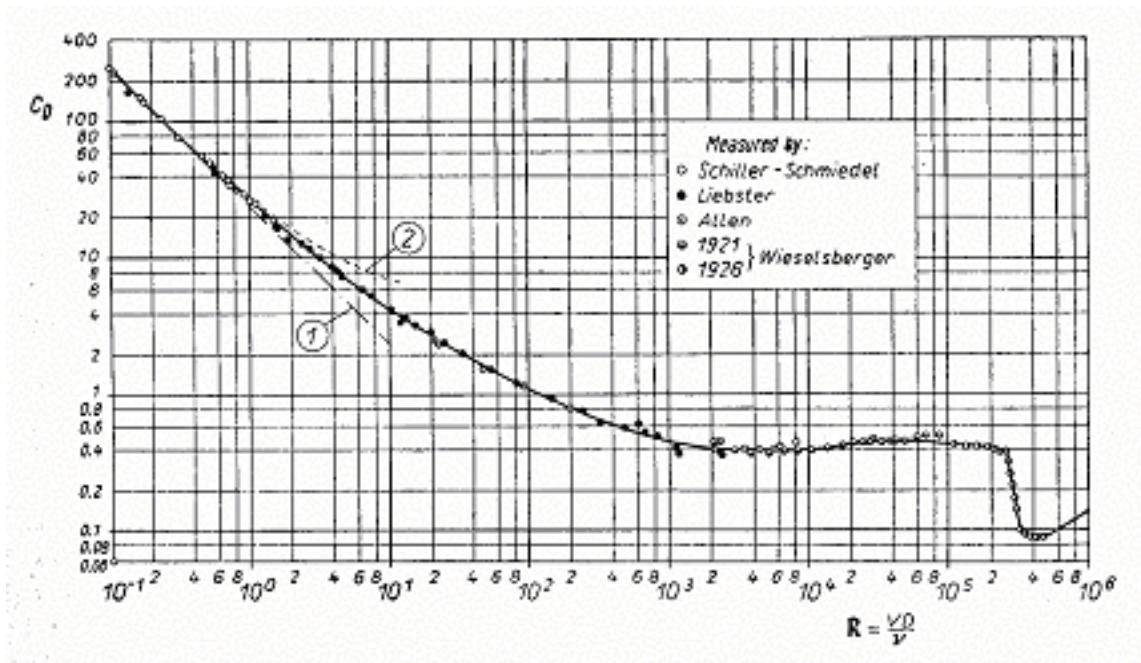


Fig.6.1: Transition of flow over a sphere from laminar to turbulent [49]

Table-6.1: Values of Ec_m for different combinations of Mach number and Temperatures

(for air):

M	T (K)	ΔT	$Ec = M^2 R T / C_v \Delta T$
0.3	400	100	0.144705882
0.3	500	200	0.090441176
0.3	600	300	0.072352941
0.3	800	500	0.057882353
0.3	1300	1000	0.047029412
0.2	400	100	0.064313725
0.2	500	200	0.040196078
0.2	600	300	0.032156863
0.2	800	500	0.02572549
0.2	1300	1000	0.020901961
0.1	400	100	0.016078431
0.1	500	200	0.01004902
0.1	600	300	0.008039216
0.1	800	500	0.006431373
0.1	1300	1000	0.00522549
0.05	400	100	0.004019608
0.05	500	200	0.002512255
0.05	600	300	0.002009804
0.05	800	500	0.001607843
0.05	1300	1000	0.001306373

6.3 Results for uniform wall temperature (Forced convection case):

6.3.1 Meridional velocity profiles:

Figure 6.2 shows examples of the meridional velocity profiles at three selected meridional locations ($\theta = 30^\circ$, 60° and 90°) along the radial distance (Z). It starts with zero value at the surface of the sphere ($Z=0$), which is the no slip condition, till it matches the free stream velocity thus representing the edge of the boundary layer surrounding the sphere. The figure also shows the increase in the boundary layer thickness as the fluid

moves further over the sphere surface in the meridional direction illustrating the boundary layer development.

Figure 6.3 shows the effect of Re on the boundary layer thickness. The higher the value of Re, the thinner is the boundary layer. This is attributed to high velocity gradients at higher Re requiring less boundary layer thickness (less distance) for the velocity to drop from its free stream value at the edge of the boundary layer to its zero value at the surface of the sphere. It is worth mentioning that as the Reynolds number increases, the rate of transfer of momentum increases too leading to higher velocity gradients and hence less boundary layer thickness.

Figure 6.4a shows the variation of the meridional velocity with θ at different Z-locations for $Re=10^4$. The figure clearly shows that the meridional U- velocity is zero at the stagnation point and is higher at some angles and decreases as it approaches the separation point. It also shows that the velocity at the surface of sphere has a zero value, which shows the no slip condition.

For the sake of validation of the present code, a comparison between this study and previous studies is shown figures 6.4b and 6.4c. Figure 6.4b shows the velocity profile for $\theta = 60^\circ$ and $Re = 10^4$. Figure 6.4c shows the wall shear stress in meridional direction for a given Reynolds number for the present study and compared with the one by Schlichting [49]. It can be clearly seen that the code used in present study is in good agreement with the previous published results.

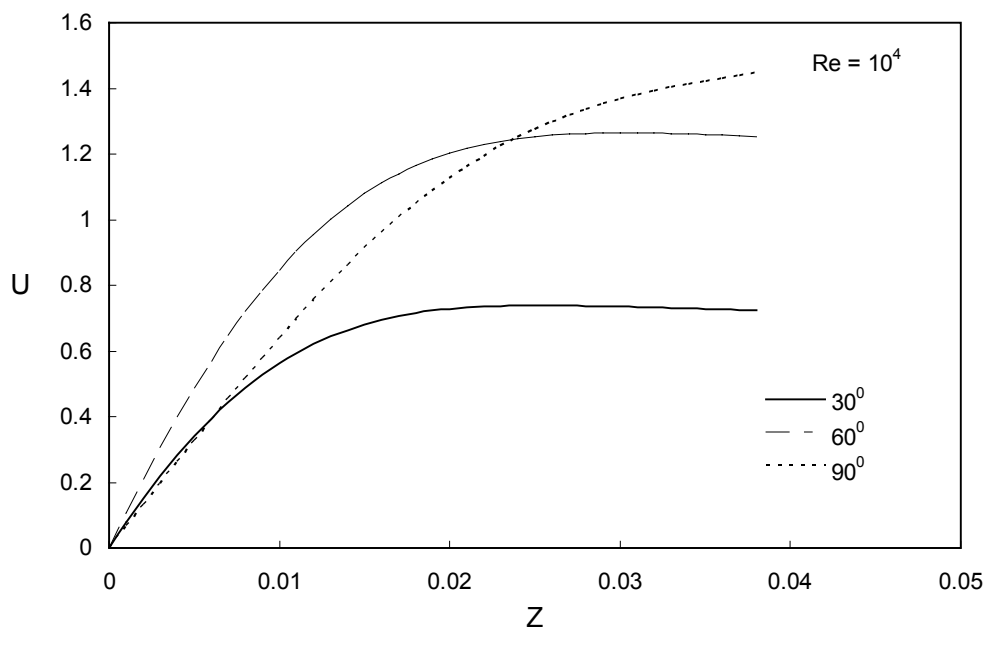


Fig 6-2: Meridional Velocity Profile at different meridional locations for a given Reynolds number

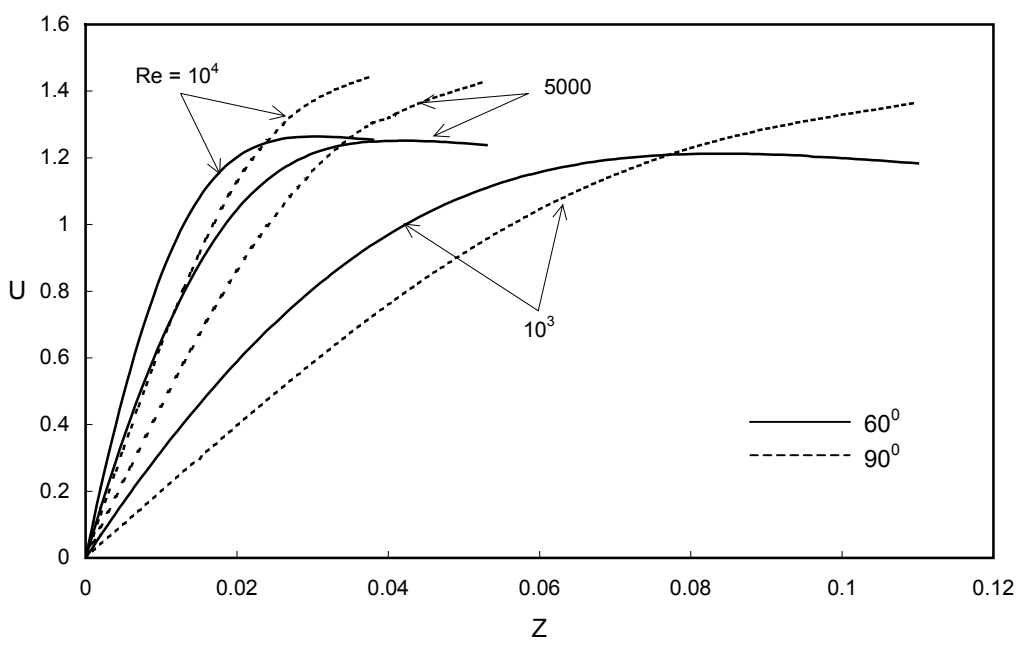


Fig 6-3: Effect of Reynolds number on Meridional velocity profiles at two different meridional stations

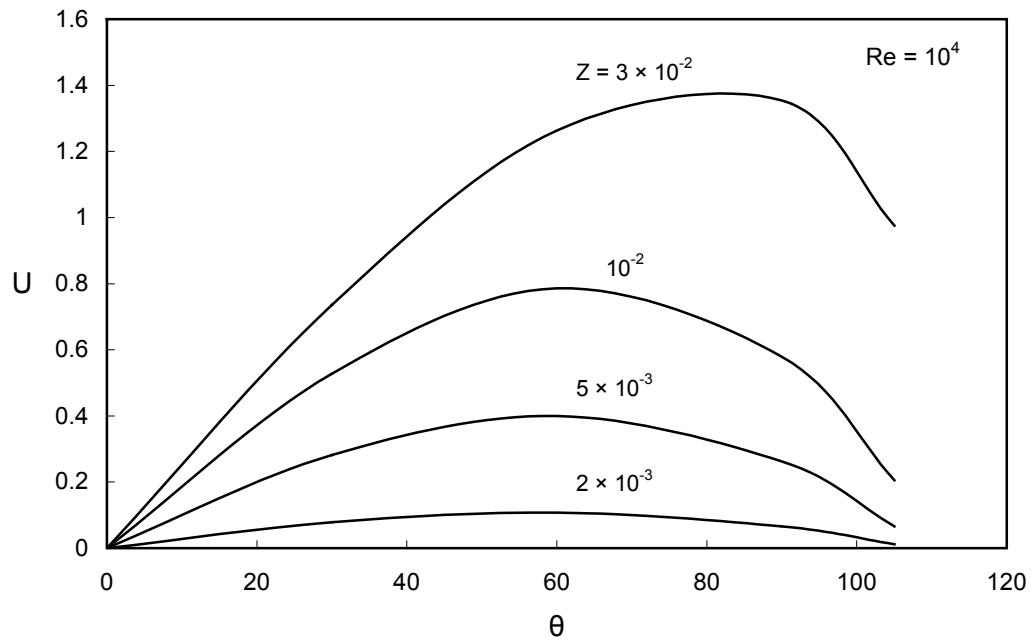


Fig 6-4a: Meridional Velocity profile over the sphere surface at different radial locations

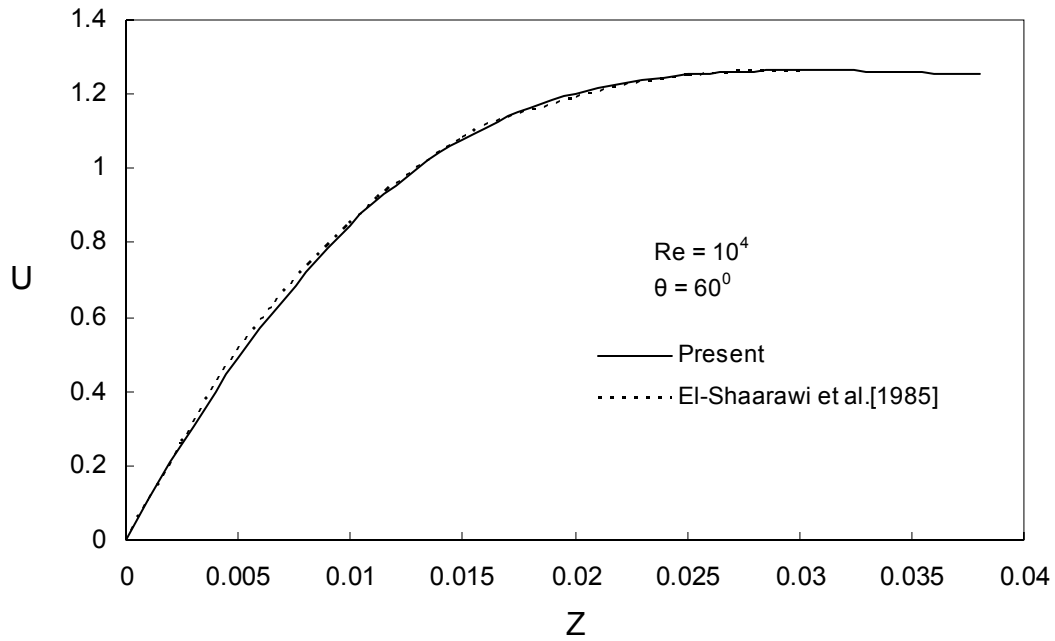


Fig 6-4b: Comparing the U-velocity of present work with that of previous work

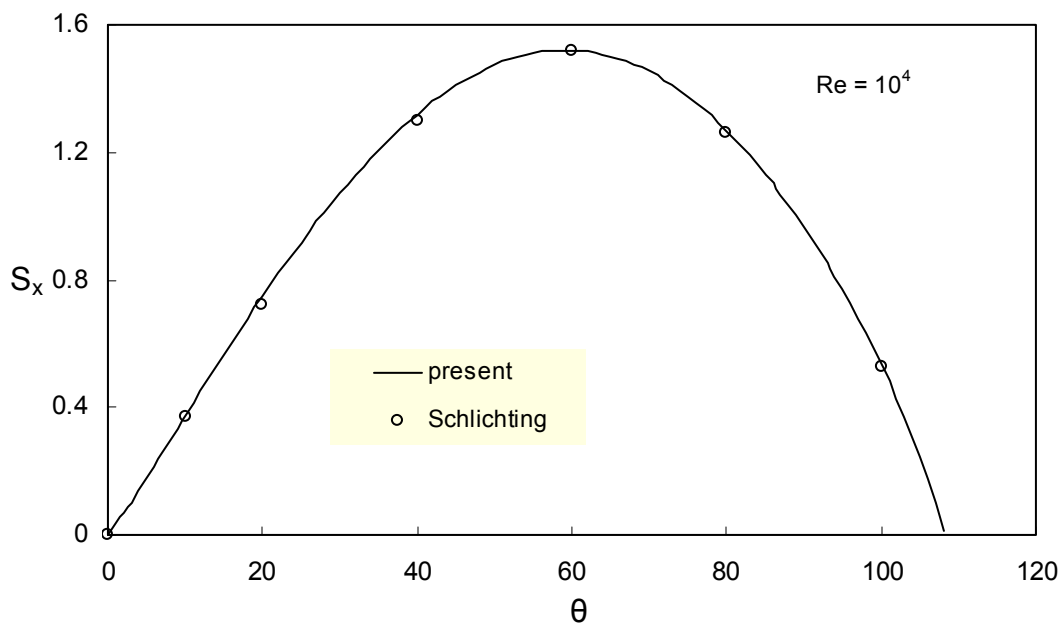


Fig 6-5: Wall shear stress in meridional direction for a given Reynolds number

6.3.2 Radial Velocity Profiles:

Figure 6.5 presents the developing radial velocity component, W , corresponding to different meridional stations (angles) $\theta = 30^\circ, 60^\circ, 90^\circ, 105^\circ$ for a given Reynolds number ($Re = 10000$). It is clear that all these profiles are starting with zero value at the surface of the sphere (no fluid is crossing the boundaries, i.e. no suction or blowing). Profiles are negative for meridional angles $< 90^\circ$ while they have positive values for $\theta > 90^\circ$. This behavior shows that the radial component of velocity is pushing the boundary layer fluid toward the sphere's surface in the accelerated region of the flow. Whereas in the adverse region ($\theta > 90^\circ$), the tendency changes to blowing of the fluid and hence the radial component of velocity assists increasing the boundary layer thickness till the maximum thickness is reached at the point where the flow separates.

6.3.3 Temperature Profile:

Figure 6.7 presents the temperature profile for some selected values of meridional stations. This figure shows the variation of the temperature profiles as the boundary layer increases along the surface of the sphere until the maximum boundary layer thickness is encountered near the point of flow separation. As expected, the wall of the sphere is at the maximum dimensionless temperature which is equal to one, and as we move away from the sphere, the temperature decreases.

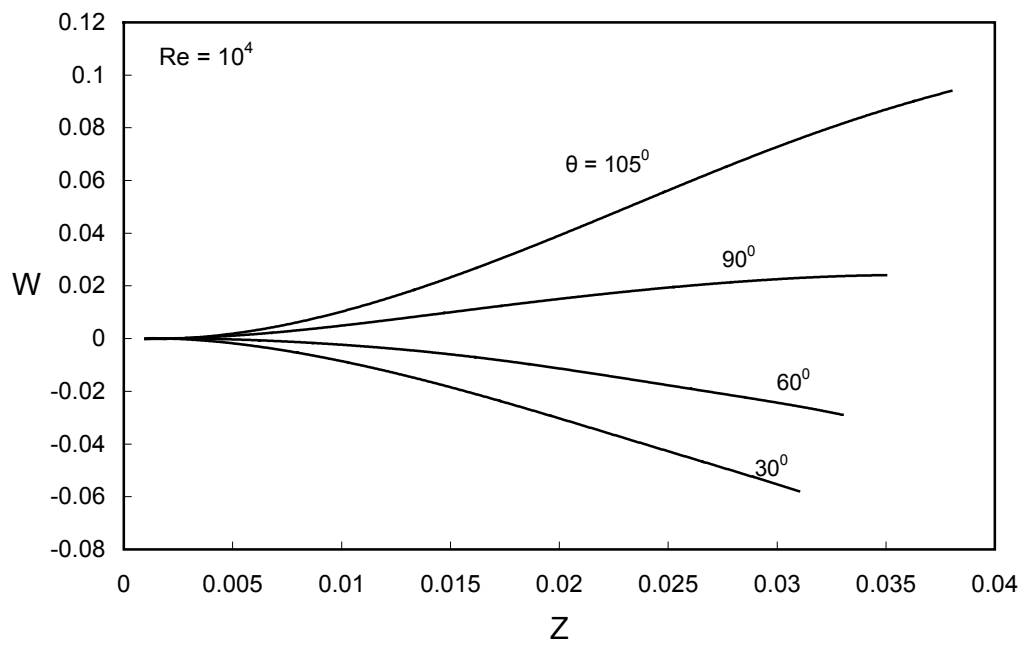


Fig 6-6: Radial velocity profile at different meridional locations

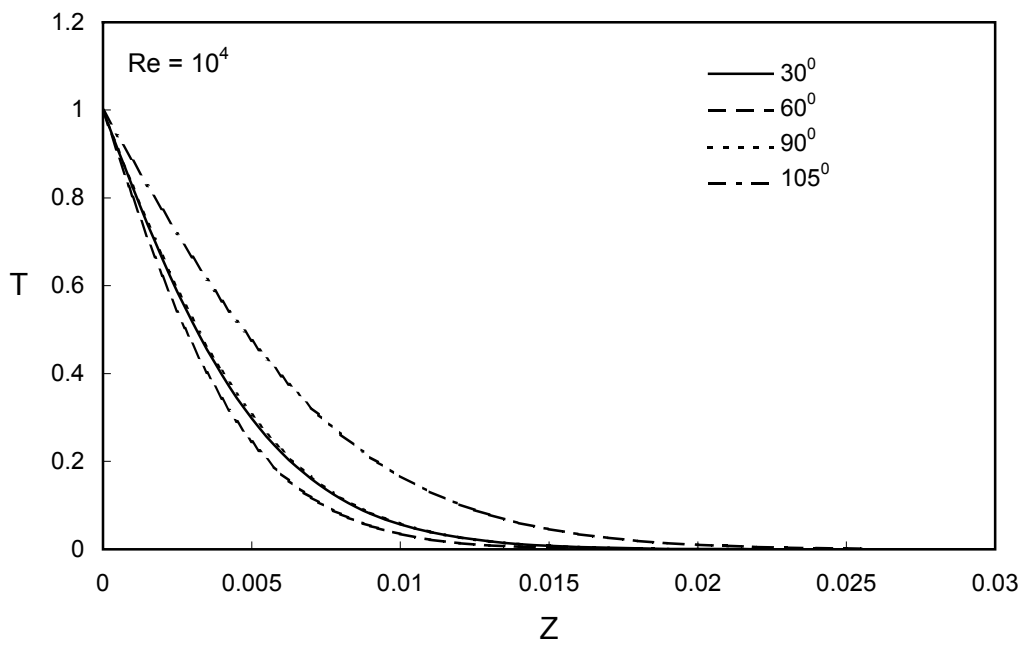


Fig 6-7: Temperature profile at different meridional locations for a given Reynolds number

6.3.4 Local entropy generation profiles:

As given by Bejan [45] the range of entropy generation number is very large, thus logarithmic scale is used in presenting the results.

Figure 6.8 shows the variation of heat transfer entropy generation with the radial distance at different meridional stations (angles), $\theta = 30^\circ, 60^\circ, 90^\circ, 105^\circ$ for a given Reynolds number ($Re = 10^4$) and modified Eckert number ($Ec_m = 10^{-2}$). This figure shows that as we move away from the surface of the sphere (i.e. increasing the value of Z), the entropy generated due to heat transfer increases. However, the rate of entropy generation is higher near the surface than far away, this is due to increase in temperature gradients as one move towards the surface. This rate approaches zero as we move away from the sphere, since the temperature gradient is zero outside the thermal boundary layer. Furthermore, the entropy generation is higher at the edge of the boundary layer than at the surface because as we move away from the sphere surface the temperature is decreasing but this temperature term ($1/T^2$) is multiplied to the entropy generation term as seen in equation (3.20), due to which the entropy generation is higher as temperature decreases. Figure 6.9 shows the same variation but for different Reynolds number. As we can see from the numerical values of the heat transfer entropy generation for different Re , we notice that the entropy generation has higher values for higher Reynolds number because of higher temperature gradients at higher velocity, that is, more heat transfer as the Reynolds number is increased for a given Ec_m .

Figure 6.10 presents the heat transfer entropy generation over the sphere surface for different radial locations and for given Reynolds and Eckert number. It can be seen that the entropy generation due to heat transfer increases from a minimum value at the

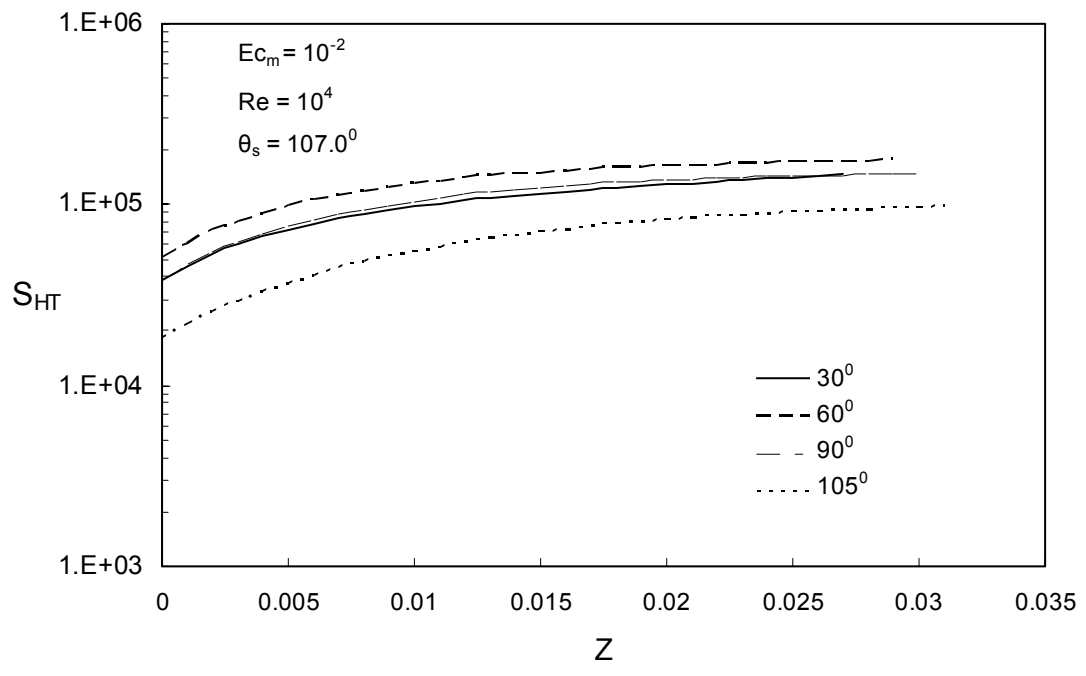


Fig 6-8: Variation of heat transfer entropy generation with radial distance for different meridional stations

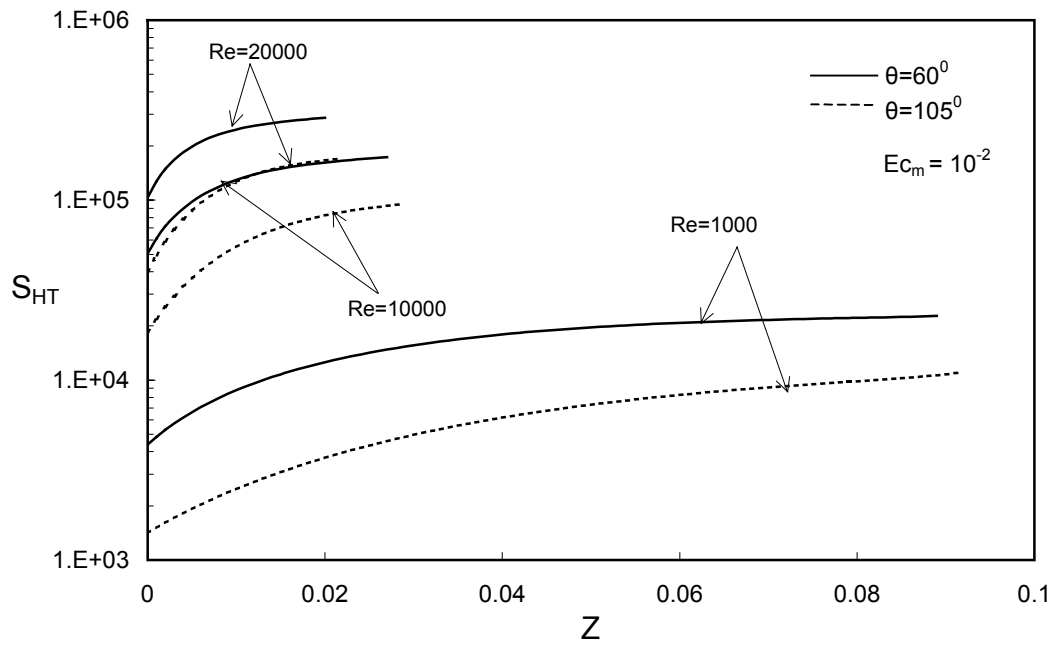


Fig 6-9: Variation of heat transfer entropy generation with radial distance for different Reynolds number at a given Eckert number

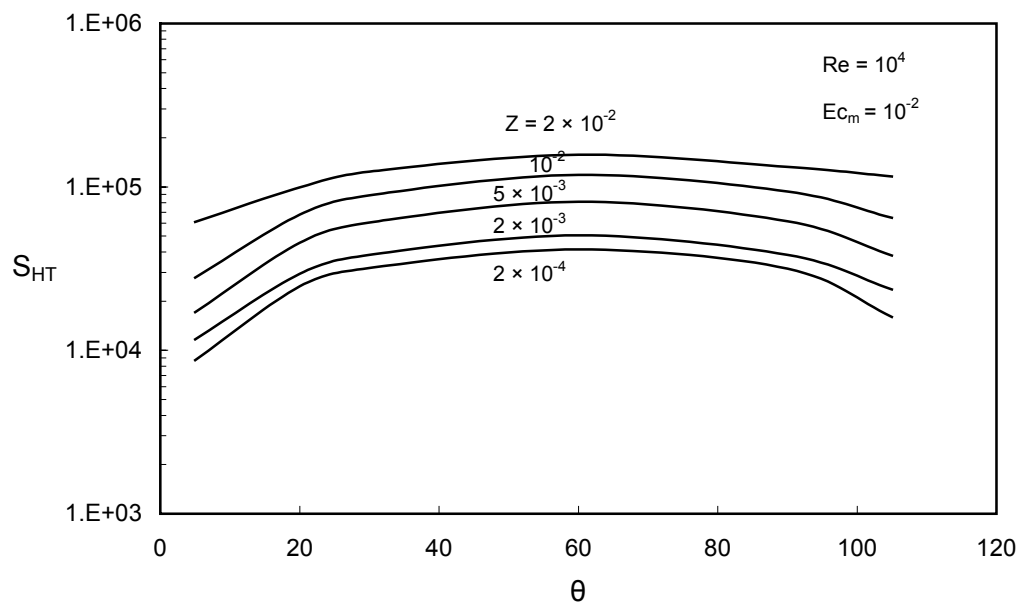


Fig 6-10: Variation of heat transfer entropy generation over the surface of the sphere at different radial locations

front stagnation point till it reaches maximum and then decreases near the separation point. As it approaches the separation point the meridional temperature gradient decreases and hence giving less heat transfer and less entropy generation.

Figure 6.11 gives the variation of fluid friction entropy generation with the radial distance (Z) at some selected angles for given Reynolds and Eckert numbers. This figure shows that entropy generation due to fluid friction is less in magnitude at smaller angles and increases with the angle and then again decreases near the separation angle. As the velocity away from the sphere is higher, resulting in an increase in the fluid friction entropy generation. This can be attributed to the higher kinetic energy of the fluid particles away from the sphere surface. Also it can be seen that meridional locations far away from stagnation point has comparatively less fluid friction at the sphere surface.

Figure 6.12 depicts the effect of Reynolds number on the fluid friction entropy generation at a given meridional location. Higher Reynolds number indicates higher velocity gradients and kinetic energies which result in higher fluid friction and hence higher entropy generation.

Figure 6.13 presents the change of fluid friction entropy generation with Eckert number for two meridional locations along radial direction for a given Reynolds number. As the Eckert number is decreased, fluid friction entropy generation decreases exponentially, this is obvious from the entropy equation (3.20) as Eckert number term is multiplied to the fluid friction term.

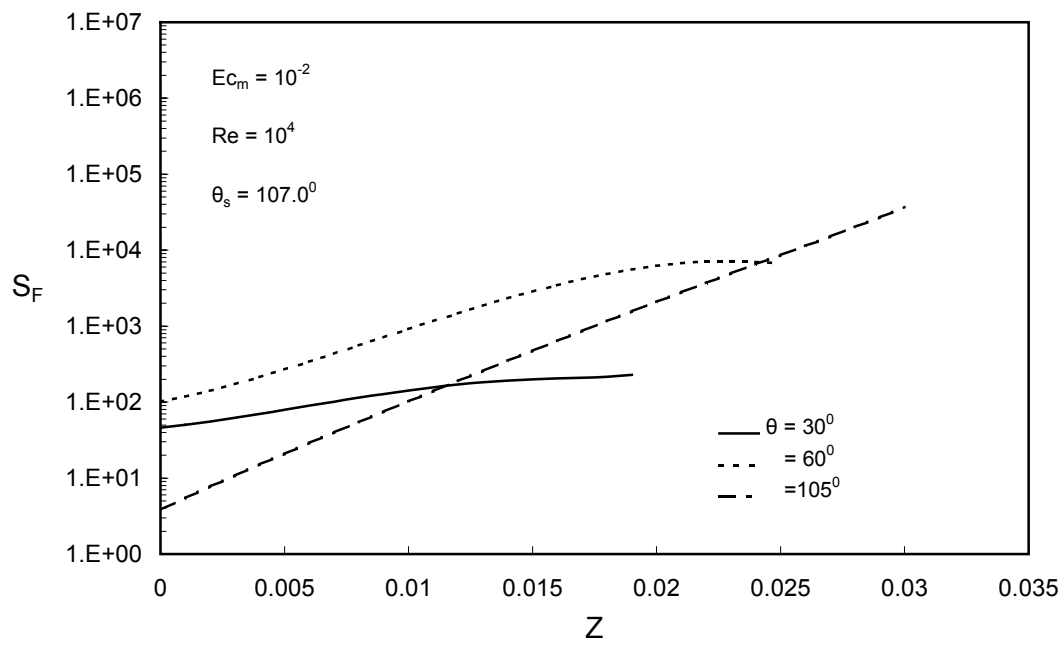


Fig 6-11: Variation of fluid friction entropy generation with radial distance for different meridional stations

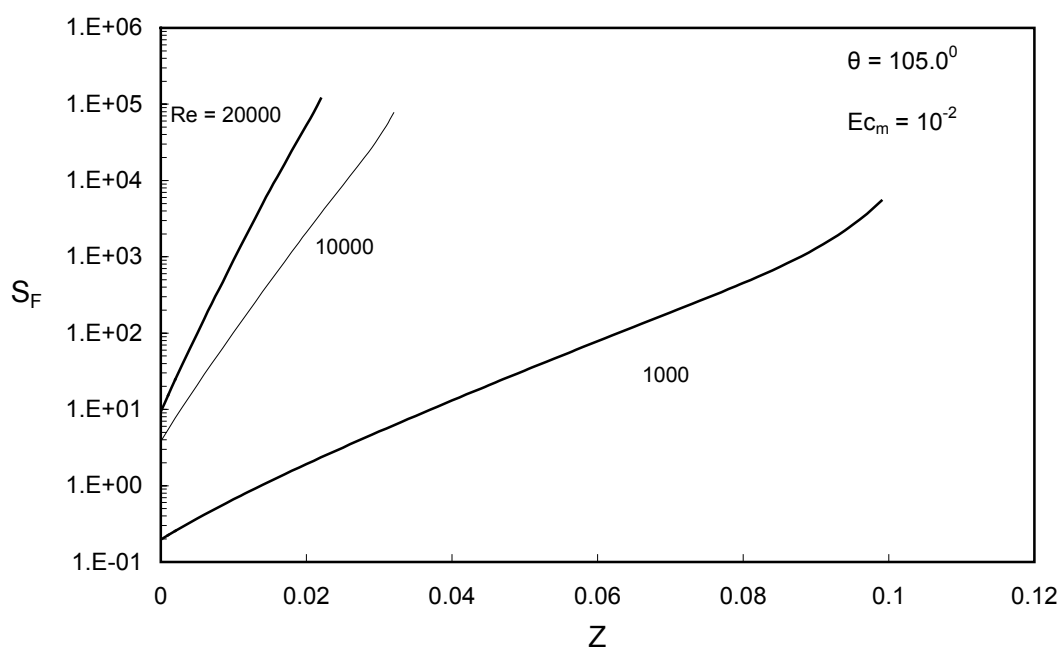


Fig 6-12: Variation of fluid friction entropy generation with radial distance for different Reynolds number at a given meridional location

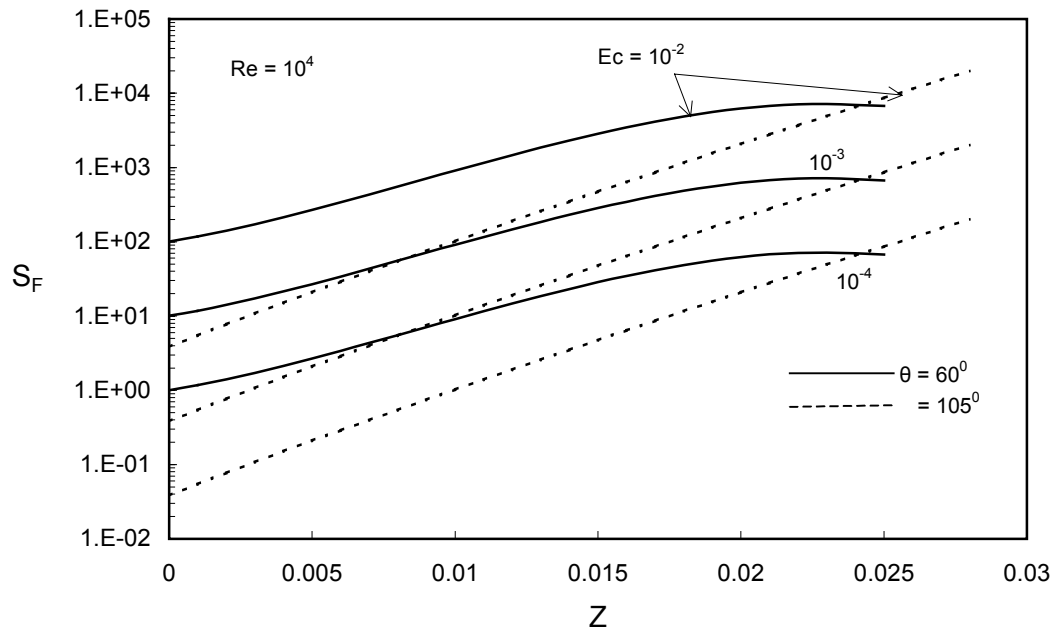


Fig 6-13: Variation of fluid friction entropy generation with radial distance for different Eckert number and meridional locations for a given Reynolds number

Fig 6.14 shows the variation of dimensionless total entropy generation for different Reynolds number (1000, 5000 and 10000) at two different meridional stations. The boundary layer thickness for higher Re is smaller resulting in higher values of velocity and temperature gradients that increase total entropy generation as compared with low Reynolds number. Also at the surface of the sphere due to high temperature and velocity gradients, the entropy generation rate is high and as we move further away from the surface, the gradients decrease and entropy generation rate decreases.

Figure 6.15 shows the variation of entropy generation over the sphere (from front stagnation point until separation angle) at different radial (Z) locations for a given Reynolds number, $Re = 10^4$. Similar to heat transfer entropy generation profile over the sphere, the total entropy generation is showing the same behavior, that is, increases as we move from the front stagnation point and again decreases near the separation point. This similarity of total entropy generation profile to heat transfer part is because the fluid friction entropy generation is significant only in high speed or super sonic flows and compressible flows. In most of the convective processes where heat transfer is the main phenomenon, fluid friction or viscous entropy generation is of less importance, this can be seen clearly from Figure 6.16 in which the fluid friction part is having magnitude of 10^2 less compared to heat transfer part.

Variation of entropy generation with Eckert number is presented in Figure 6.17 for two different Reynolds numbers ($Re = 2 \times 10^4, 10^4$). It can be seen that for $Ec_m < 10^{-3}$,

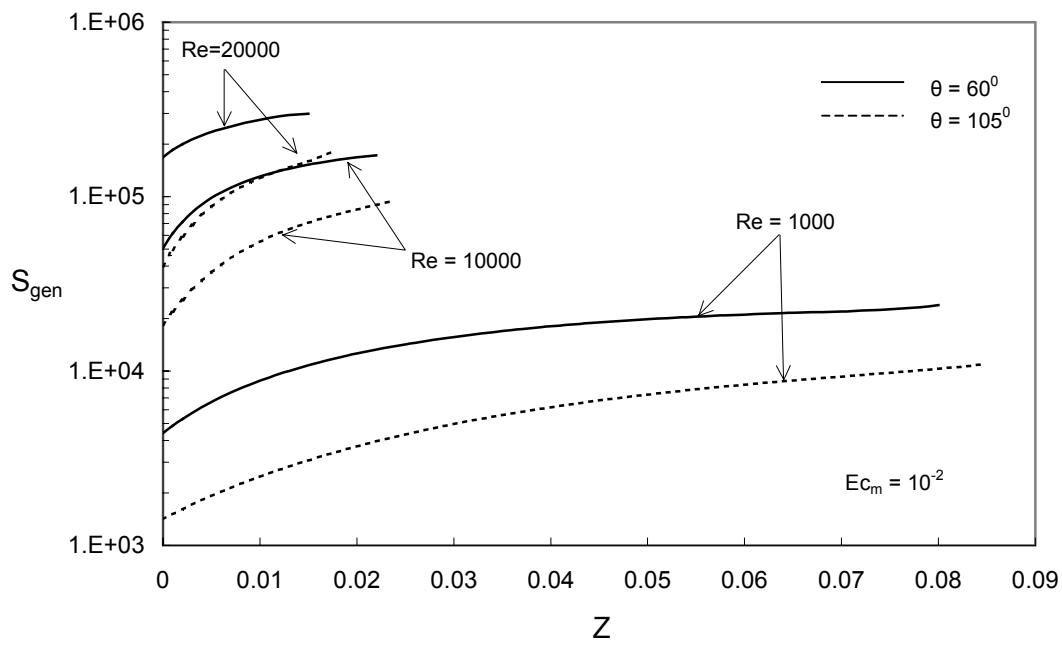


Fig 6-14: Comparing total entropy generation profile along radial direction for different Reynolds number

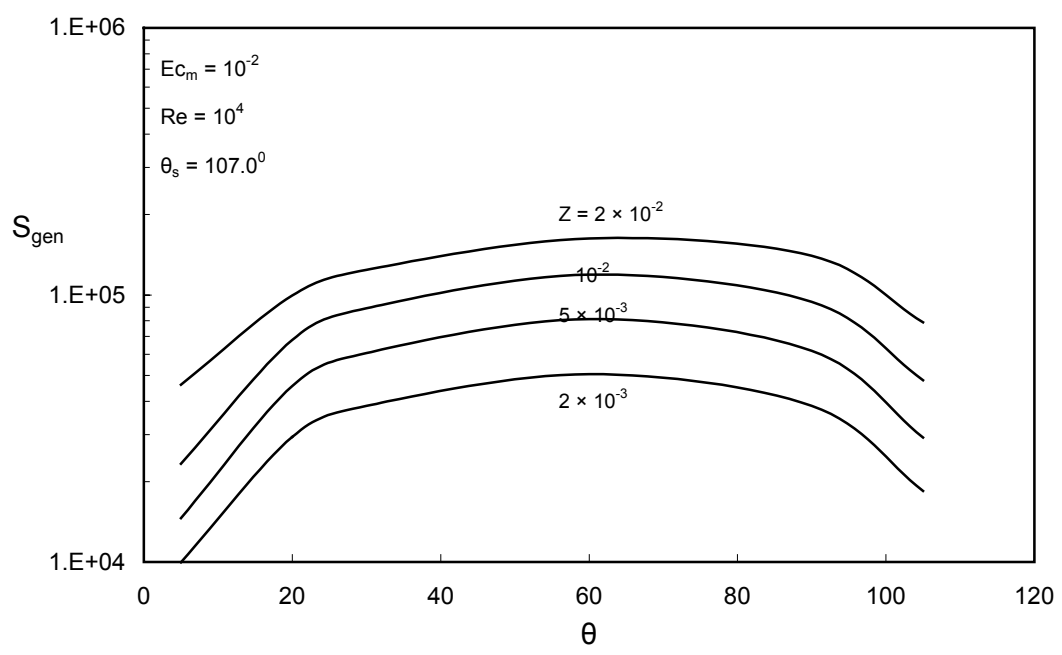


Fig 6-15: Variation of entropy generation over the sphere surface at different radial (Z) locations for a given Reynolds number

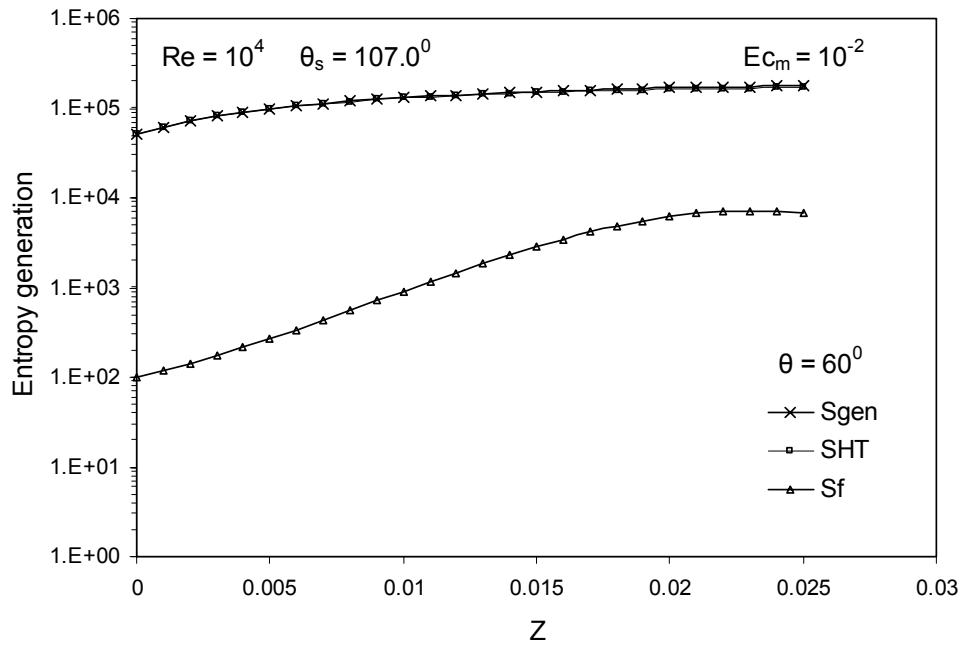


Fig 6-16: Comparing heat transfer, fluid friction and total entropy generation at a particular meridional location

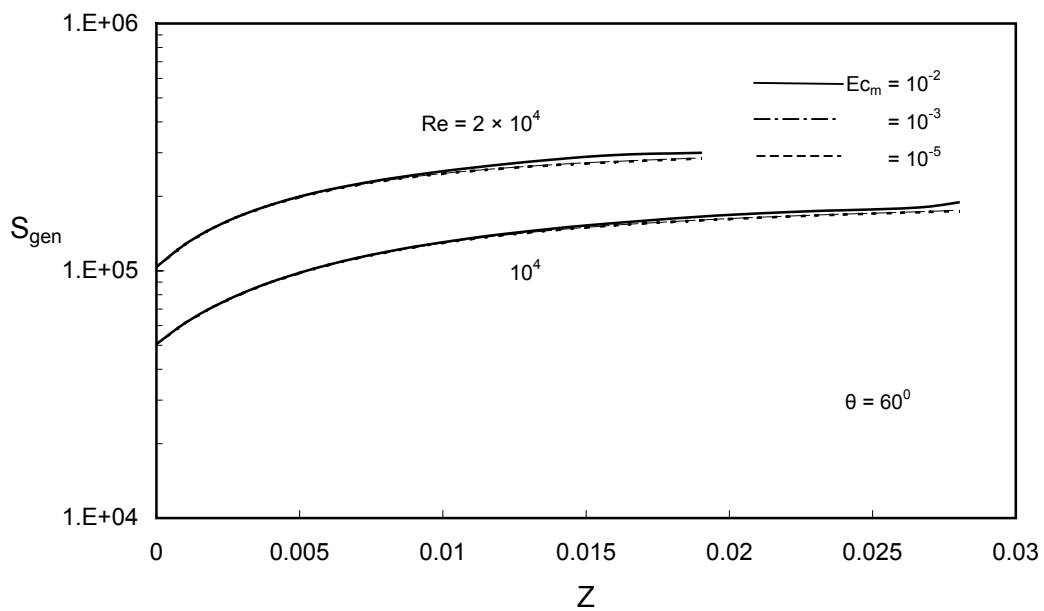


Fig 6-17: Comparing entropy generation profile for different Eckert number

the fluid friction entropy generation is negligible, which result in very less variation in total entropy generation. Hence for flows with very low Reynolds number, which result in low velocities and hence low Eckert number, fluid friction entropy generation can be neglected.

6.3.5 Local and overall average entropy generation profiles:

Local and average entropy generation equations are given in (3.20) and (3.21). It is seen from figure 6.18 that high fluid friction at certain meridional locations ($60^\circ < \theta < 100^\circ$) over the sphere causes the local average fluid friction entropy generation to be remarkable. This is mainly due to fluid particles over the sphere accelerate in the region $0 \leq \theta \leq 90^\circ$ and decelerate in the region where $\theta > 90^\circ$, hence the pressure decreases in the accelerated region and then increases in the decelerated region. Since the external pressure is imposed at the boundary layer, the transformation of the pressure into kinetic energy takes place in the accelerated region and a great deal of the kinetic energy of the particles adjacent to the wall is consumed to move against the friction forces. This can also be related to the velocity gradients, which are high in accelerating region of flow and less in decelerating region of fluid flow. The heat transfer entropy generation is having a dominant effect in total entropy generation as can be seen from the graph.

Figure 6.19 also shows the same pattern of local average entropy generation over the sphere surface for three different Reynolds numbers. We can notice that at higher Re, entropy generation is higher due to small viscous and thermal boundary layer at higher Reynolds number, which results in higher velocity and temperature gradients and hence high heat transfer rates, but at the expense of high entropy generation.

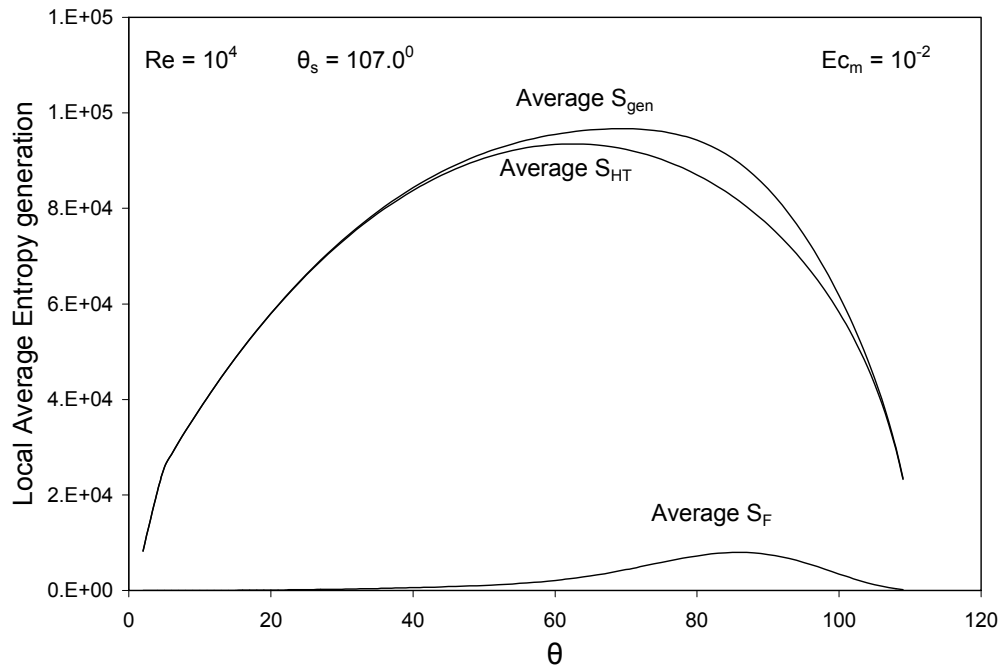


Fig 6-18: Variation of local average entropy generation over the sphere surface for given Reynolds and Eckert numbers

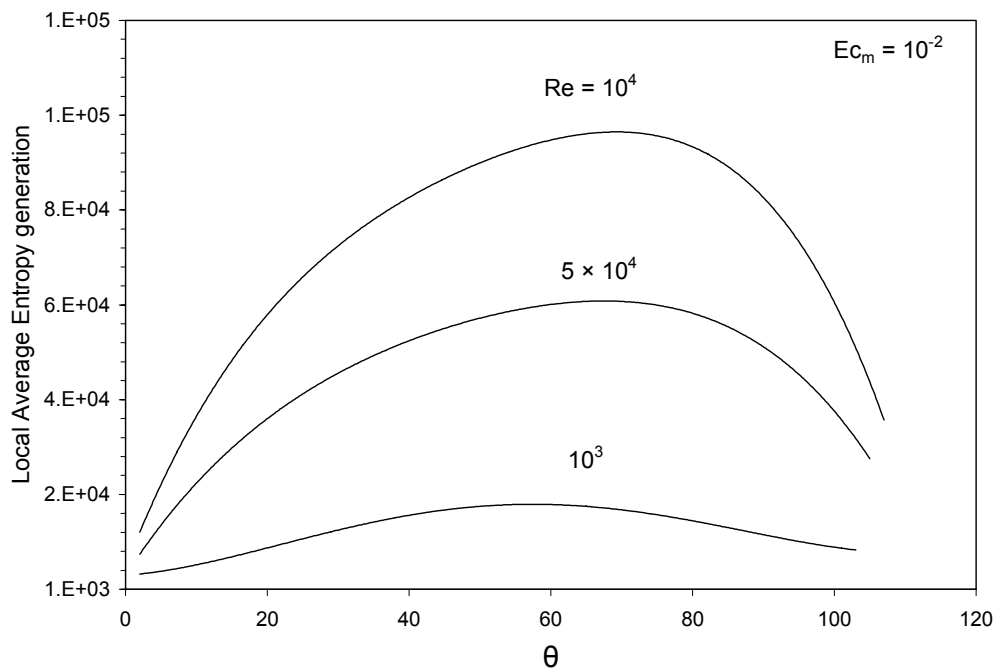


Fig 6-19: Comparing local average entropy generation profiles for different Reynolds numbers

Figure 6.20 shows the variation of average fluid friction entropy generation over the sphere for different Eckert number and a particular Reynolds number ($Re = 10^4$). Again the high velocity gradients at some region in the boundary layer, where acceleration of fluid particles take place, result in high fluid friction and hence increases the average fluid friction entropy generation in these region over the sphere.

Effect of Reynolds number on overall average entropy generation profile is shown in figure 6.21. This figure also presents a comparison between heat transfer, fluid friction and over all entropy generation for a wide range of Reynolds number ($10^2 < Re < 10^5$). This wide range is shown in order to compare with the results presented in the literature ([33] through [37]). As expected from the literature survey, the average entropy generation is decreasing from $Re = 100$ to $Re = 1000$, which is the range of Re reported in the literature. But the range of Reynolds number greater than 1000 has not been presented in the previous studies. We see that as the Reynolds number is increased further $Re = 1000$, S_{avg} shows a constant line and then increases at higher rate for $Re > 10^4$. Hence high Reynolds number results in high heat transfer rates which is the desired phenomena in thermal systems like heat exchangers but at the loss of some useful power in form of entropy generation.

Figure 6.22 shows the effect of Reynolds number on average entropy generation profile for different Eckert number. We can see that high Eckert number results in

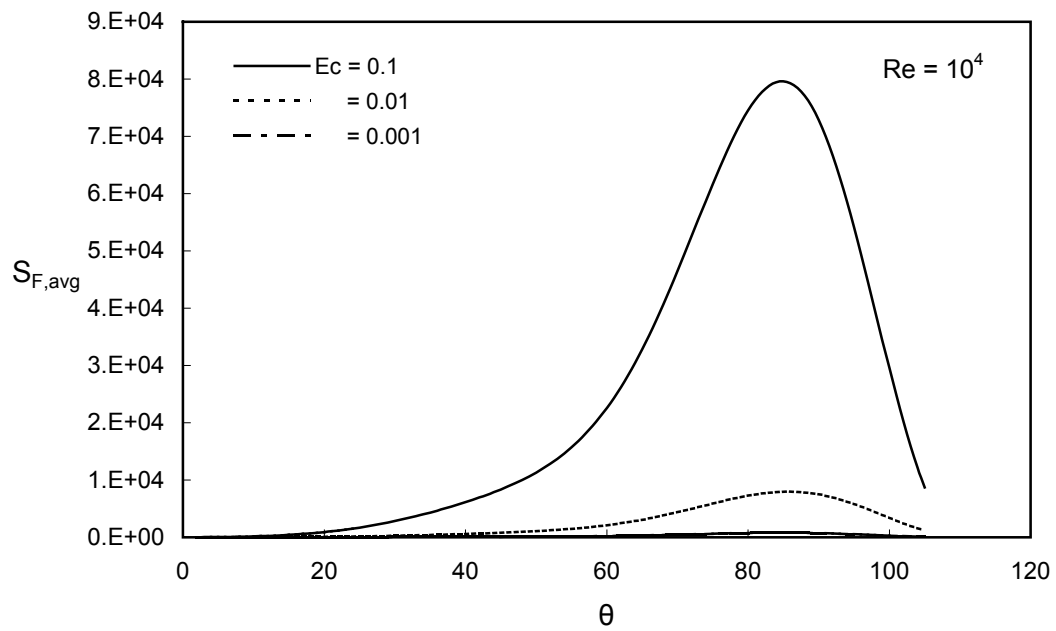


Fig 6-20: Variation of local average fluid friction entropy generation over the sphere for different Eckert numbers and a given Reynolds number

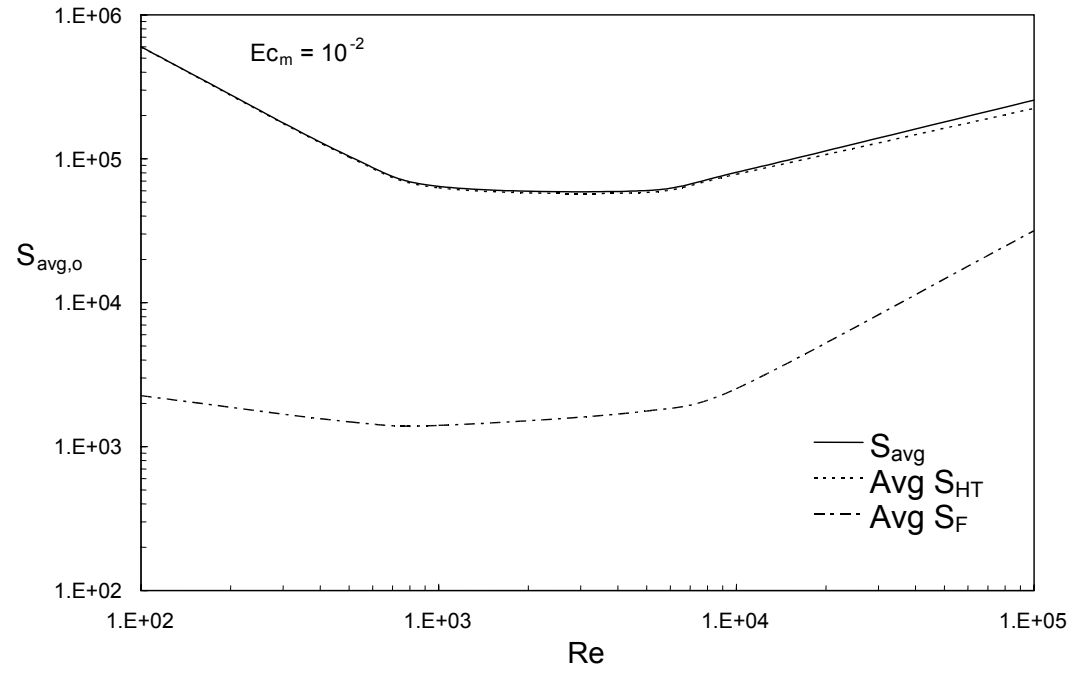


Fig 6-21: Effect of Reynolds number on overall average entropy generation

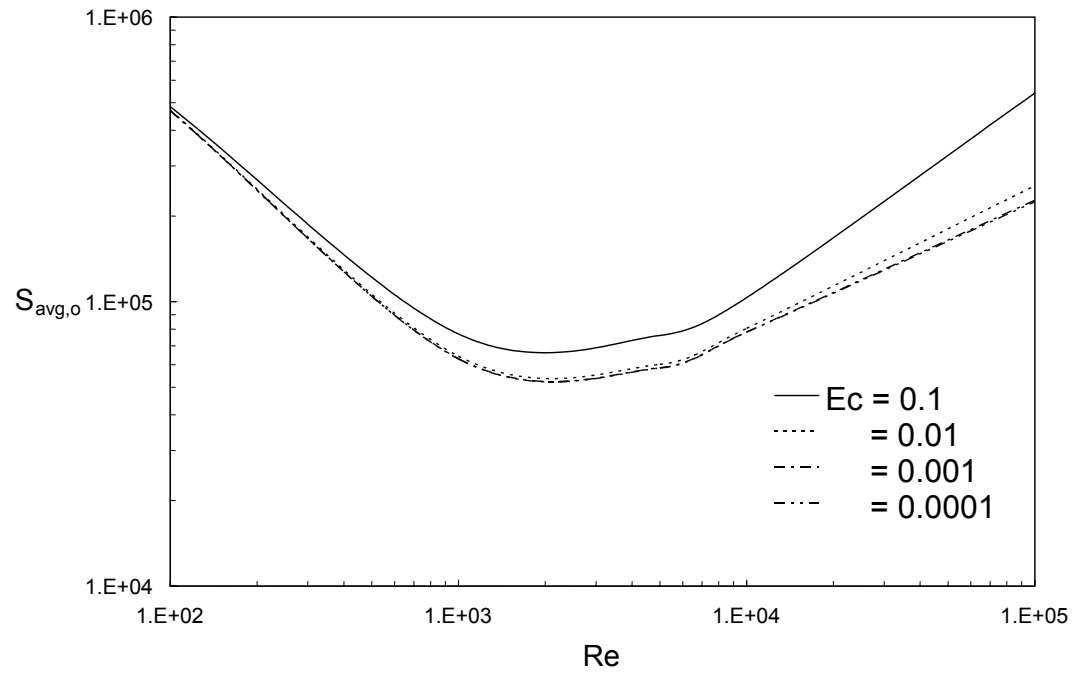


Fig 6-22: Effect of Reynolds number on overall average entropy generation for different Eckert numbers

high $S_{\text{avg},o}$ and as the Eckert number is decreased, the variation of $S_{\text{avg},o}$ is negligible. And hence with this graph we can find the best combination of Reynolds number and Eckert number for which the $S_{\text{avg},o}$ is minimum.

Figure 6.23 presents the effect of Eckert number on the overall average fluid friction entropy generation for different Reynolds numbers. We can notice that the Eckert number plays a considerable role on the magnitude of fluid friction entropy generation and further increase of $Ec_m > 0.1$ causes the flow to be compressible. Figure 6.24 shows the effect of Eckert number on overall average Entropy generation for different Reynolds numbers. As seen from the previous result, fluid friction entropy generation has significant effect on total entropy generation only when Eckert number is considerably high. This figure also shows that for $Ec_m = 0.1$, $S_{\text{avg},o}$ increases steadily and with further increase in Ec_m , $S_{\text{avg},o}$ increasing exponentially, but makes the flow compressible as the mach number is greater than 0.3 for $Ec_m > 0.1$.

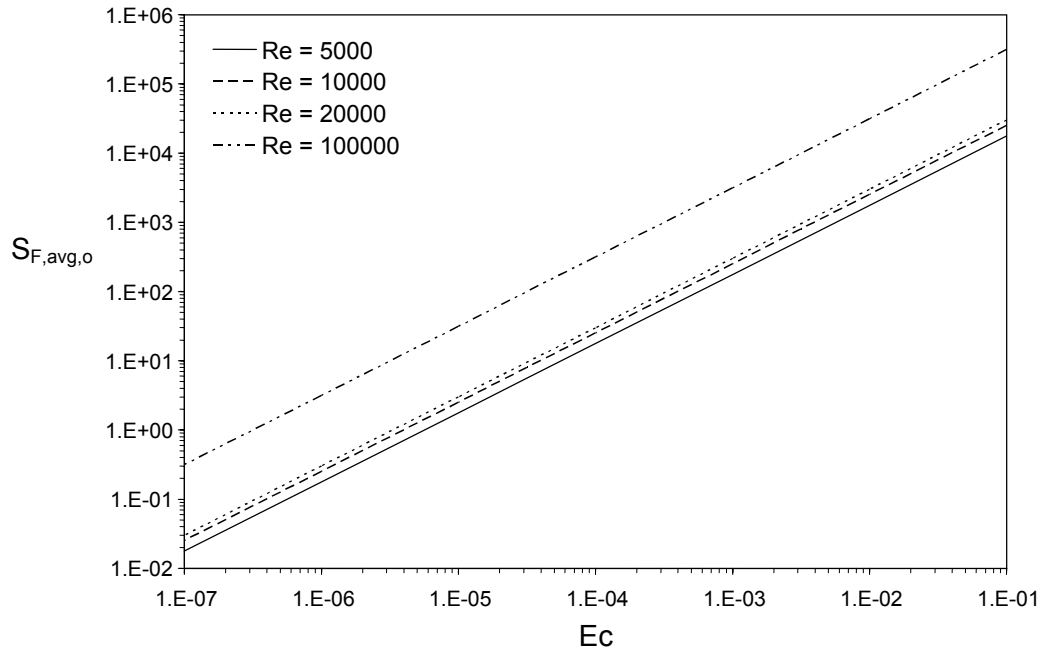


Fig 6-23: Effect of Eckert number on average fluid friction entropy generation for different Reynolds numbers

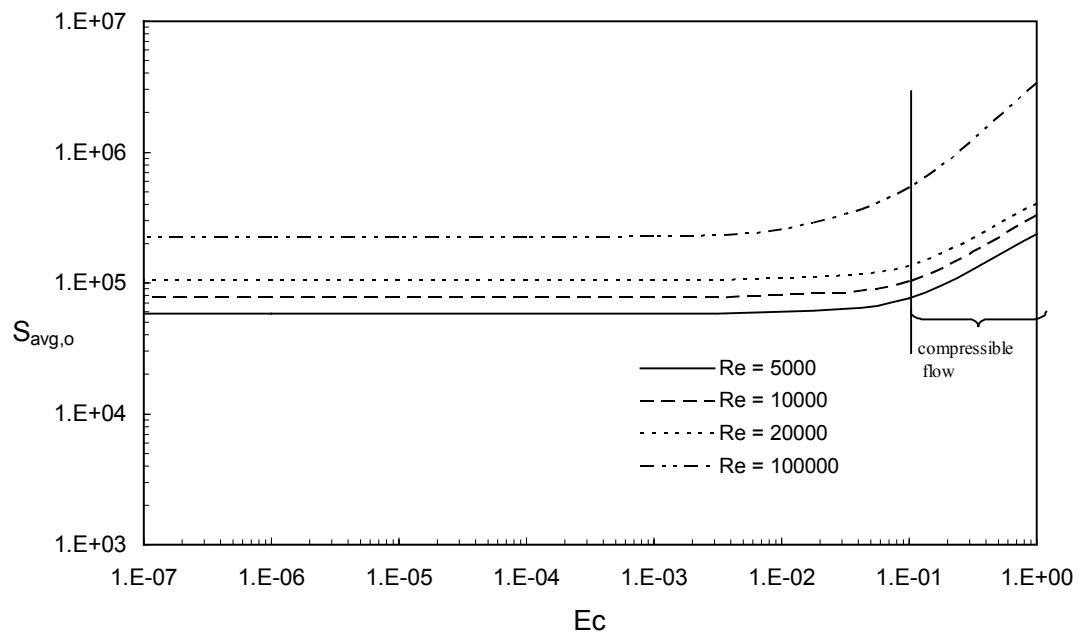


Fig 6-24: Effect of Eckert number on overall average entropy generation for different Reynolds numbers

6.3.6 Bejan number and Irreversibility Ratio:

Paoletti et al.[51] defined Bejan number as the ratio of heat transfer entropy generation to the over all entropy generation, that is

$$Be = \frac{\text{Heat Transfer Entropy Generation}}{\text{Total Entropy Generation}}$$

And its range is $0 \leq Be \leq 1$

$Be \gg \frac{1}{2}$: Irreversibility due to Heat transfer dominates

$Be \ll \frac{1}{2}$: Irreversibility due to Fluid Friction dominates

$Be \cong \frac{1}{2}$: Irreversibility due to Heat transfer equals to Irreversibility due to Fluid Friction

Bejan [45] defined the Irreversibility Distribution Ratio as:

$$IR = \frac{\text{Fluid Friction Entropy Generation}}{\text{Heat Transfer Entropy Generation}}$$

$IR > 1$: Fluid friction entropy generation dominates

$IR < 1$: Heat transfer entropy generation dominates

$IR = 1$: Heat transfer and fluid friction entropy generation are equal

Bejan number and irreversibility ratio are measures of the relative effect of the heat transfer and fluid friction entropy generation on the total entropy generation.

Figure 6.25 shows the effect of Eckert number on the irreversibility ratio. As can be seen from equation (3.20), the Ec_m term is multiplied with the fluid friction term, hence an increase in Eckert number increases fluid friction part and physically it means that as the fluid velocity is increased, the fluid friction increases and hence the entropy generation due to the fluid friction or due to velocity gradients also increase. Figure 6.26 is just a cross plot of Figure 6.25, which shows that the increase in Reynolds number has less effect on the irreversibility ratio when compared with increase in Eckert number.

Figure 6.27 shows the effect of Eckert number on Bejan number for different values of Reynolds number. As can be seen from the graph, Bejan number decreases after certain value of Eckert number which is 10^{-3} , hence the fluid friction has significant effect on the total entropy generation at high Eckert numbers. And for $Ec_m < 10^{-3}$, the Bejan number is constant at a value of one, indicating that the heat transfer entropy generation is the only part contributing to the total entropy generation and fluid friction entropy generation is negligible which is confirming with our discussion in previous results. Figure 6.28 is a cross plot of the results shown in figure 6.27; it confirms that the increase in Reynolds number has little effect on Bejan number at low Ec_m .

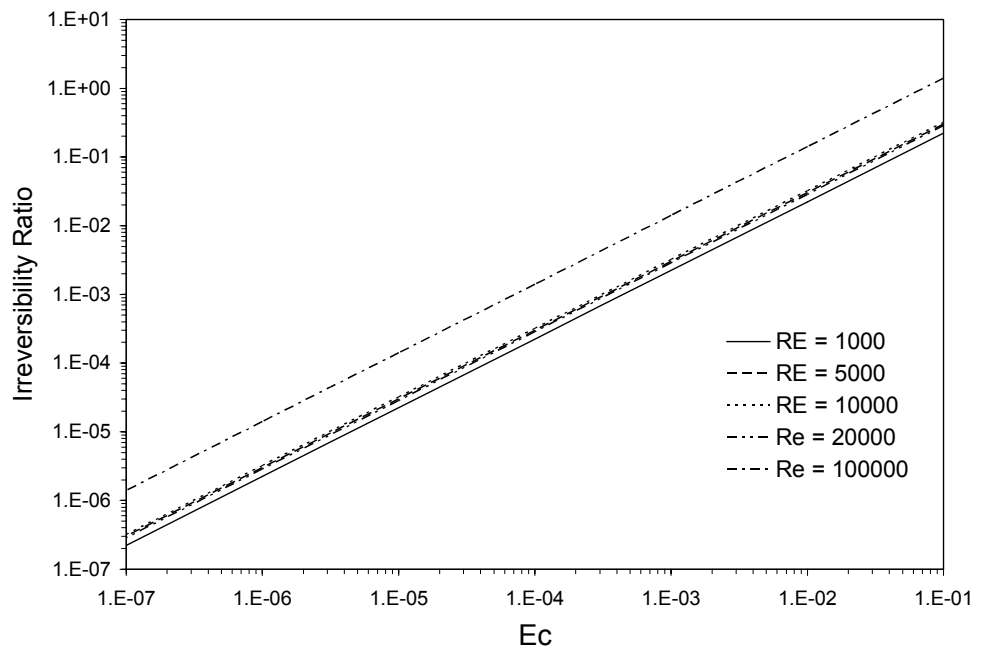


Fig 6-25: Effect of Eckert number on irreversibility ratio for different Reynolds number

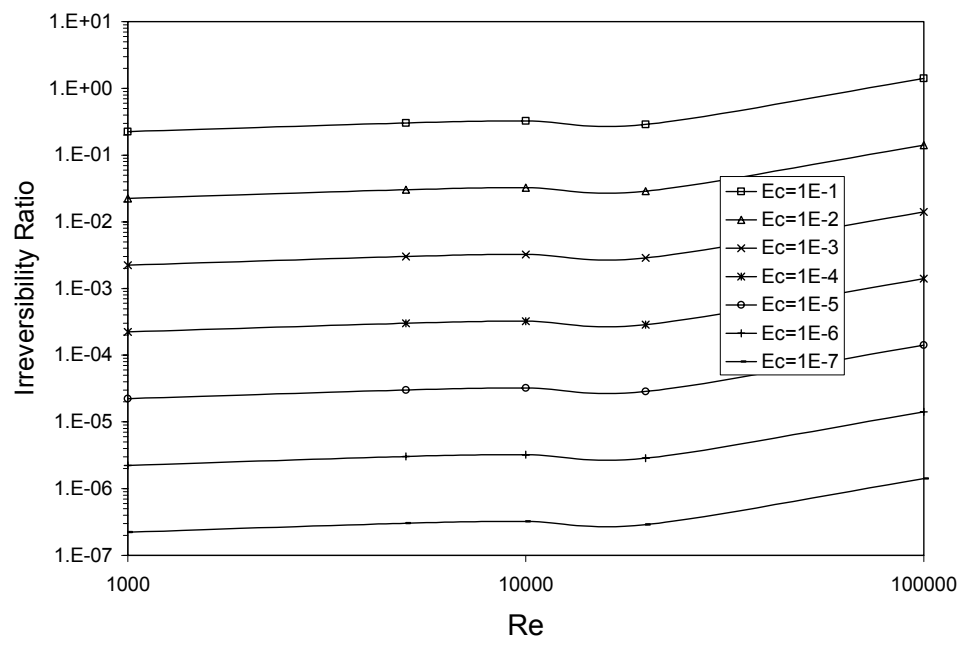


Fig 6-26: Effect of Reynolds number on irreversibility ratio for different Eckert number

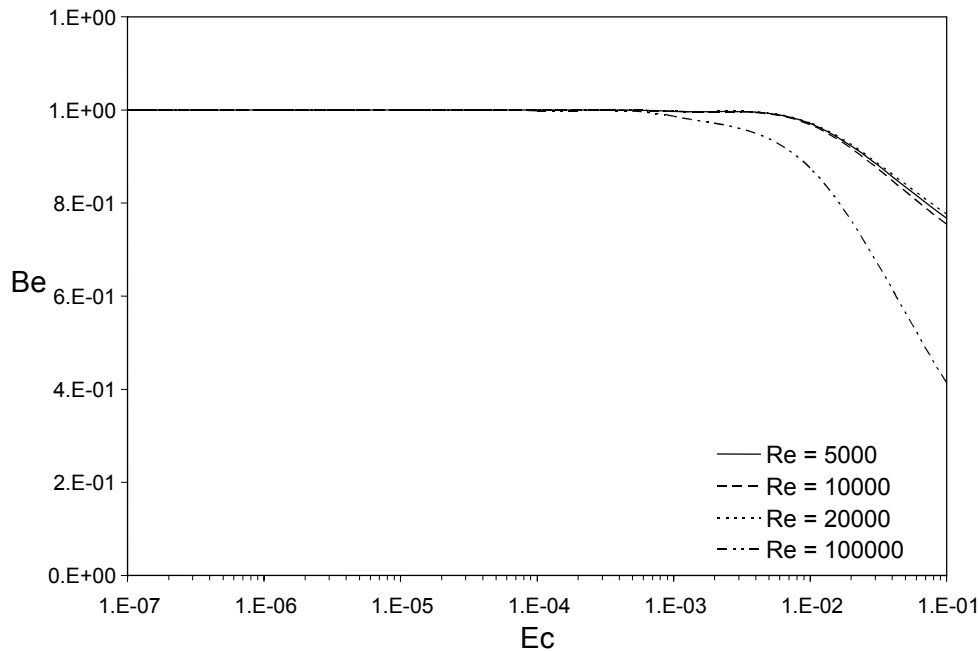


Fig 6.27: Effect of Eckert number on Bejan number for different Reynolds numbers

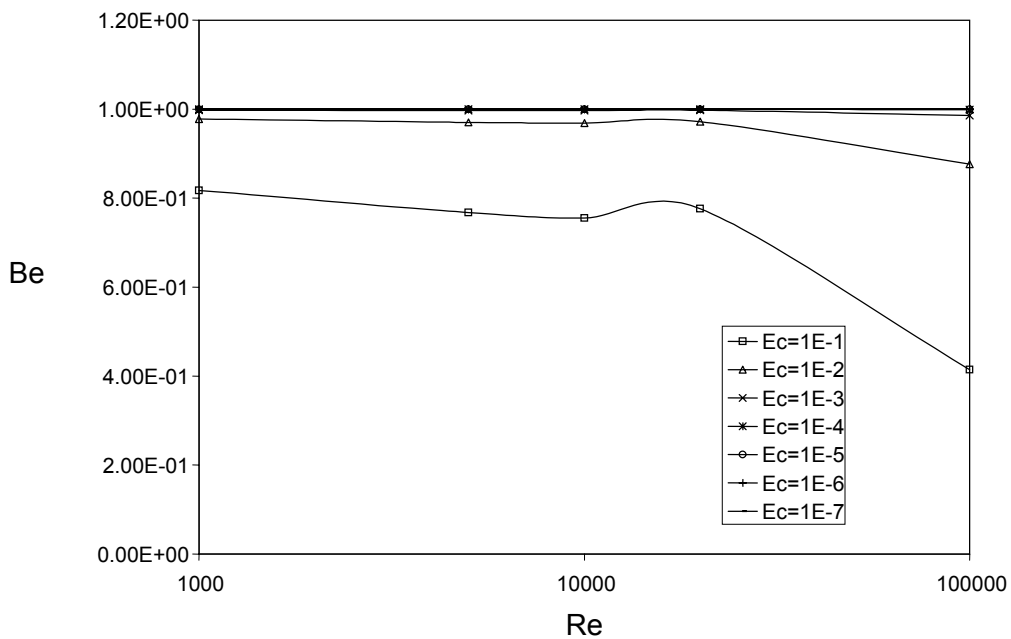


Fig 6-28: Effect of Reynolds number on Bejan number for different Eckert numbers

6.4: Results for uniform heat flux (Forced convection case):

6.4.1 Meridional and radial velocity profiles:

Figure 6.29 shows examples of the meridional velocity profiles at four selected meridional locations ($\theta = 30^\circ, 60^\circ, 90^\circ, 105^\circ$) along the radial distance (Z). It starts with zero value at the surface of the sphere ($Z=0$) representing the no slip condition till it matches the free stream velocity at the edge of the boundary layer surrounding the sphere. This figure shows the increase in the boundary layer thickness as the fluid moves over the sphere surface in the meridional direction illustrating the boundary layer development.

Figure 6.30 shows the developing radial velocity component, W , corresponding to different meridional stations (angles), $\theta = 30^\circ, 60^\circ, 90^\circ, 105^\circ$ for a given Reynolds number ($Re = 10^4$). Similar to the case for uniform wall temperature, these profiles are also starting with zero value at the surface of the sphere (representing no fluid is crossing the boundaries, i.e. no suction or blowing). Profiles are negative for meridional angles $< 90^\circ$ while they have positive values for $\theta > 90^\circ$. This behavior shows that the radial component of velocity is pushing the boundary layer fluid toward the sphere's surface in

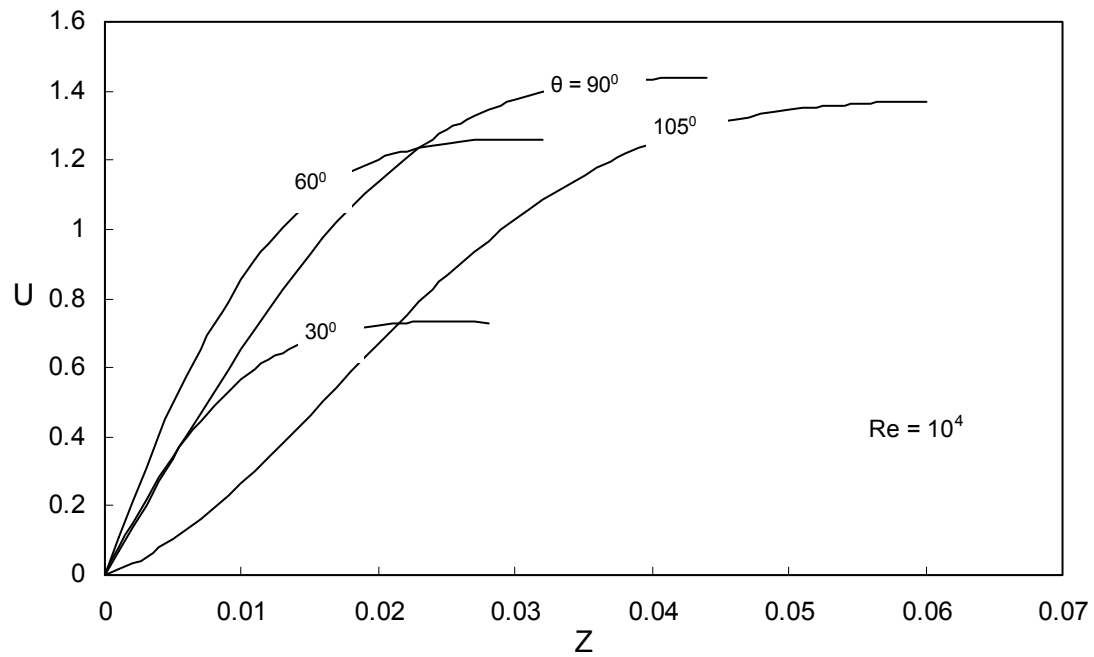


Fig 6.29: Meridional velocity profile at different meridional locations and for a given Reynolds number

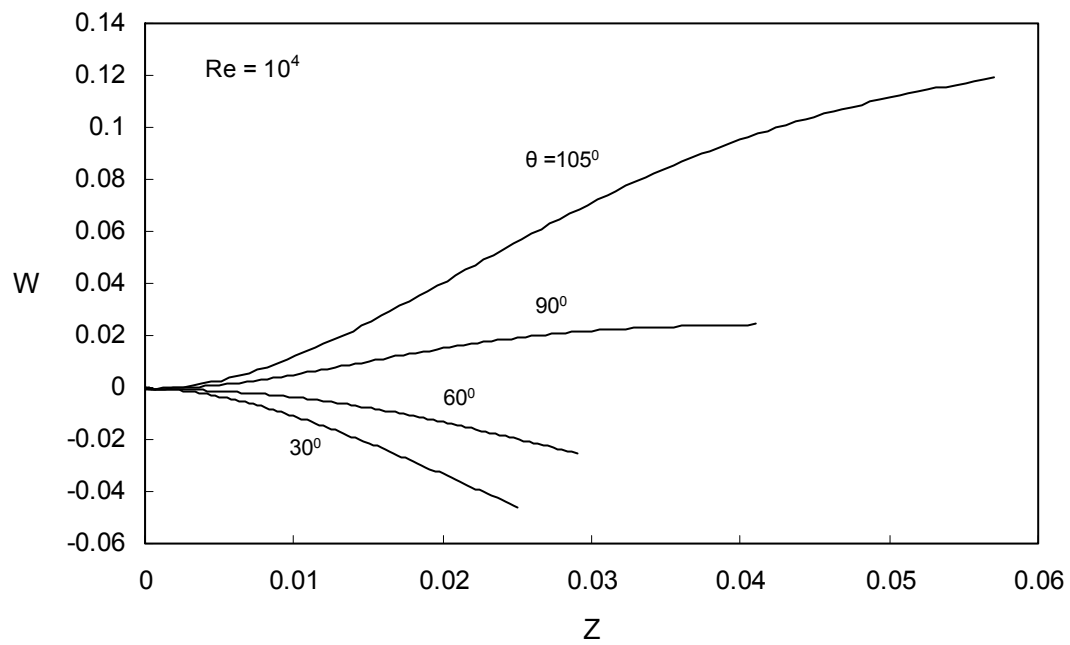


Fig 6.30: Radial velocity profile at different meridional locations

the accelerated region of the flow. On the other hand, in the W-profile in the adverse region ($\theta > 90^\circ$) the tendency changes to blowing of the fluid, the radial component of velocities assist increasing the boundary layer thickness till the maximum thickness is reached at the point where the flow separation takes place.

6.4.2 Temperature Profile:

Figure 6.31 shows the wall temperature profile on the sphere surface for the case of uniform heat flux. As can be seen, the wall temperature is increasing as we move from front stagnation point towards the separation point. Hence as the fluid separates from the sphere at separation point, there is no cooling of the sphere by the free stream due to which the wall temperature attains a highest value.

Figure 6.32 shows the temperature profile at some selected values of the meridional stations, namely $\theta = 30^\circ, 60^\circ, 90^\circ, 105^\circ$ and for two particular values of Reynolds number ($Re = 10^3$ and 10^4). This figure shows the variation of the temperature profiles as the hydrodynamic boundary layer thickness increases along the surface of the sphere until the maximum boundary layer thickness is encountered near the point of flow separation. The non-dimensional wall temperature of the sphere has the maximum value, and as we move away from the sphere, the fluid temperature decreases and finally attains the free stream temperature.

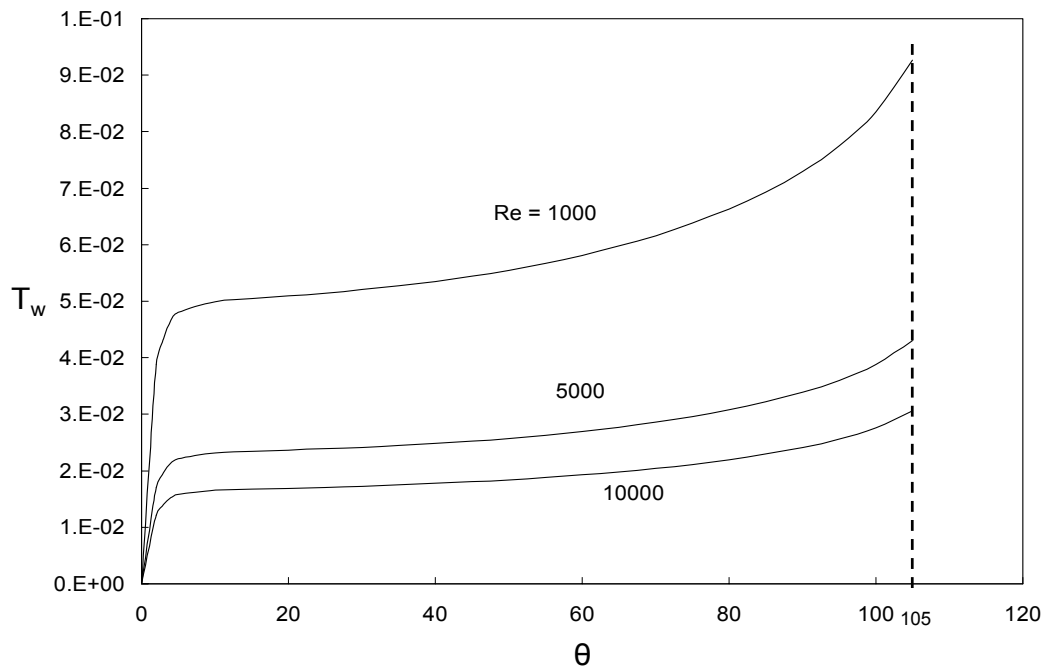


Fig 6-31: Sphere wall temperature profile for different Reynolds numbers

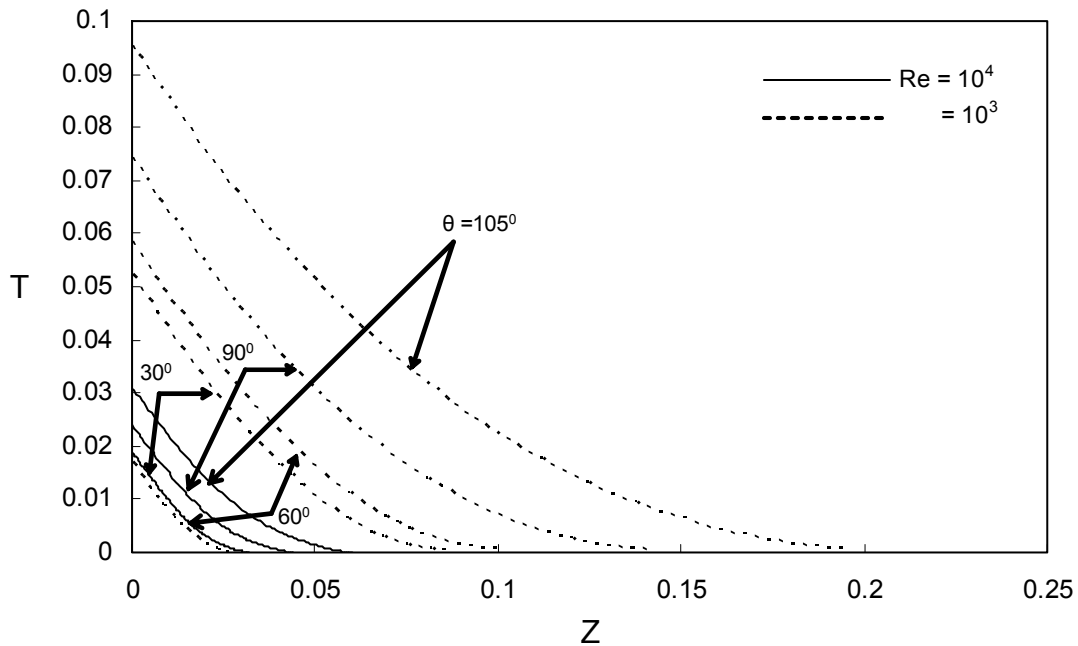


Fig 6-32: Temperature profile at different meridional locations for two different Reynolds numbers

6.4.3 Local entropy generation profiles:

As stated in previous section for uniform wall temperature case, the range of entropy generation number is very large, thus logarithmic scale is used in presenting the results [47].

Figure 6.33 shows the variation of dimensionless heat transfer entropy generation with radial distance for different meridional stations (angles), $\theta = 20^\circ, 30^\circ, 60^\circ, 90^\circ, 105^\circ$, for given Reynolds number ($Re = 10^4$) and modified Eckert number ($Ec_m = 10^{-2}$). This figure shows that as we move away from the surface of the sphere, the entropy generation rate due to heat transfer increases, due to the decrease in temperature gradients near the edge of the boundary layer away from the sphere surface.

Figure 6.34 shows the same variation but for a given value of $\theta = 105^\circ$ at different values of Reynolds number ($Re = 10^3, 5 \times 10^3$ and 10^4). We can see from the numerical values of the heat transfer entropy generation for different Re , the entropy generation has higher values for higher Reynolds number because of higher heat transfer rates at higher velocities, that is, more heat transfer as the Reynolds number is increased for a given Ec_m , which is a desired phenomenon in systems where maximum heat should be removed.

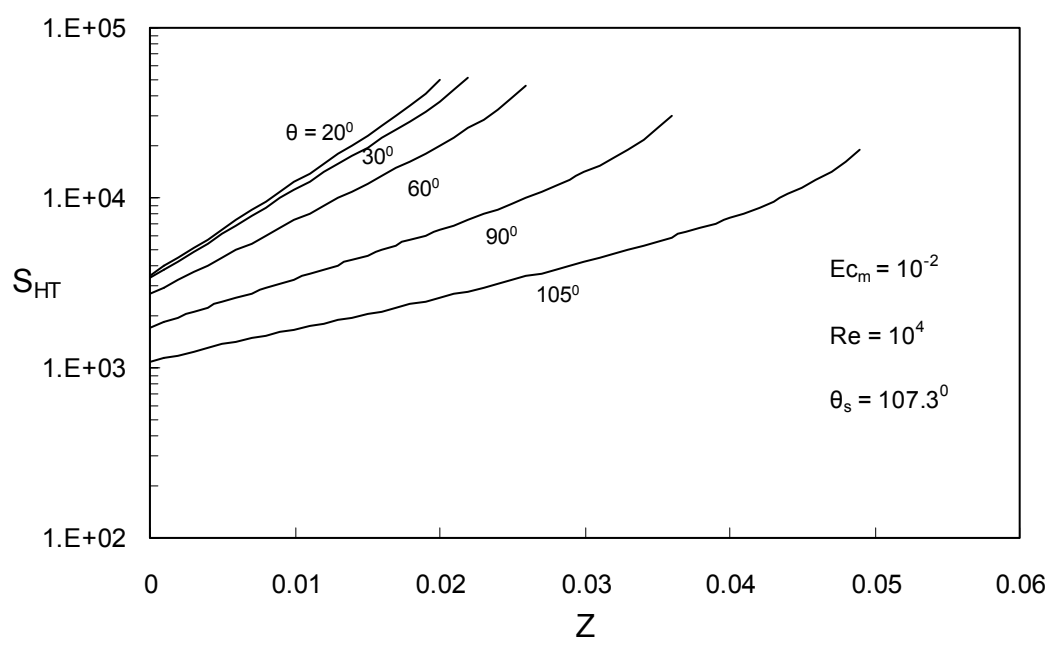


Fig 6-33: Variation of heat transfer entropy generation with radial distance at different meridional stations, UHF case

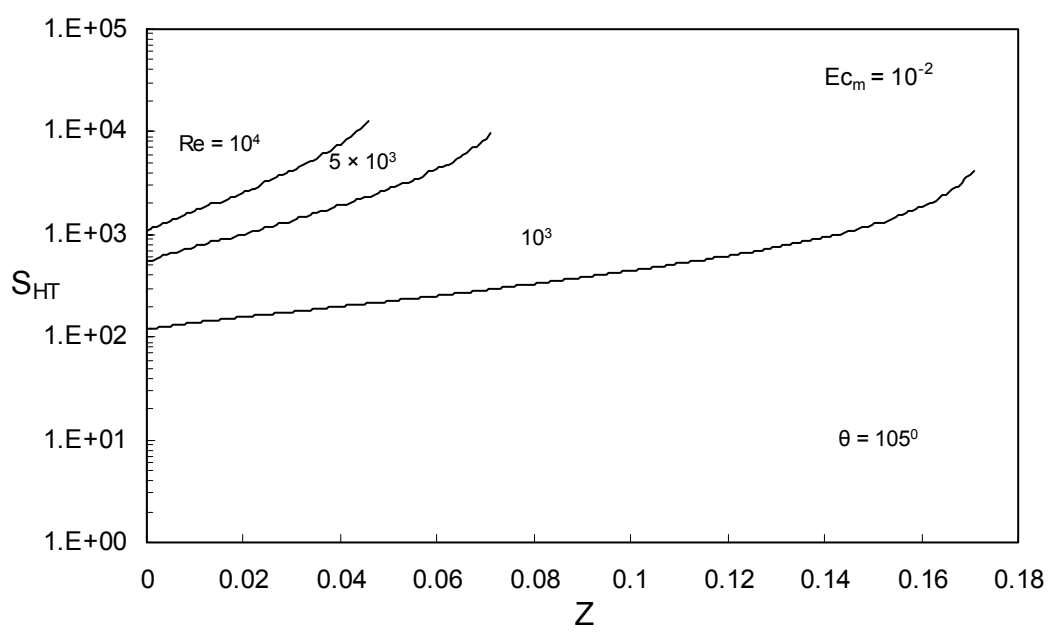


Fig 6-34: Variation of heat transfer entropy generation with radial distance for different Reynolds numbers

Figure 6.35 shows the variation of dimensionless fluid friction entropy generation with the radial distance for different meridional stations, $\theta = 30^\circ, 60^\circ, 90^\circ, 105^\circ$. This figure shows that entropy generation due to fluid friction is less in magnitude at angles near front stagnation point and separation point. As the velocity away from the sphere is higher, but the velocity gradients are decreasing this results in a decrease in the fluid friction entropy generation. This can be attributed to the higher kinetic energy of the fluid particles away from the sphere surface. Also it can be seen that meridional locations far away from stagnation point has comparatively less fluid friction at the sphere surface. If we compare the fluid friction entropy generation due to Uniform wall temperature from figure 6.12 and Uniform Heat flux from figure 6.36, we can see that the magnitude of entropy generation due to fluid friction is very small in UHF case and hence negligible for the range of Reynolds number investigated. In addition, the magnitude of fluid friction entropy generation is of the order of 10^3 less when compared with heat transfer entropy generation; hence fluid friction entropy generation can be neglected in practical analysis for the case of uniform heat flux.

Figures 6.37 and 6.38 represent the variation of total entropy generation at different meridional locations and for different Reynolds numbers, respectively. The entropy generation is increasing linearly along the radial direction till it reaches the edge of the boundary layer, and also we can notice that the smaller angles have higher entropy generation than larger angles because of the smaller thermal boundary layer thickness near the front stagnation point resulting in higher temperature gradients and hence higher

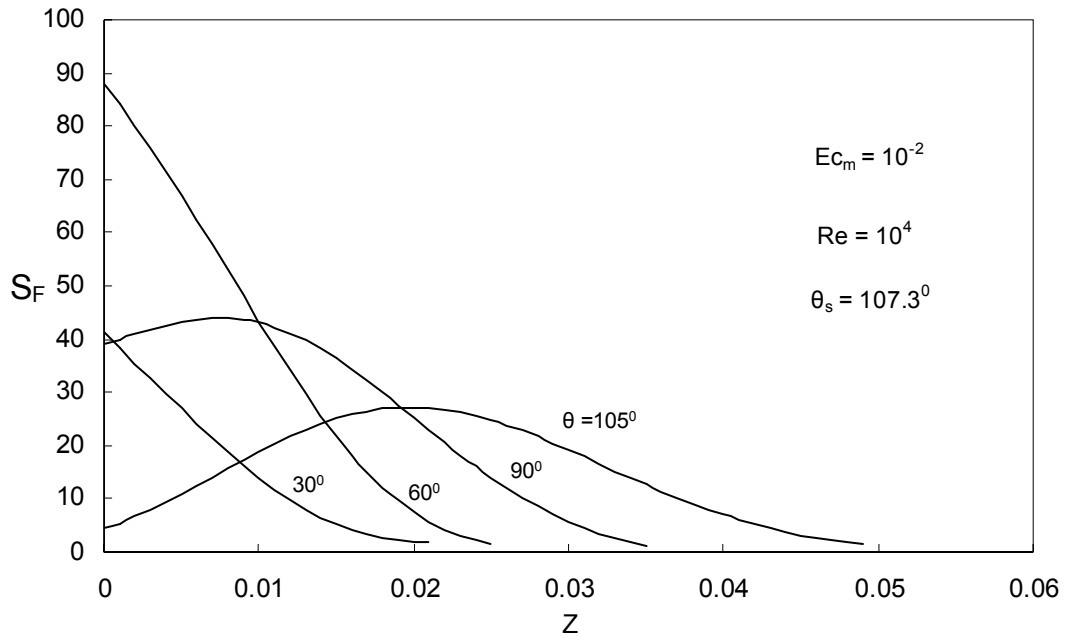


Fig 6-35: Variation of fluid friction entropy generation with the radial distance at different meridional stations

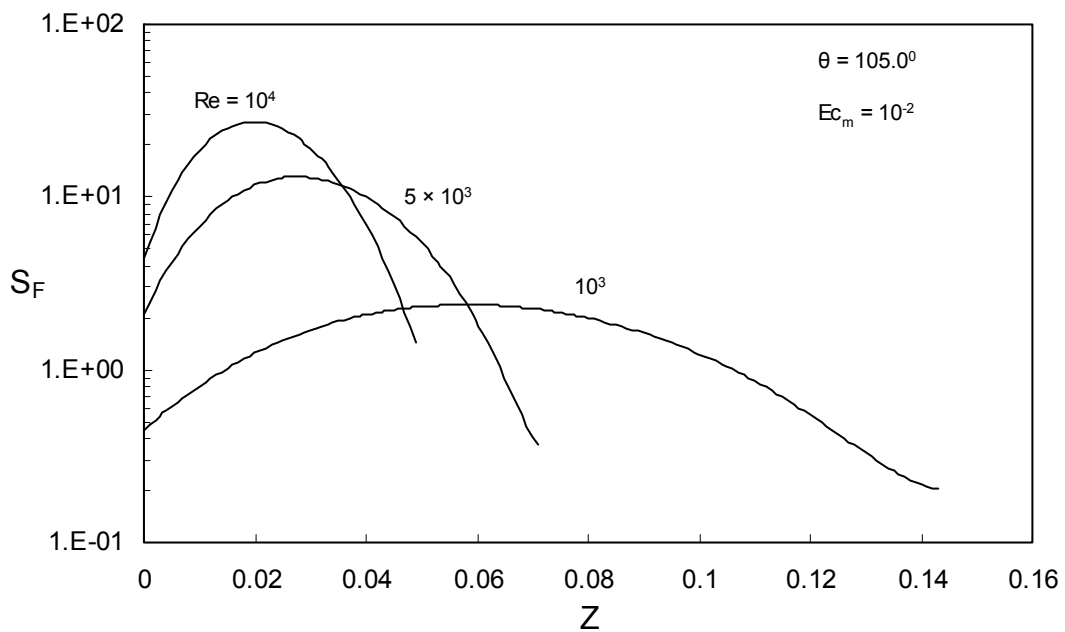


Fig 6-36: Variation of fluid friction entropy generation with the radial distance for different Reynolds numbers and at a given meridional location

thermal entropy generation rates. We can also notice from figure 6.38 that the entropy generation profile has the same trend for all the Reynolds numbers. And higher the Reynolds number, higher is the entropy generation for given Eckert number.

Figure 6.39 shows the variation of dimensionless entropy generation over the sphere surface at different radial (Z) locations for given Reynolds number and Eckert number. It is seen here that the entropy generation is decreasing as we move from front stagnation point to the separation point; this can be understood better if we see the temperature profile, which is increasing constantly. This makes entropy generation profile decreasing as the temperature (T) appears in the denominator of entropy term in equation (3.22).

Figure 6.40 compares heat transfer and total entropy generation at a particular meridional location ($\theta = 60^\circ$) and Eckert number, and for two values of Reynolds number ($Re = 5 \times 10^3$ and 10^4). Since the fluid friction entropy generation is negligibly small as seen from figure 6.36, it has been excluded in this graph. The curves of total and heat transfer entropy generation are overlapping; hence we can say that the major contribution to entropy generation is through heat transfer and the fluid friction is negligible in this case of uniform heat flux.

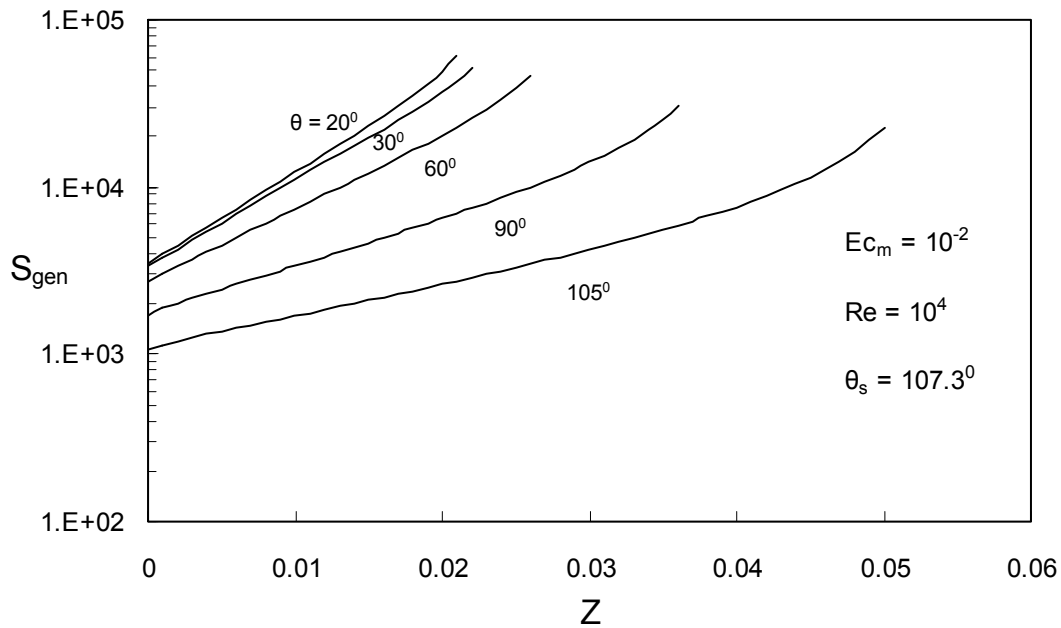


Fig 6-37: Variation of total entropy generation with the radial distance for different meridional locations

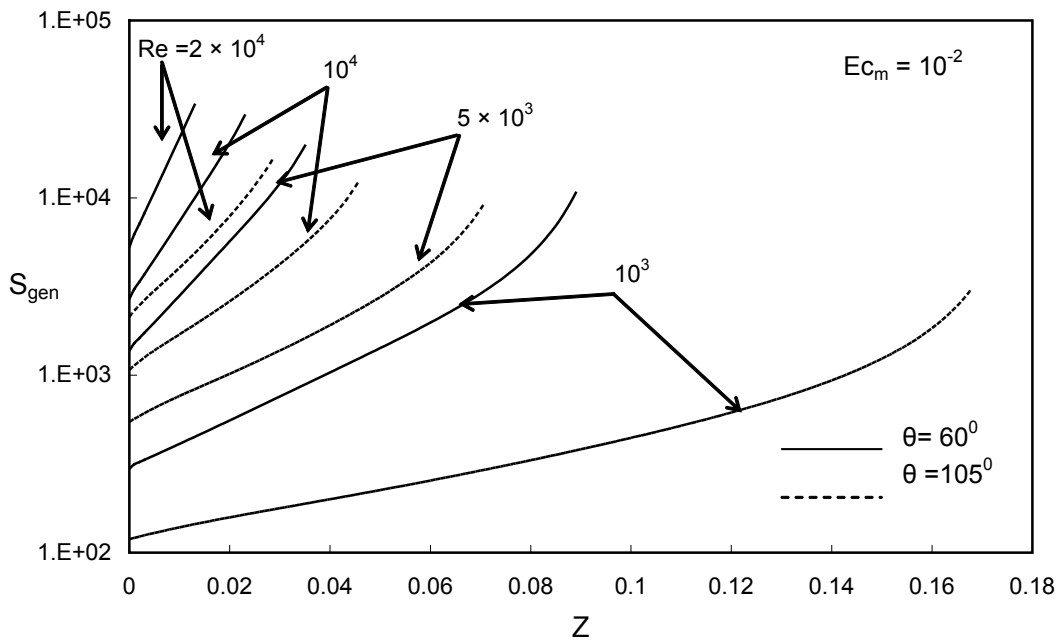


Fig 6-38: Comparing total entropy generation profile for different Reynolds numbers

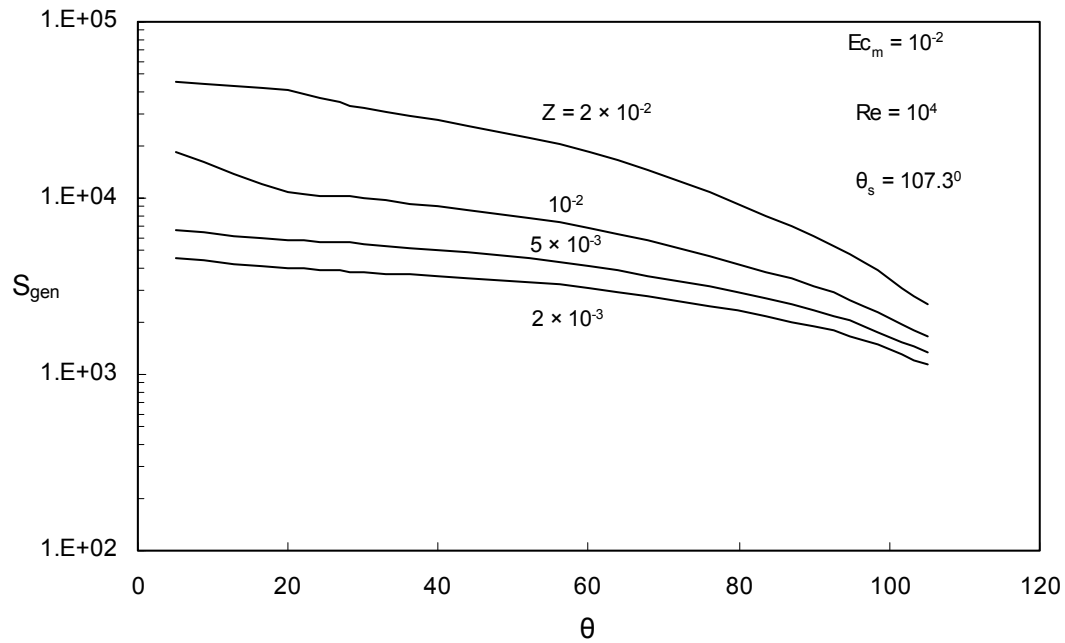


Fig 6-39: Variation of entropy generation over the sphere surface at different radial (Z) locations for a given Reynolds number

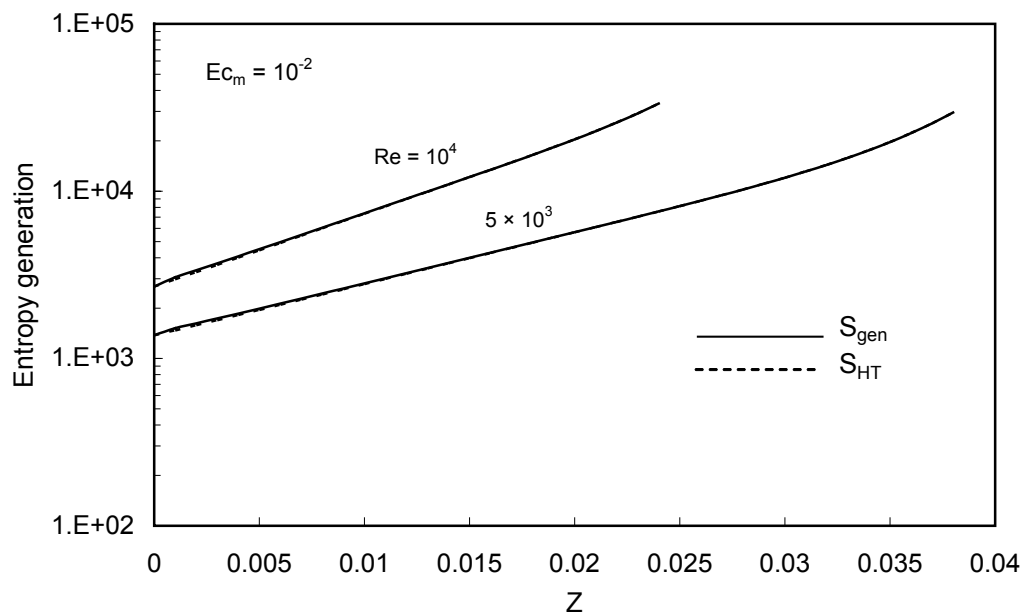


Fig 6-40: Comparing heat transfer and total entropy generation at a particular meridional location and Eckert number

6.4.4 Average entropy generation profiles:

In this section, local and total average entropy generation is presented for different engineering parameters like Reynolds number and Eckert number.

The local average is the average of the values computed along the radial direction (Z) that starts from the sphere surface till the edge of boundary layer. Figure 6.41 shows the variation of local average heat transfer entropy generation for different Reynolds number ($Re = 1000, 5000, 10^4, 10^5$). The same trend is observed for all the Reynolds number values, that is, entropy generation rate is highest near the stagnation point and then it decreases as we move towards the separation point. The same trend is shown also for total entropy generation in figure 6.42 that presents the local average entropy generation profile for different Reynolds number ($Re = 1000, 5000, 10^4, 20000, 10^5$). It can also be seen that higher Reynolds number leads to higher entropy generation for a given Eckert number, due to small viscous and thermal boundary layer thickness at higher Reynolds number, which results in higher velocity and temperature gradients and hence higher heat transfer rates, but at the expense of higher entropy generation.

Figure 6.43 shows the local average entropy generation profile for different Eckert number ($Ec = 10^0, 10^{-1}, 10^{-3}$) for a given Reynolds number ($Re = 10^3$). Although $Ec = 10^0$ represents the compressible flow, as established in table 6.1, this result has been presented to show a general trend for different Eckert numbers. We can notice that change in Eckert number has very little effect on the dimensionless local average entropy generation because the total magnitude of fluid friction entropy generation itself is very small as indicated from earlier results.

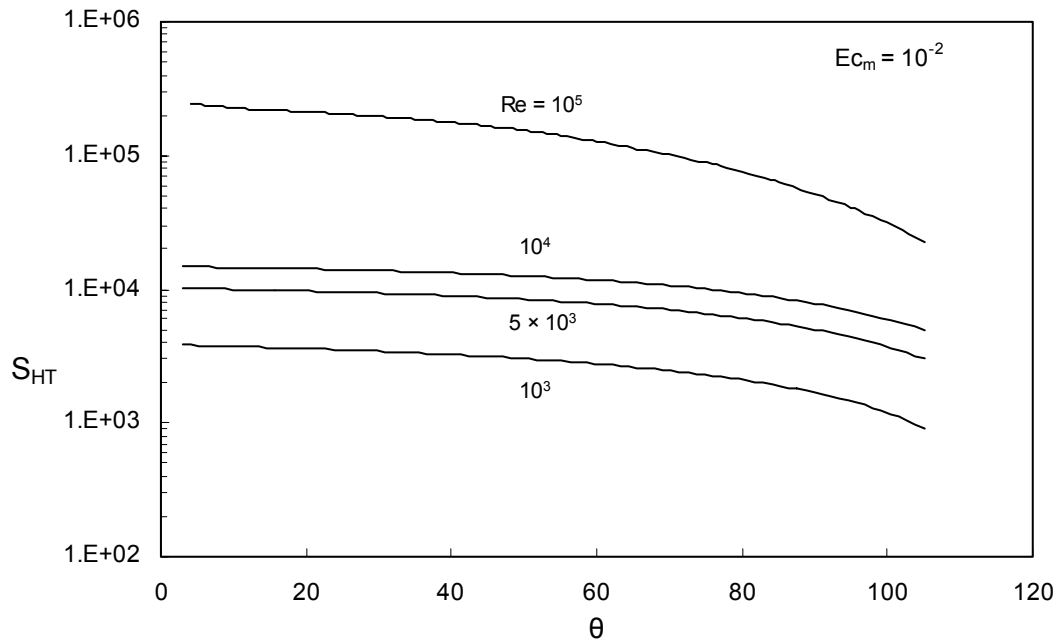


Fig 6-41: Variation of local average heat transfer entropy generation for different Reynolds numbers

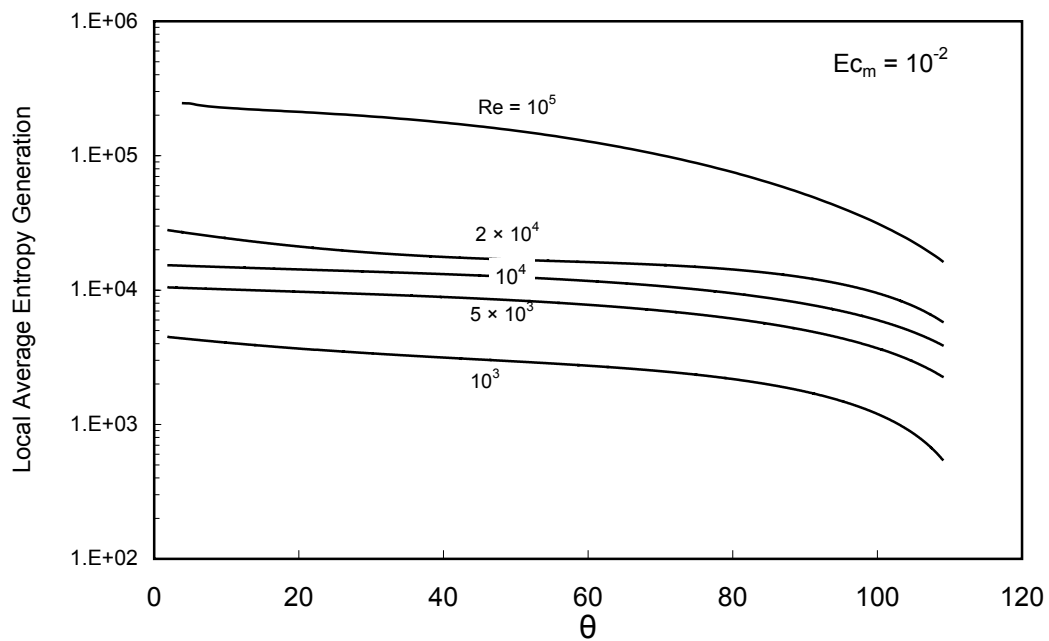


Fig 6-42: Variation of local average entropy generation for different Reynolds number

Figure 6.44 shows the effect of Reynolds number ($10^2 < Re < 10^5$) on average entropy generation profile for different Eckert numbers. As seen in the earlier graph, the effect of Eckert number is very small for any Reynolds number, we notice here that as the Reynolds number is increased, the average entropy generation increases indicating that high Reynolds number result in high heat transfer rates but at the expense of higher losses in terms of entropy generation which in turn result in high irreversibility and power loss in thermal systems. Hence it can be concluded from this graph that in uniform heat flux case, low Reynolds number result in less entropy generation and vice versa.

Figures 6.45 and 6.46 show the effect of Eckert number on average fluid friction and total average entropy generation respectively. We can notice that the Eckert number plays a considerable role on the magnitude of fluid friction entropy generation since an increase in the Eckert number increases the fluid friction entropy generation linearly for any Reynolds number. Further increase of $Ec_m > 0.1$ causes the flow to be compressible. As seen in earlier results presented in figures 6.35 and 6.40, the fluid friction entropy generation has little contribution to the total entropy generation; hence figure 6.46 shows a constant line indicating that the fluid friction term has negligible effect on total entropy generation and hence can be neglected for the cases of uniform heat flux.

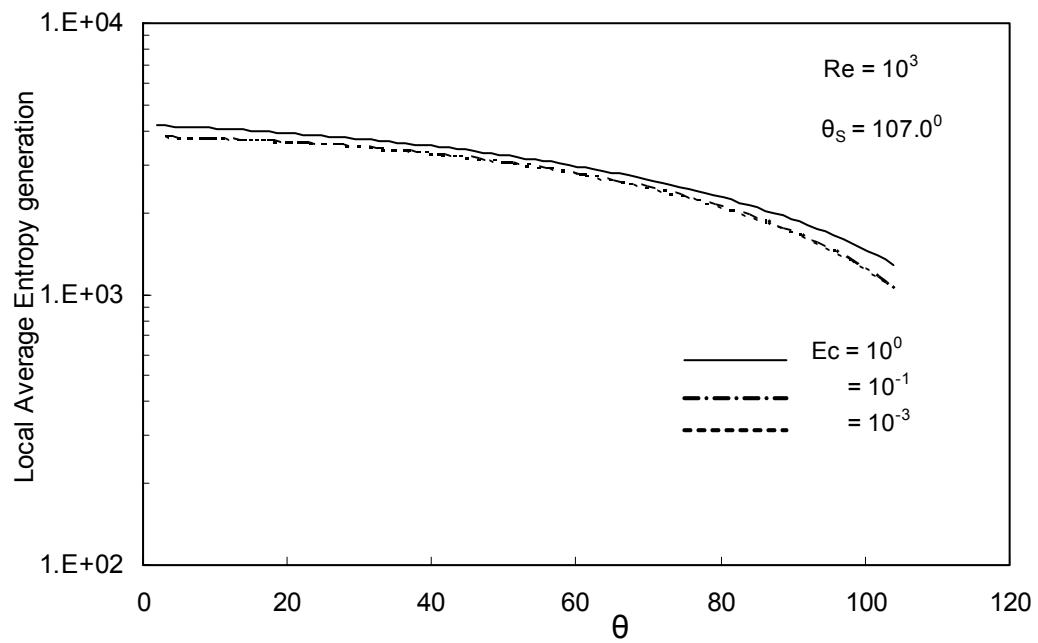


Fig 6-43: Comparing local average entropy generation profile for different Eckert numbers and a given Reynolds number

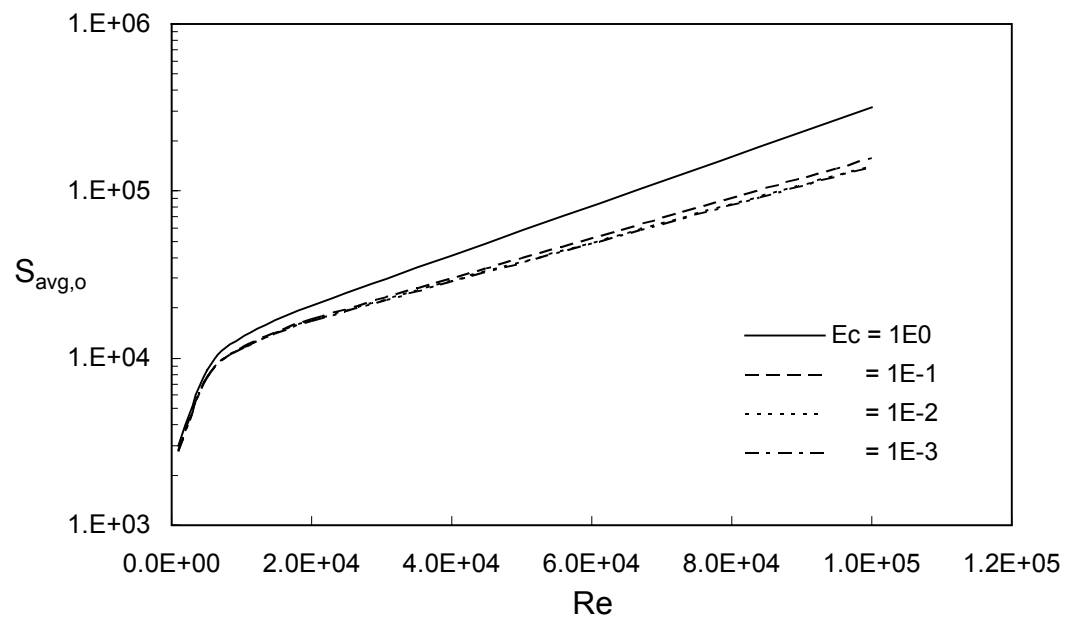


Fig 6-44: Effect of Reynolds number on average entropy generation profile for different Eckert numbers

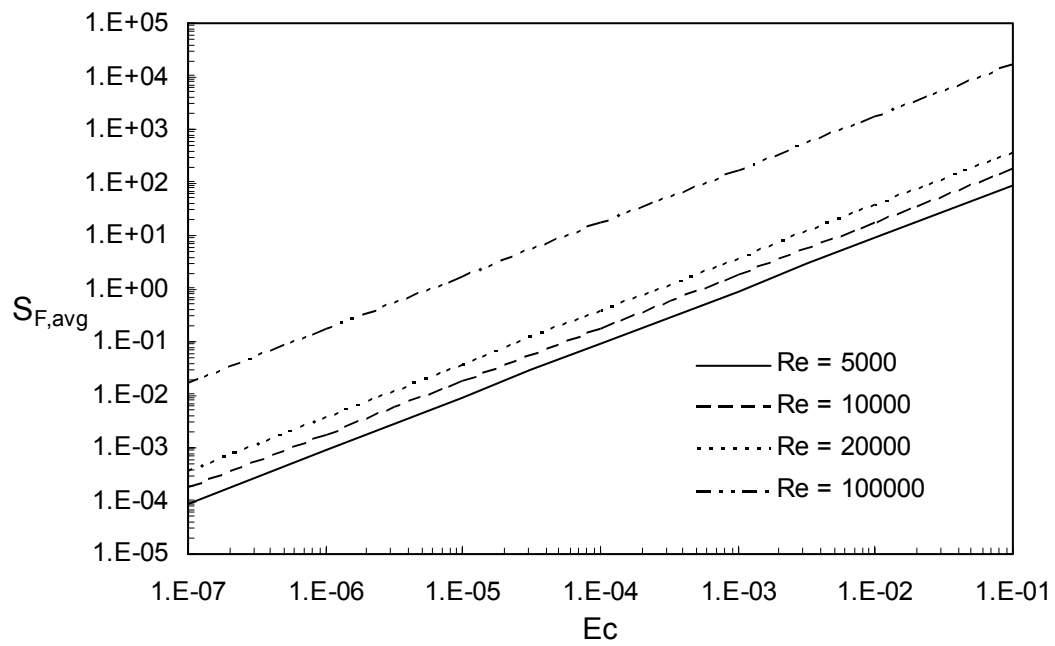


Fig 6-45: Effect of Eckert number on average fluid friction entropy generation for different Reynolds number

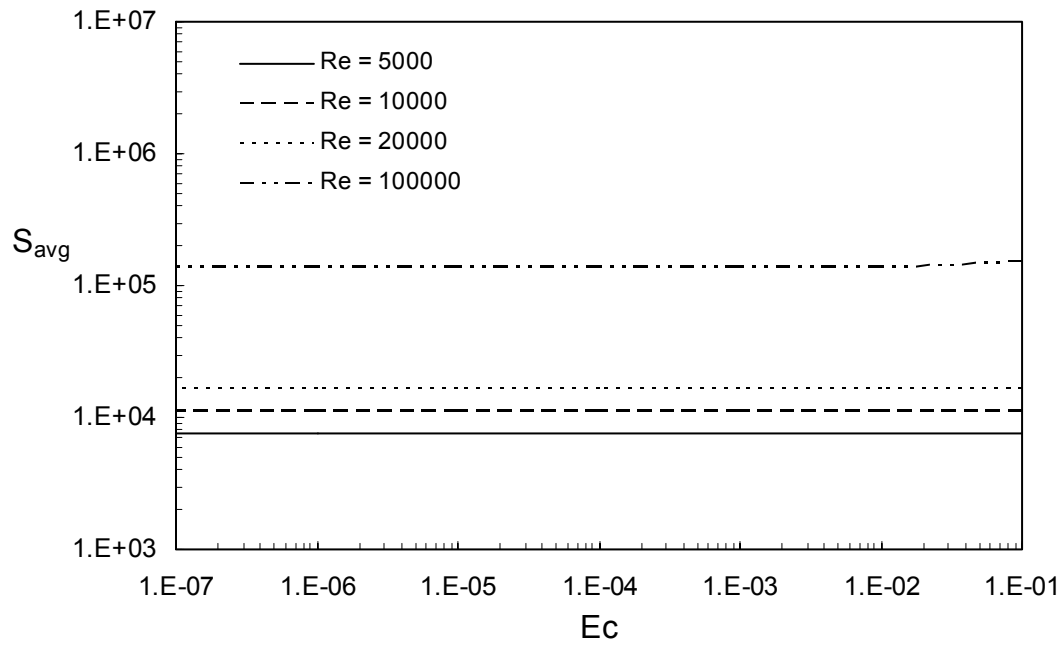


Fig 6-46: Effect of Eckert number on average entropy generation profile for different Reynolds numbers

6.4.5 Bejan number and Irreversibility ratio:

Figure 6.47 shows the effect of Eckert number on Irreversibility ratio. It can be seen from equation (3.22), that the Ec_m term is multiplied by the fluid friction term, which results in the increase in fluid friction as Eckert number increases and accordingly this figure shows that as the fluid velocity is increased, the fluid friction increases and hence the entropy generation due to the fluid friction or due to velocity gradients also increases. Figure 6.48 is a cross plot of Figure 6.47, which shows that the increase in Reynolds number has less effect on Irreversibility ratio when compared with increase in Eckert number.

Figure 6.49 shows the effect of Eckert number on Bejan number for different Reynolds number. As can be seen from the graph, Bejan number decreases after certain value of Eckert number which is 10^{-2} , hence the fluid friction has significant effect on total entropy at high Eckert numbers. And for $Ec_m < 0.3$, the Bejan number is constant indicating that the heat transfer entropy generation is only contributing to total entropy generation and fluid friction entropy generation is negligible which confirms our discussion in previous results. Figure 6.50 is a cross plot of Figure 6.49, indicating that increasing Reynolds number decreases the Bejan number however this decrease is small in magnitude at low Ec_m .

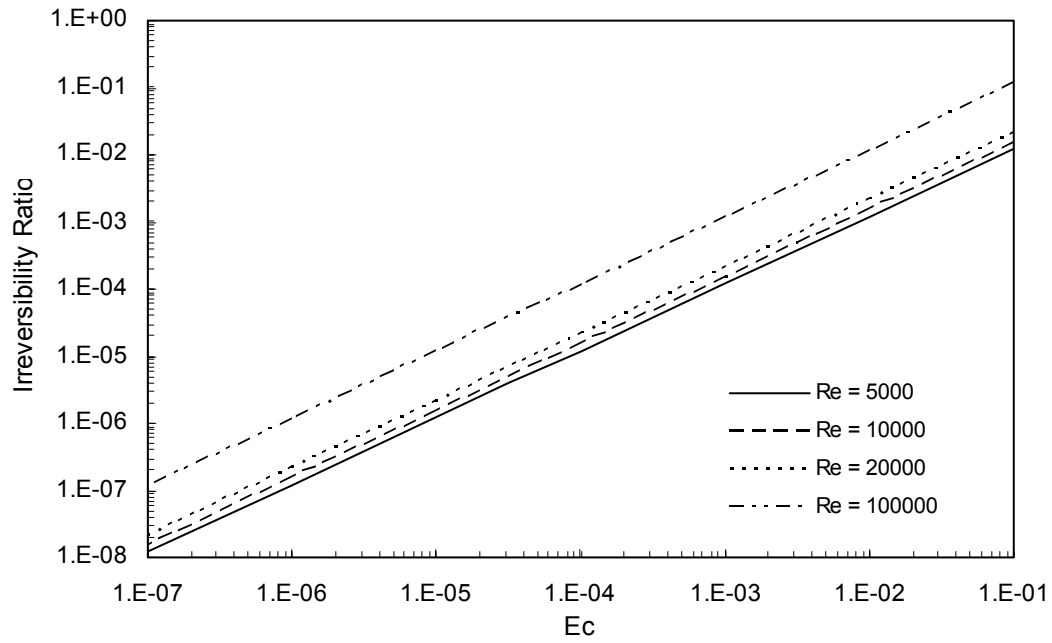


Fig 6-47: Effect of Eckert number on irreversibility ratio for different Reynolds number

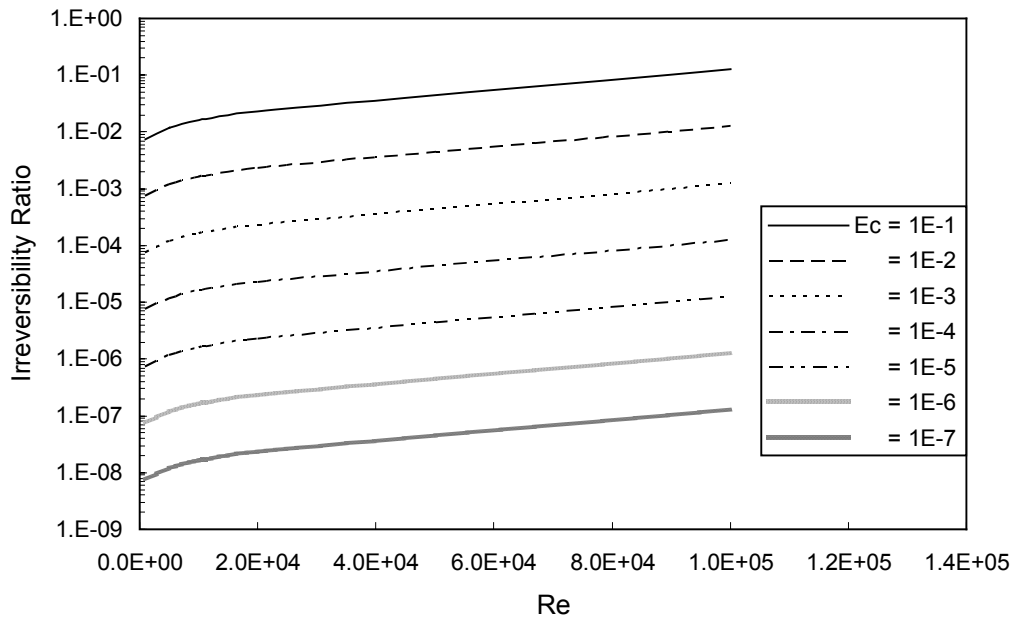


Fig 6-48: Effect of Reynolds number on irreversibility ratio for different Eckert number

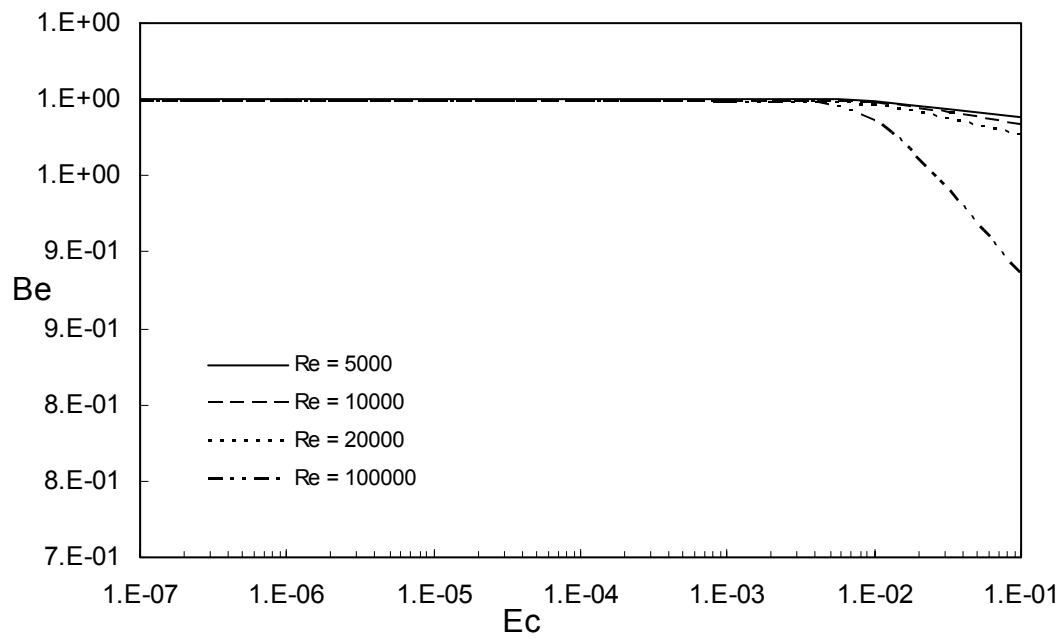


Fig 6.49: Effect of Eckert number on Bejan number for different Reynolds number

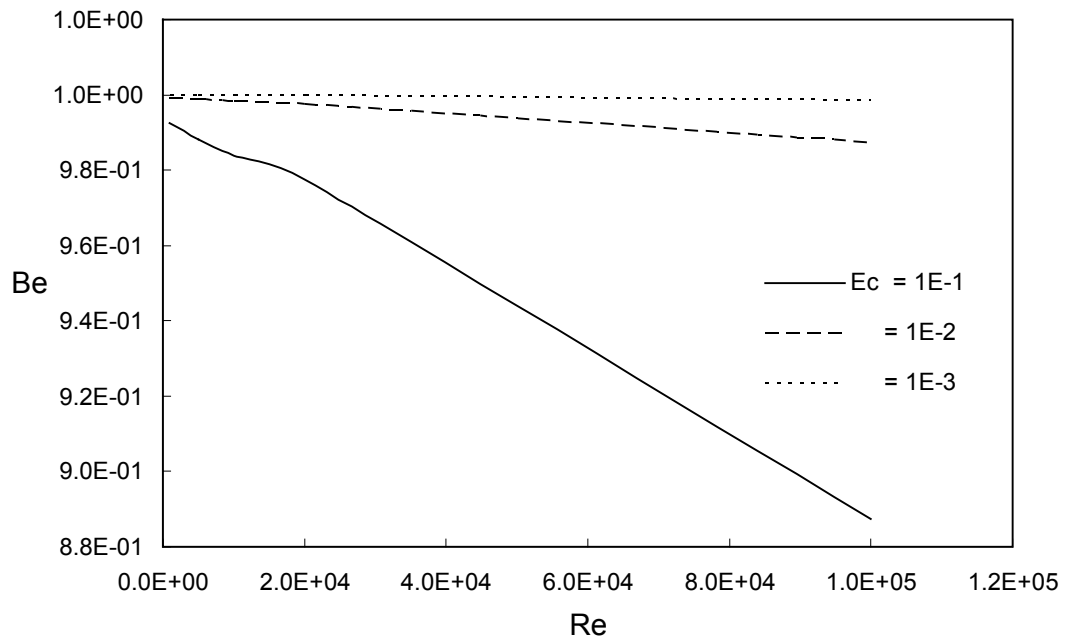


Fig 6-50: Effect of Reynolds number on Bejan number for different Eckert number and UHF cases.

CHAPTER VII

RESULTS AND DISCUSSIONS FOR MIXED CONVECTION

7.1 Introduction:

Whenever the free stream velocity is small and the temperature difference between the sphere surface and the surrounding fluid is large, the buoyancy effects may not be neglected as in the case for pure forced convection. Hence the study of laminar mixed convection around a sphere is of great importance. In this chapter, the results of solving the governing continuity, momentum and energy equations and computing local and average entropy generation are presented for mixed (forced and free) convection case. These clarify the effect of the controlling parameters like Reynolds number, Grashof number and Eckert number on flow field and entropy generation. The results for both the aiding ($Gr > 0$) and opposing flows ($Gr < 0$) for both uniform wall temperature and uniform Heat flux cases are presented and discussed in this chapter and compared with those for pure forced convection discussed in chapter VI.

7.2 Uniform wall temperature Case (Mixed convection):

The range of Grashof number was between 10^0 and 10^8 for both aiding and opposing flows; where as the ranges of the other controlling parameters are same as given in section 6.2.

7.2.1: Meridional and radial velocity profiles:

In order to show the effect of superimposed free convection (i.e. $Gr \neq 0$) on the developing meridional velocity U , Fig. 7.1 presents, for $Re = 10^4$, the obtained meridional velocities at two different meridional stations, $\theta = 60^\circ$ and 90° and for three selected Grashof numbers ($Gr = 0, \pm 10^8$). The aiding free convection tends to increase the fluid velocity as compared with the case of forced convection flow ($Gr = 0$), while an opposing free convection causes a decrease in the velocity component. It can be seen from the figure 7.2 that the effect of superimposed free convection is unremarkable at the front stagnation point, since the thermal boundary layer has not yet sufficiently developed. However as the flow moves towards the equator, such effect becomes increasingly remarkable. It is also worth mentioning that the velocity profile has a zero value at the sphere surface (i.e. $Z = 0$) and increases gradually till it reaches the edge of boundary layer where it approaches the free stream velocity.

The radial velocity W is similarly influenced by a superimposed free convection. Hence the opposing free convection makes the velocity boundary layer develop faster than it would with an aiding free convection. This phenomenon may be attributed to the previously mentioned effect of free convection on the meridional velocity component. An aiding free convection causes an increase in the meridional velocity near the heated boundary and, due to continuity principle; this makes more fluid come to the sphere from region far away. Thus an aiding flow causes the radial velocity component W to have a larger (negative) value than does an opposing free convection as seen in the Fig- 7.3.

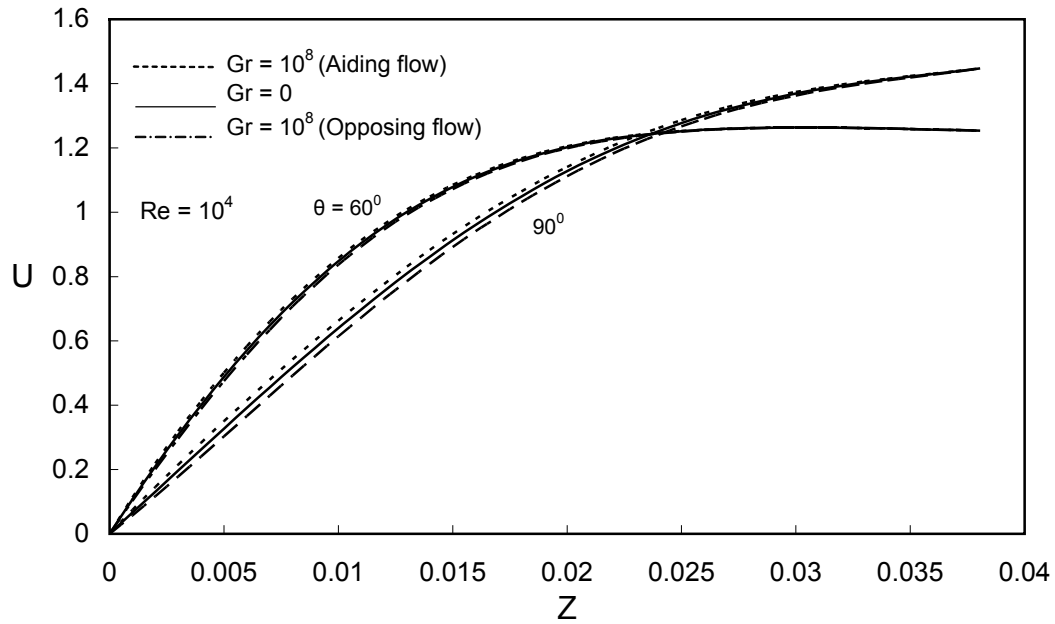


Fig 7-1: Variation of meridional velocity with radial distance for two different meridional stations

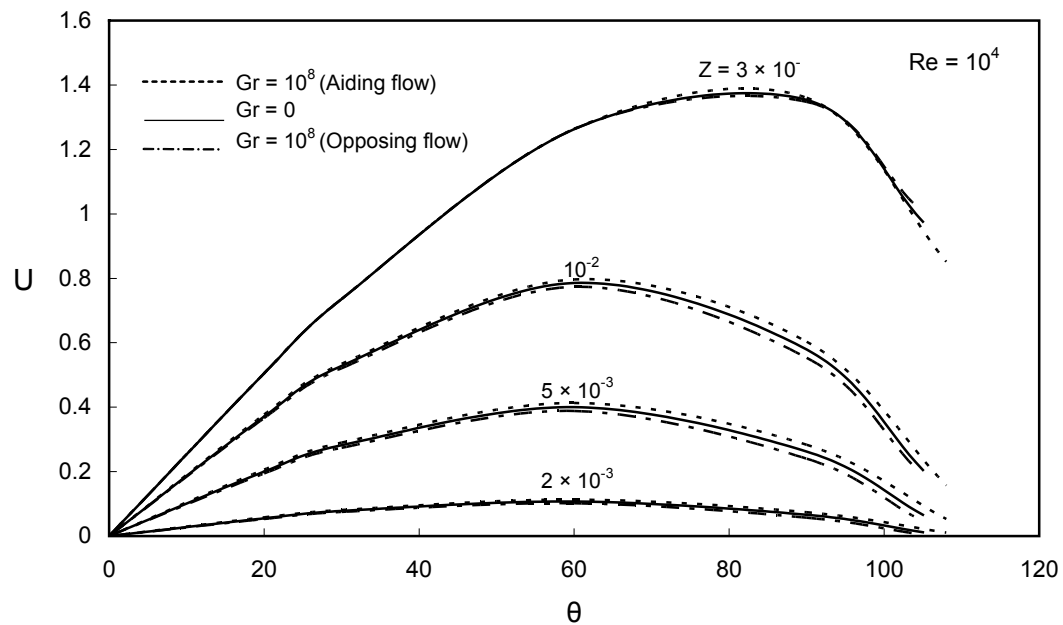


Fig 7-2: Variation of meridional velocity over the sphere surface

7.2.2: Temperature profile:

Figure 7.4 presents the temperature profiles for aiding and opposing flows and for a particular meridional station ($\theta = 90^\circ$). This figure shows the variation of the temperature profiles as the boundary layer increases along the surface of the sphere until the edge of boundary layer is encountered. As expected, the wall of the sphere is at the maximum dimensionless temperature, which is equal to one, and as we move away from the sphere, the temperature over the sphere decreases. And this phenomenon is the same for both aiding and opposing flows. Moreover the aiding flow tends to decrease the fluid temperature when compared to pure forced convection and an opposing flow tries to increase the fluid temperature over the sphere in comparison with pure forced convection ($Gr = 0$) case.

7.2.3: Local entropy generation profiles:

Figure 7.5 shows the variation of dimensionless local heat transfer entropy generation with radial distance for different Grashof numbers. Entropy generation profiles are directly related to gradients of temperature, meridional and radial velocity components in the domain. As discussed earlier the temperature profiles decreases as we move in Z -direction from sphere surface, which results in a decrease in the thermal boundary layer thickness and an increase in the temperature gradients near the surface due to the fact that the entropy generation rate is very high near the surface than far away.

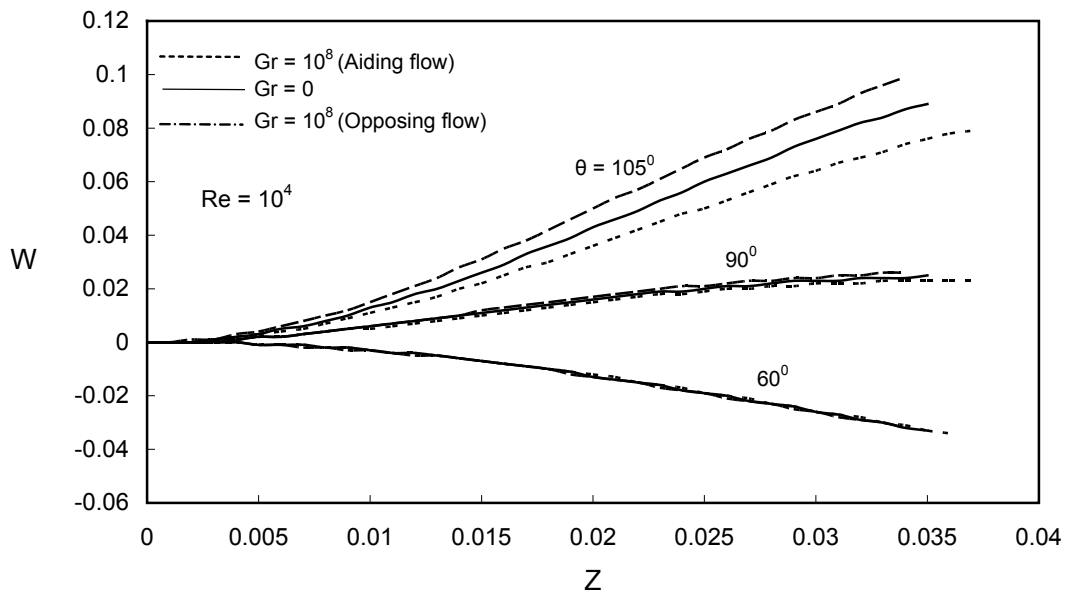


Fig 7-3: Variation of radial velocity with radial distance at different radial locations

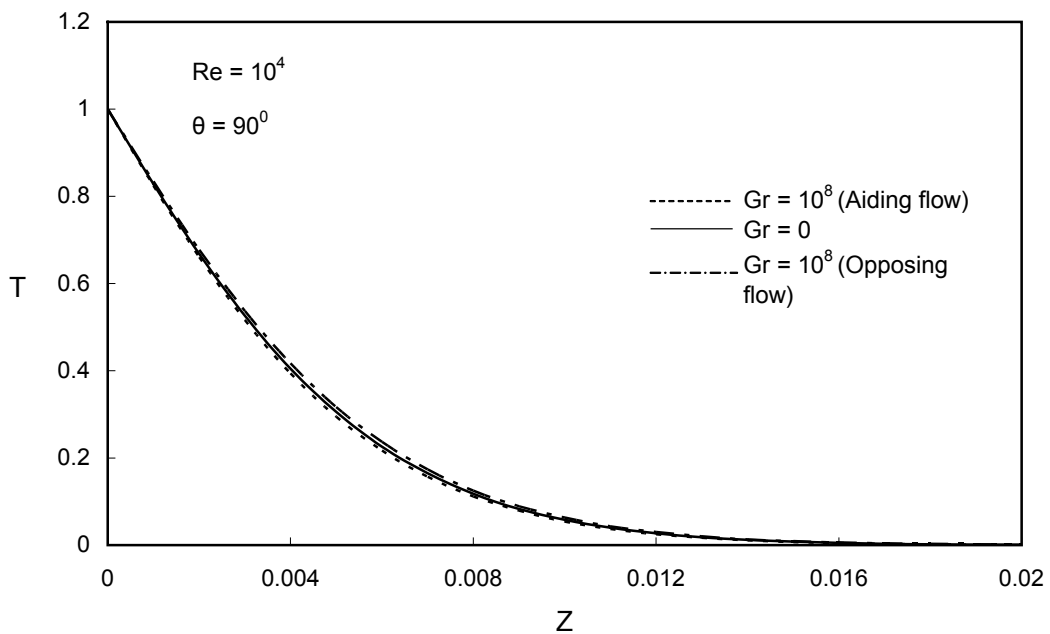


Fig 7-4: Temperature profile for different Grashof number at given meridional station

Moreover the aiding free convection causes higher temperature gradients than the pure forced convection ($Gr = 0$) which result in high heat transfer and high heat transfer entropy generation while the opposing flow has an opposite effect. It can also be noted here that the superimposed free convection is not much noticeable near the stagnation point, but as we move away from the front stagnation point, the effect is increasingly remarkable. The same effect is observed in the figure 7.6, which shows the variation of local Heat transfer entropy generation with radial distance for different Reynolds numbers. Higher Reynolds number dominates the effect of Grashof number due to which, for $Re = 10^4$, the aiding and opposing free convection has very less effect on the variation of heat transfer entropy generation.

Figure 7.7 shows the variation of dimensionless heat transfer entropy generation for a given Reynolds number ($Re = 10^4$) and at a selected meridional angle ($\theta = 105^\circ$). As the Grashof number decreases, the effect of Re is dominant.

Figure 7.8 shows the variation of local fluid friction entropy generation with radial distance at two different meridional stations ($\theta = 60^\circ, 105^\circ$). This figure shows that entropy generation due to fluid friction is less in magnitude at smaller angles and increases with the angle and then again decreases near the separation point. As discussed earlier, the aiding free convection causes the meridional and radial velocity

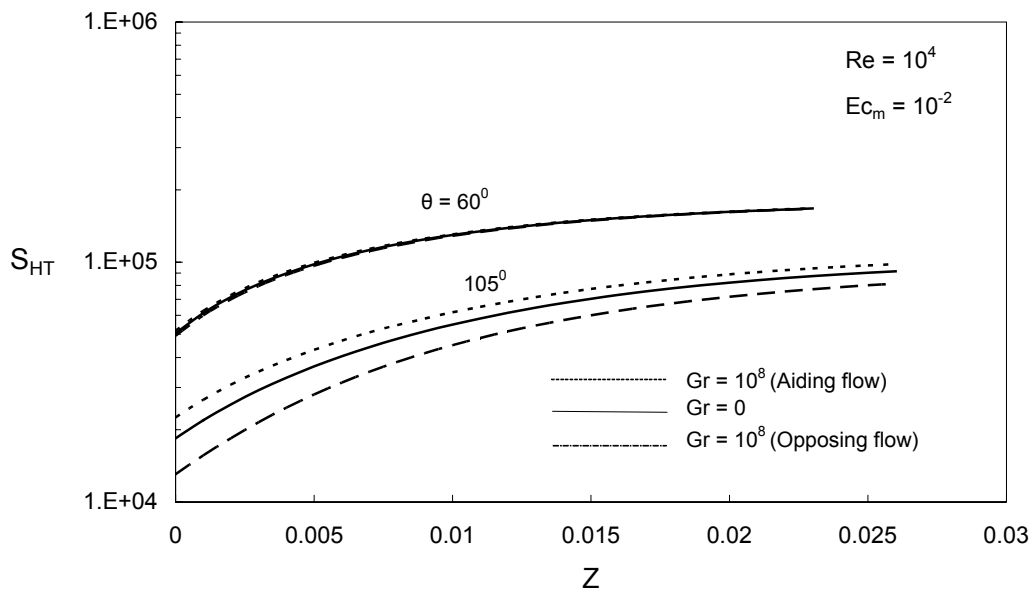


Fig 7-5: Variation of local heat transfer entropy generation with radial distance for two selected meridional angles

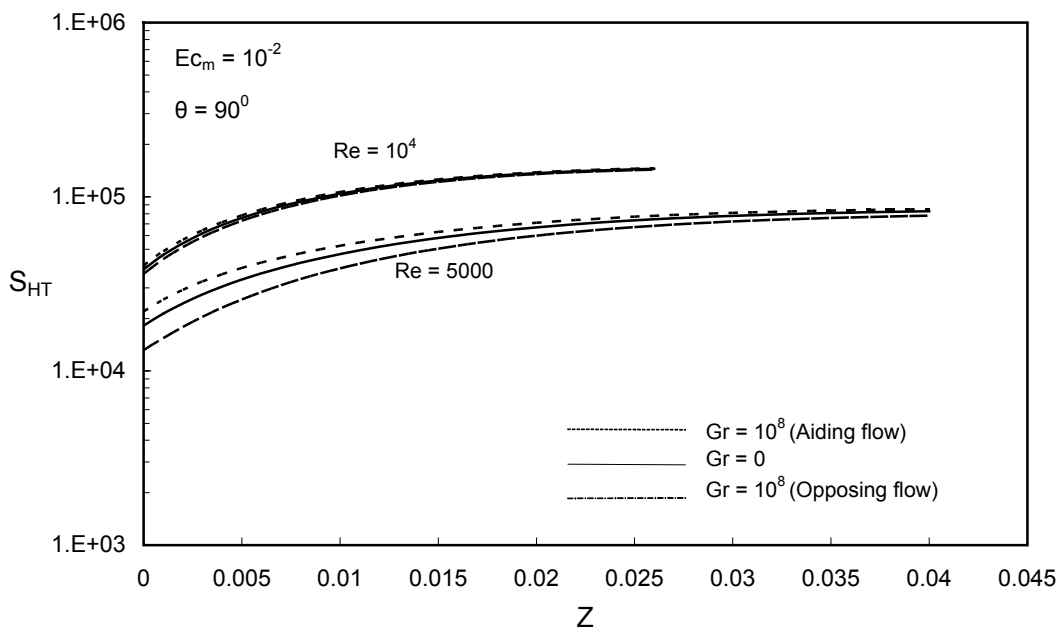


Fig 7-6: Variation of local heat transfer entropy generation with radial distance for different Reynolds numbers

components to be higher, the velocity gradients are also higher near the surface resulting in an increase in the fluid friction entropy generation rate near the surface. This can be attributed to the higher kinetic energy of the fluid particles away from the sphere surface. Moreover the meridional locations closer to the point of external flow separation have comparatively less fluid friction at the sphere surface. The opposing flow causes the fluid velocity to decrease and hence decreasing the velocity gradients when compared with the pure forced convection. It can also be noted that the effect of aiding or opposing flow is more pronounced far away from the front stagnation point.

Figure 7.9 shows the variation of total entropy generation with radial distance at two meridional stations ($\theta = 60^\circ, 105^\circ$) and given Reynolds number ($Re = 10^4$). The total entropy generation has the same behavior as the heat transfer entropy generation alone, because the fluid friction entropy generation is having magnitude of 10^2 lower when compared with heat transfer entropy term. This results in heat transfer entropy generation to be dominant and it is also clear from the figure 7.5, the aiding flow has the tendency to increase the velocity and temperature gradients by decreasing the thermal boundary layer thickness, and hence increases the total entropy generation. The opposing flow decreases the temperature and velocity gradients and hence decreases the total entropy generation.

Figure 7.10 shows the variation of total entropy generation with radial distance for seven different Grashof numbers and for given Reynolds. The behavior of the curve is similar to the case of Heat transfer entropy generation.

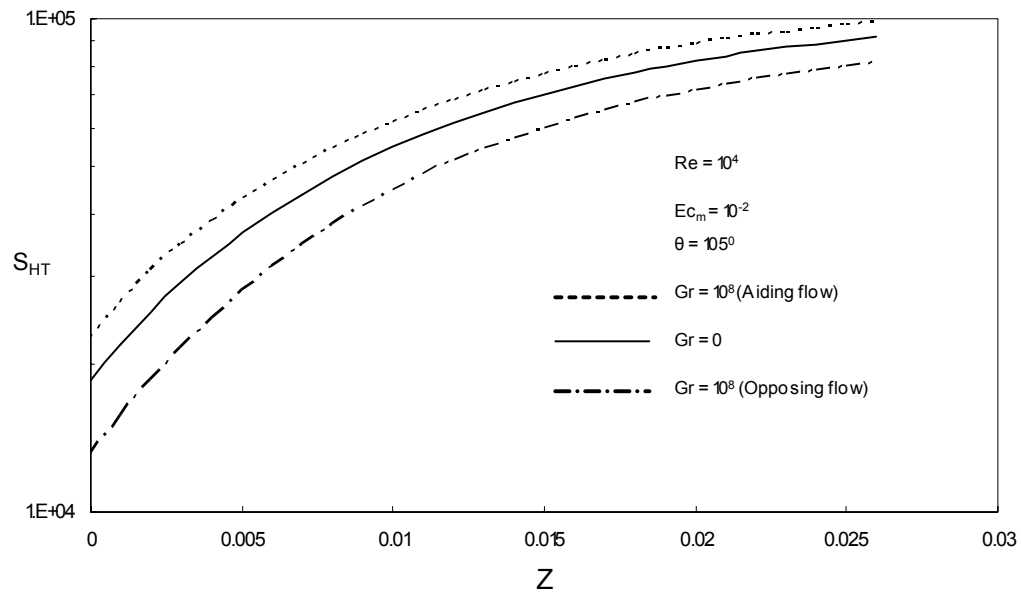


Fig 7-7: Variation of local heat transfer entropy generation for different Grashof numbers

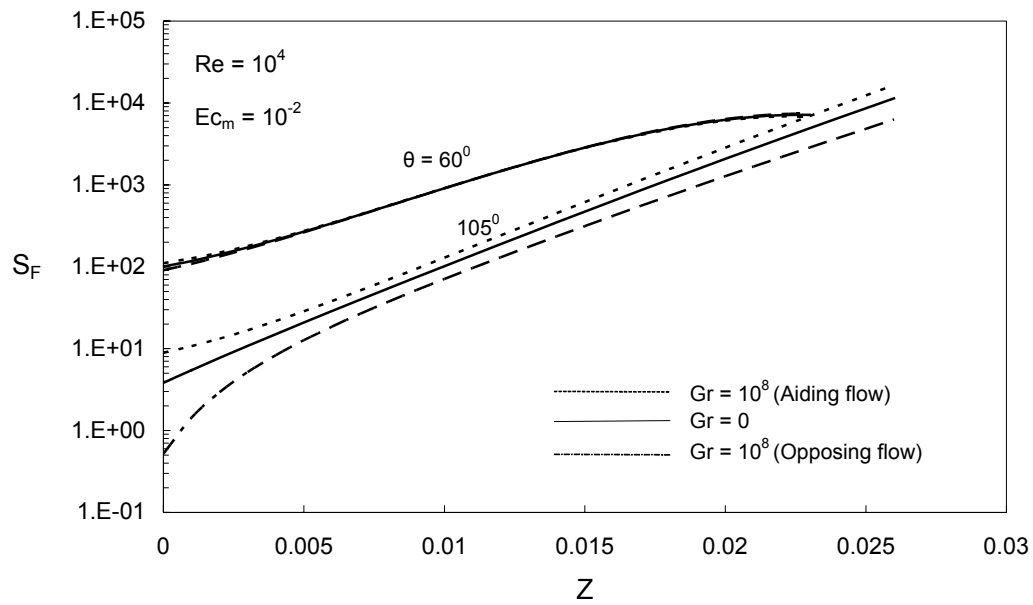


Fig 7-8: Variation of local fluid friction entropy generation with radial distance at two different meridional stations

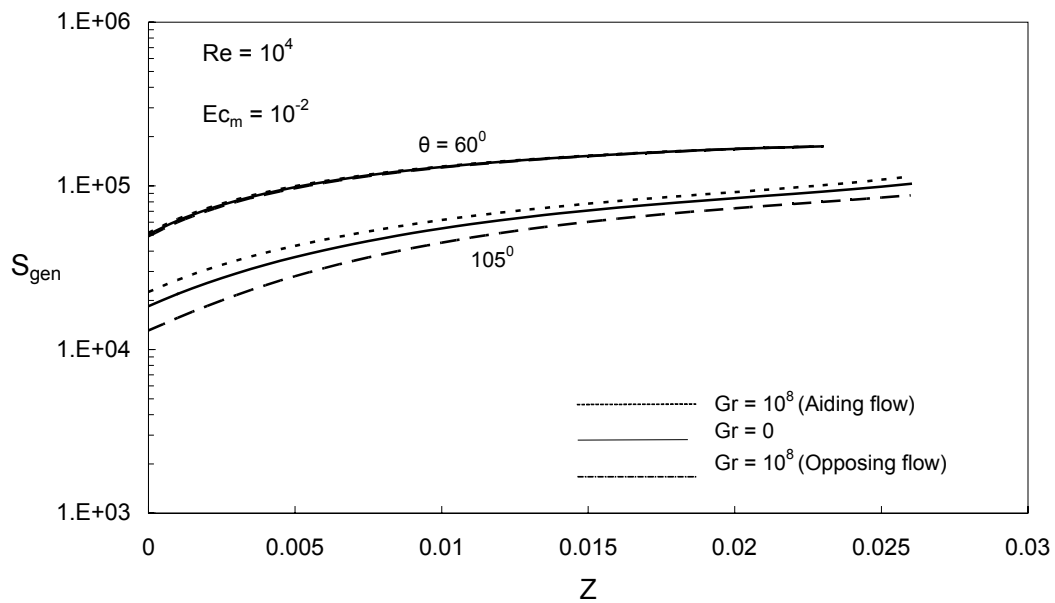


Fig 7-9: Variation of local entropy generation with radial distance and at two meridional stations

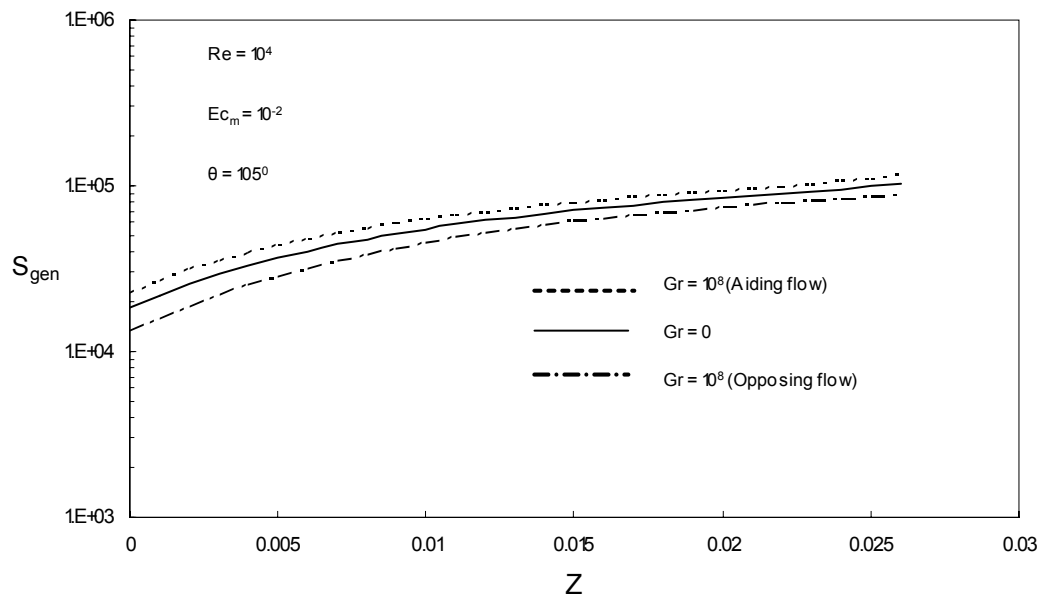


Fig 7-10: Variation of local entropy generation for different Grashof numbers

Figure 7.11 is a cross plot of the figure 7.9, where total entropy generation is plotted for some selected values of dimensionless radial distance from the wall (Z) for some of the investigated values of Gr . The entropy generation increasing as the thermal boundary layer increases from the front stagnation point and again decreases as we move towards the separation point.

Figure 7.12 shows a comparison between dimensionless entropy generation due to heat transfer and due to fluid friction. Similar to the case of $Gr = 0$ in the previous chapter, the entropy generation due to heat transfer is of very high magnitude in comparison with fluid friction entropy generation, both for aiding free convection and opposing free convection. Hence for most of the practical analysis cases in which Reynolds number is low about $Re = 10^4$ or less, the fluid friction entropy generation can be neglected. Figure 7.13 shows the total entropy generation for different Eckert number, it is clear from the figure that Eckert number less than 10^{-2} has no effect on the total entropy generation.

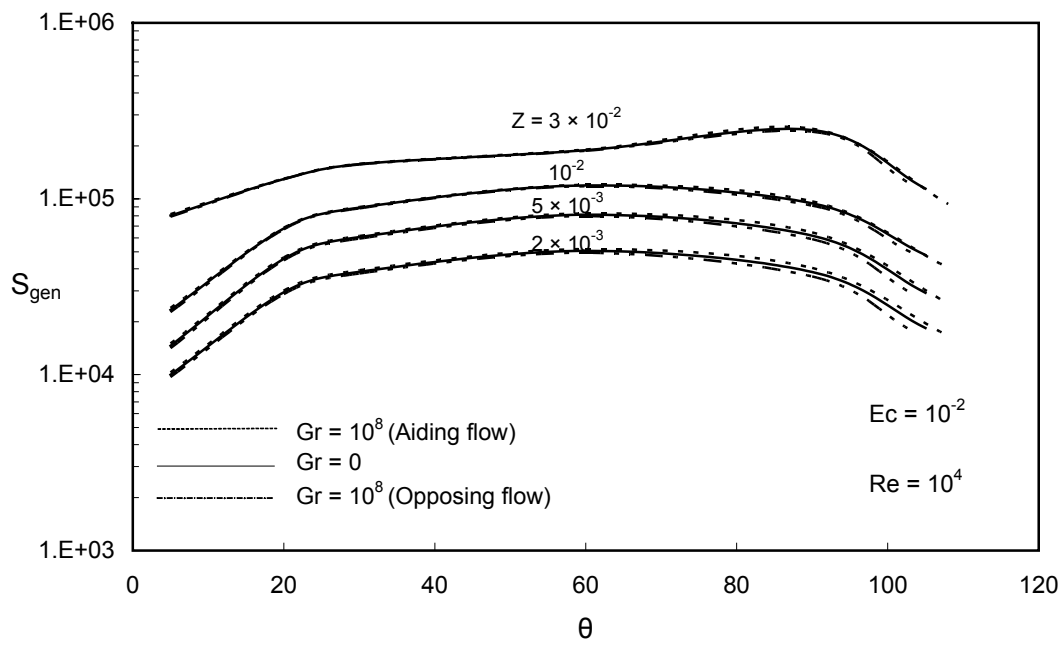


Fig 7-11: Local entropy generation for different Grashof number over the surface of the sphere

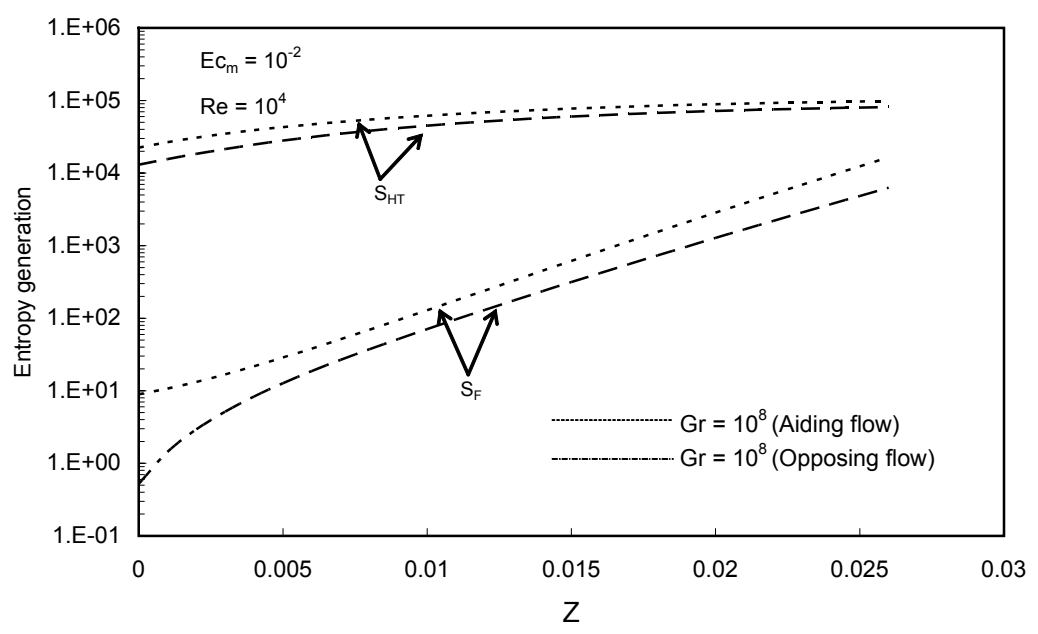


Fig 7-12: Comparing heat transfer and fluid friction entropy generation for different Grashof number along radial direction

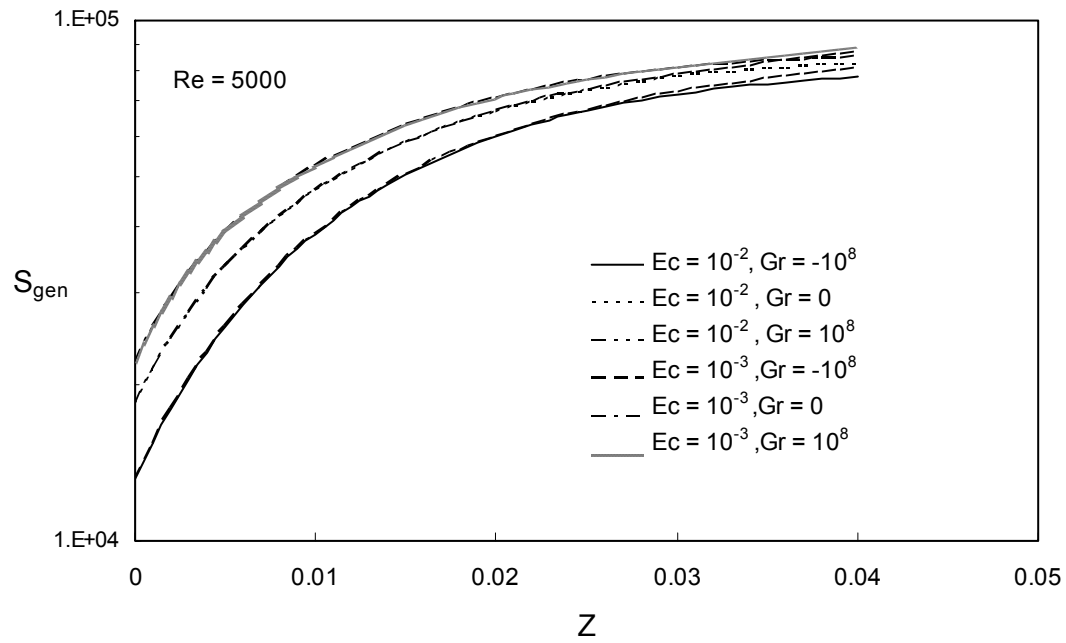


Fig 7-13: Comparing entropy generation profile for different Grashof number and Eckert number at a given Re (= 5000) and at $\theta = 105^\circ$

7.2.4: Local and overall average entropy generation profiles:

It can be seen from the Figure 7.14 that higher fluid friction increases the fluid friction entropy generation. Since the fluid particles over the sphere accelerate in the region $0 \leq \theta \leq 90^\circ$ and decelerate in the region where $\theta > 90^\circ$, hence the pressure decreases in the accelerated region and then increases in the decelerated region. Since the external pressure is imposed at the boundary layer, the transformation of the pressure into kinetic energy takes place in the accelerated region and a great deal of the kinetic energy of the particles adjacent to the wall is consumed to move against the friction forces. This can also be related to the velocity gradients, which are high in accelerating region of flow and less in decelerating region of fluid flow. The heat transfer entropy generation is having a dominant effect in total entropy generation as can be seen from the graph. Moreover, positive Grashof number, i.e. the aiding flow tends to increase the entropy generation than the opposing flows.

Figure 7.15 shows the variation of local average entropy generation over the sphere surface for different values of Reynolds number ($Re = 5 \times 10^3, 10^4$ and 2×10^4) and for some selected values of Grashof number. We can notice that at higher Re , entropy generation is higher due to small viscous and thermal boundary layer, which results in higher velocity and temperature gradients and hence higher heat transfer, but at the expense of higher entropy generation. Positive Grashof number tends to decrease the thermal boundary layer thickness and increase the temperature and velocity gradients resulting in higher entropy generation than for pure forced convection.

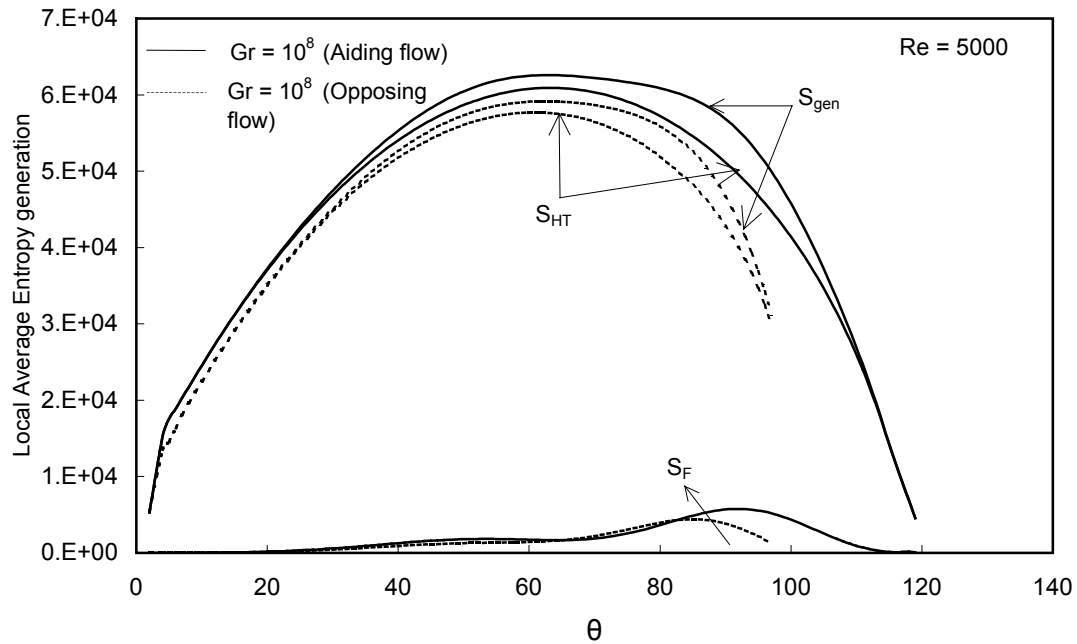


Fig 7-14: Variation of local average entropy generation over the sphere surface for a given Reynolds and Eckert number

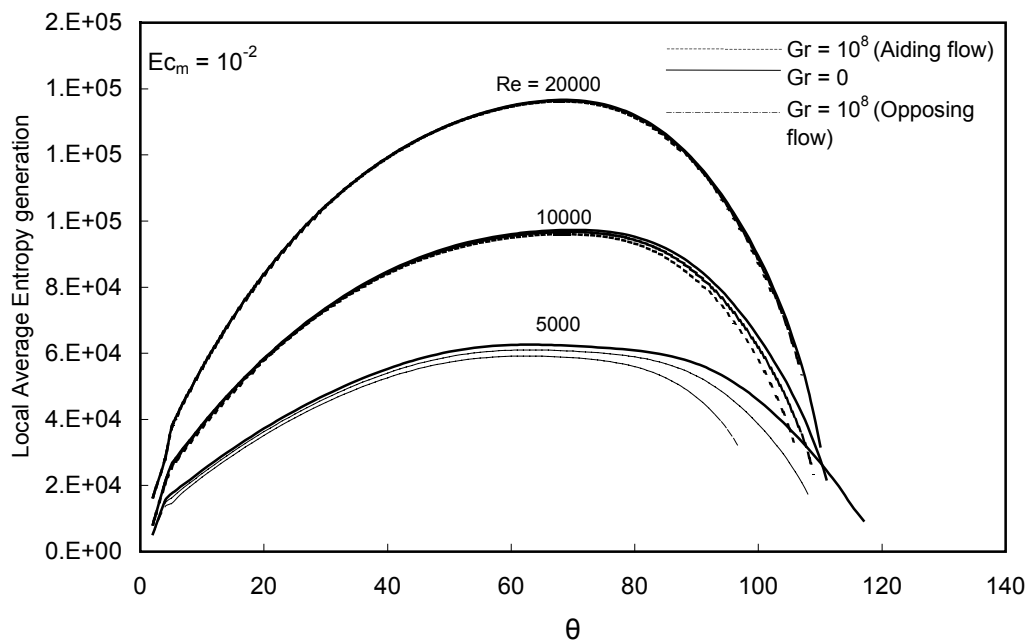


Fig 7-15: Comparing local average entropy generation profile for different Reynolds numbers and Grashof numbers and for a given Eckert number

Similarly, negative Grashof numbers tries to increase the boundary layer thickness and hence decrease the velocity and temperature gradients, thus decreasing the entropy generation. It can be noted that the higher Grashof numbers results in high Nusselt number and hence higher heat transfer rates which is desired phenomenon in many thermal systems but at the loss of some useful energy in the form of entropy generation.

Figure 7.16 shows the variation of local average entropy generation over the sphere for given Reynolds and Eckert number. The plot indicates that high Grashof number, in aiding or opposing directions, has a considerable effect. Further more, the aiding flow increases the entropy generation while an opposing flow tends to reduce it.

Figure 7.17 shows the variation of local average entropy generation for a given Reynolds number. As seen in figure 7.15, here also the entropy generation profile is increasing as we move from the front stagnation point and again decreases near the separation point. Higher Eckert number results in higher fluid friction entropy generation and hence increase total entropy generation. As seen in previous figures, a positive Grashof number increases the entropy generation and a negative Grashof number decreases the total entropy generation, which is a desired phenomenon in most of the power systems, so as to save useful power or work, but at the same time with more heat transfer.

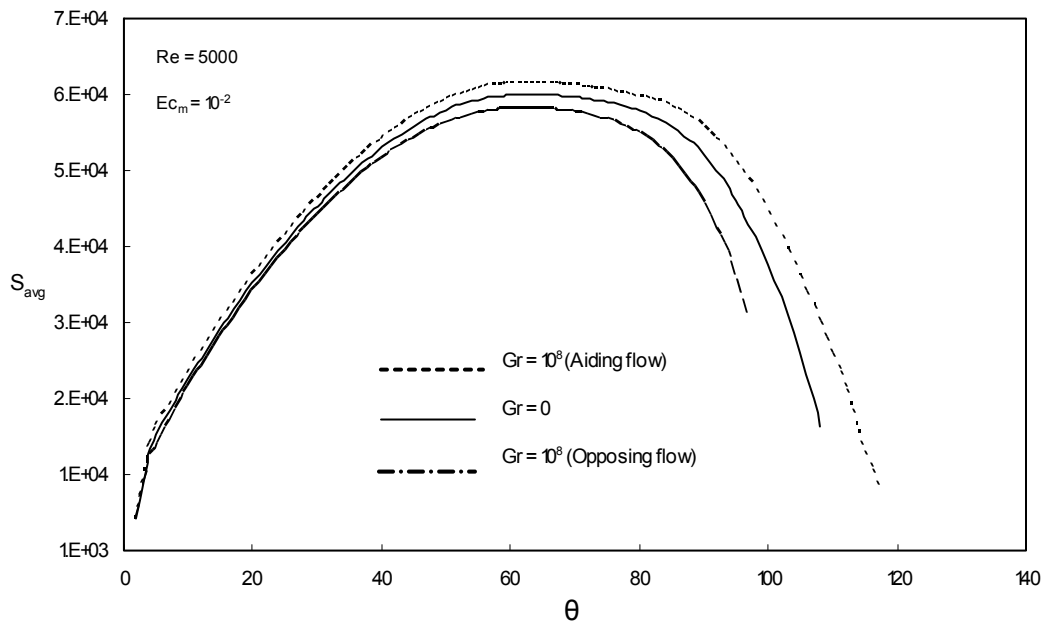


Fig 7-16: Variation of local average entropy generation for given Reynolds and Eckert number and different Grashof numbers

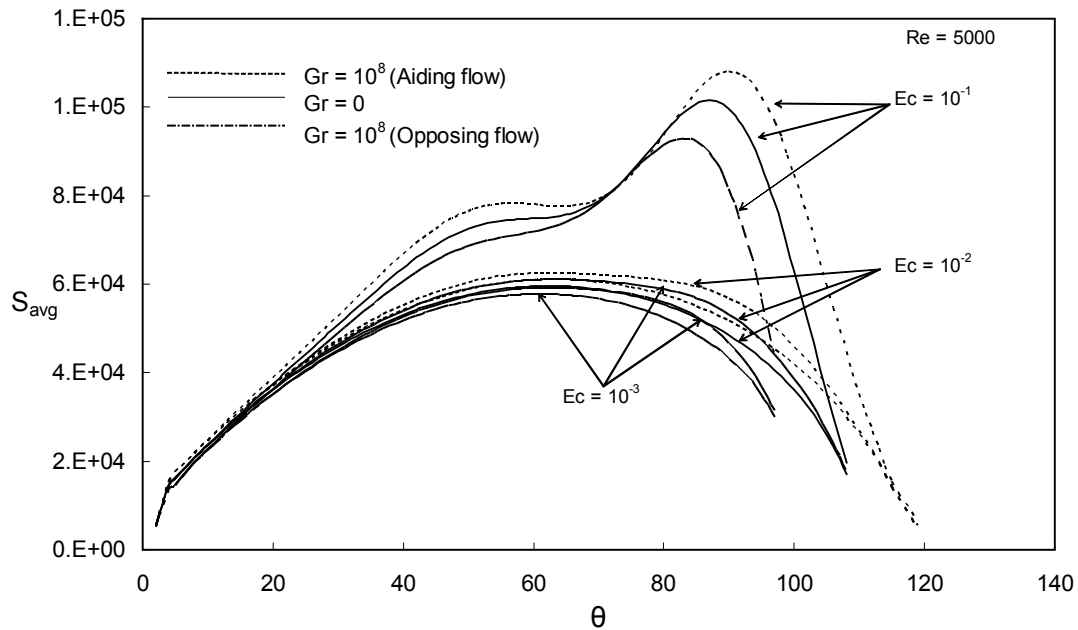


Fig 7-17: Variation of local average entropy generation over the sphere surface for a different Eckert number

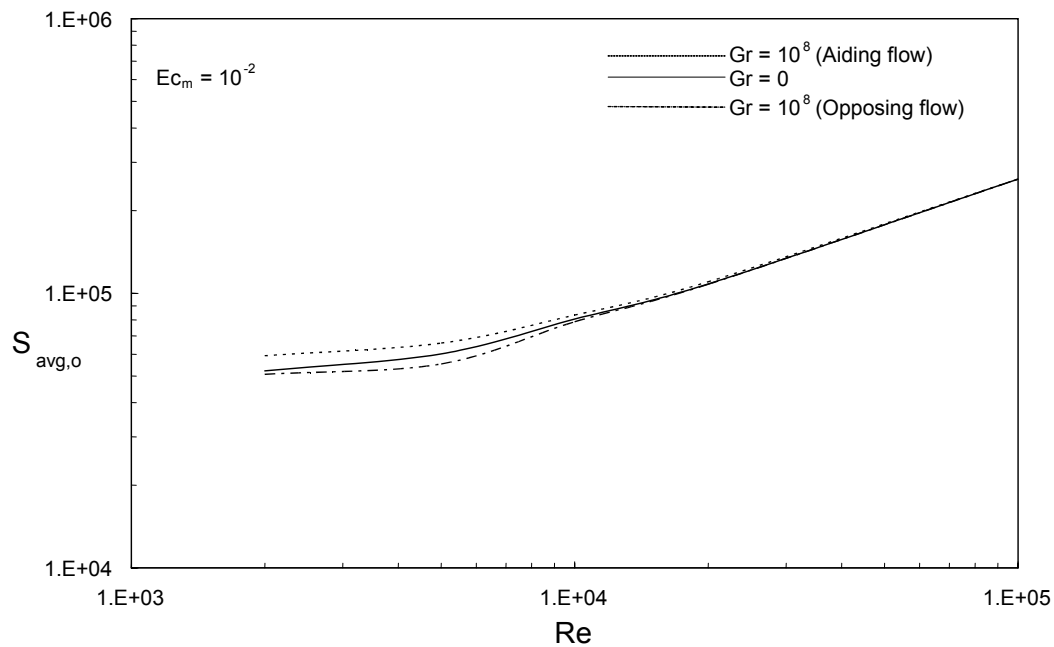


Fig 7-18: Effect of Reynolds number on overall average entropy generation profile for different Grashof numbers

Figure 7.18 shows the effect of Reynolds number on total entropy generation for the case of mixed convection. Here the graph is plotted with some selected values of Grashof number. At low Reynolds number and high Grashof number makes the flow turbulent, so the range of Reynolds number selected in this graph is 2×10^3 to 10^5 . As the Reynolds number increases, the Grashof number has very less effect on the flow and temperature fields. This is clear from the graph, which shows that for low Reynolds number, and high Grashof number (aiding or opposing) the entropy generation change is remarkable and as the Reynolds number increases, the same magnitude of Grashof number has very little effect on the entropy generation change.

7.2.5 Bejan number and Irreversibility Ratio:

Figure 7.19 shows the effect of Reynolds number on Irreversibility ratio for different values of Grashof number. It can be seen from this figure that as the Reynolds number is increased, the irreversibility ratio increases and then it decreases at a particular Reynolds number and then increases steadily which indicates that the fluid friction entropy generation is more dominant in over all entropy generation for higher Reynolds numbers.

Similarly Figure 7.20 shows the effect of Reynolds number on Bejan number for different Grashof number, it can be seen that as the Reynolds number is increased, Bejan number decreases and then increases slightly between $Re = 10000$ and $Re = 20000$, and then again decreases steadily. We can conclude with this result that as the Reynolds number is increased, the heat transfer entropy generation has little effect on the over all entropy generation.

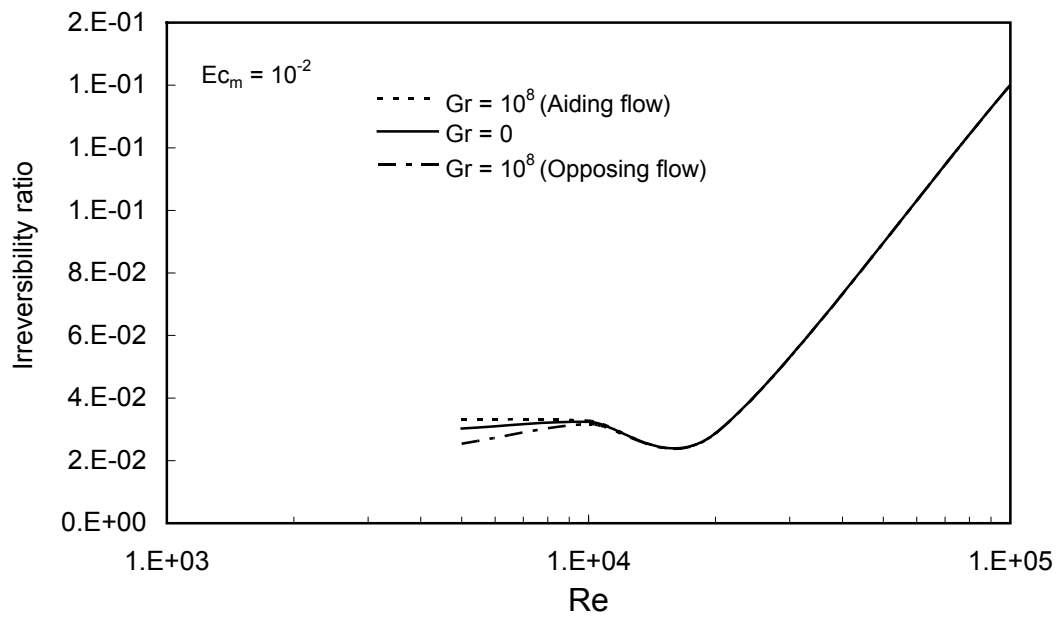


Fig 7-19: Effect of Reynolds number on irreversibility ratio for different Grashof numbers

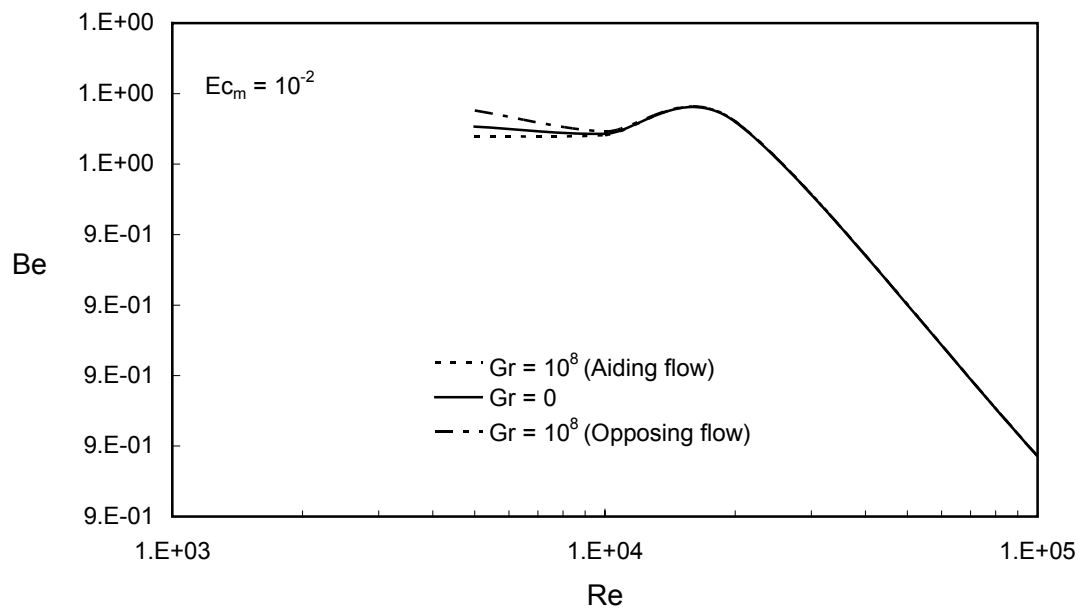


Fig 7-20: Effect of Reynolds number on Bejan number for different Grashof numbers

7.3 Uniform heat flux Case (Mixed convection):

The ranges of controlling parameters are same as given in section 7.2.

7.3.1: Meridional and radial velocity profiles:

In order to show the effect of superimposed free convection (i.e. $Gr \neq 0$) on the meridional velocity U , Figure 7.21 presents, for $Re = 10^4$ and UHF, the obtained meridional velocities at two different meridional stations, $\theta = 60^\circ$ and 90° and for selected Grashof numbers ($Gr = 0$ and $Gr = 10^9$, that represent aiding and opposing flows). It can be seen that the aiding free convection (positive Grashof number) tends to increase the fluid velocity as compared with the case of pure forced convection ($Gr = 0$), while an opposing free convection (negative Grashof number) causes a decrease in this velocity component similar to case of UWT seen in section 7.2. Figure 7.22 shows the variation of meridional velocity U , over the sphere at different radial locations. The effect of superimposed free convection is usually unremarkable at the front stagnation point, since the thermal boundary layer has not yet sufficiently developed. However as the flow moves further over the sphere, such an effect becomes increasingly remarkable. As expected, the velocity profile has a zero value at the sphere surface (i.e. $Z = 0$) which represents the no slip condition on the sphere surface and increases gradually till it reaches the edge of boundary layer where it approaches the free stream velocity.

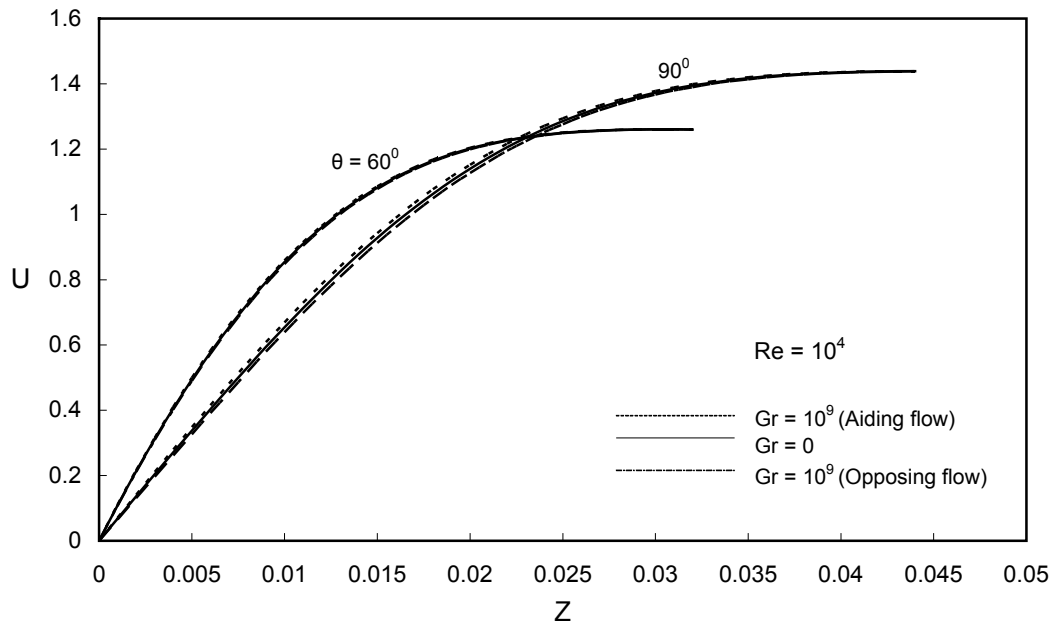


Fig 7-21: Meridional velocity profile for two different meridional stations

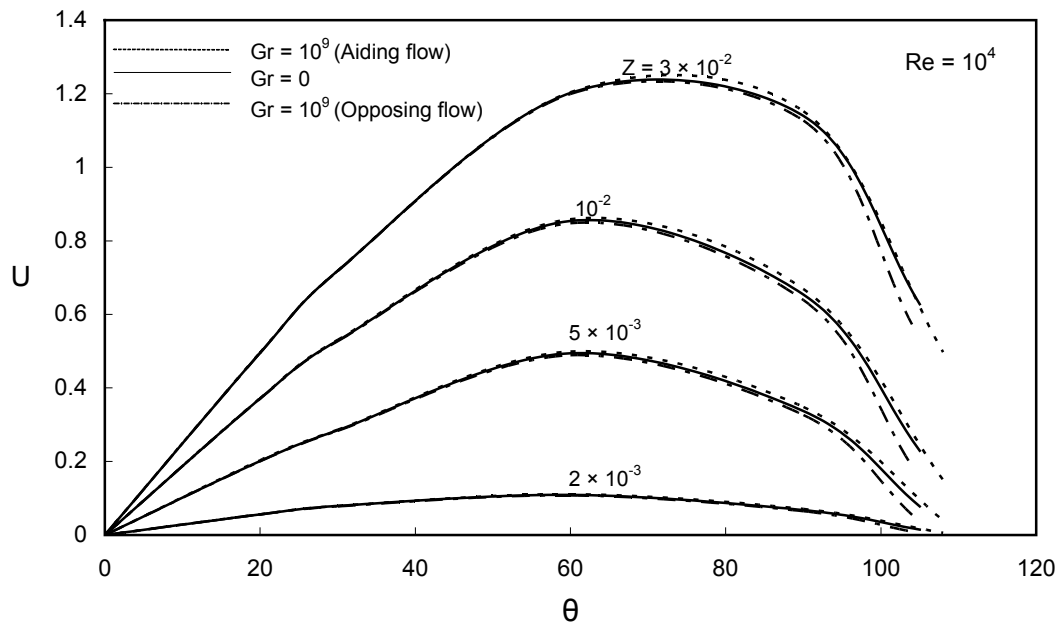


Fig 7-22: Meridional velocity profile for different Grashof number over the sphere surface

The radial velocity W is similarly influenced as the meridional velocity U , by a superimposed free convection. Hence the opposing free convection makes the azimuthal velocity boundary layer develop faster than it would with an aiding free convection. An aiding free convection causes an increase in the meridional velocity near the heated boundary and, due to continuity principle; this makes more fluid come towards the sphere from region far away. Thus an aiding flow causes the radial velocity component W to have a larger (negative) value than does an opposing free convection as shown in the figure 7.23.

7.3.2: Temperature profile:

Figure 7.24 presents the temperature profile for selected values of Grashof number and a particular meridional station ($\theta = 90^\circ$). This figure shows the variation of the temperature profiles as the boundary layer increases along the surface of the sphere until the edge of boundary layer is encountered. It can be noted that the aiding flow tends to decrease the fluid temperature when compared with pure forced convection and an opposing flow tends to increase the fluid temperature over the sphere in comparison with $Gr = 0$ case.

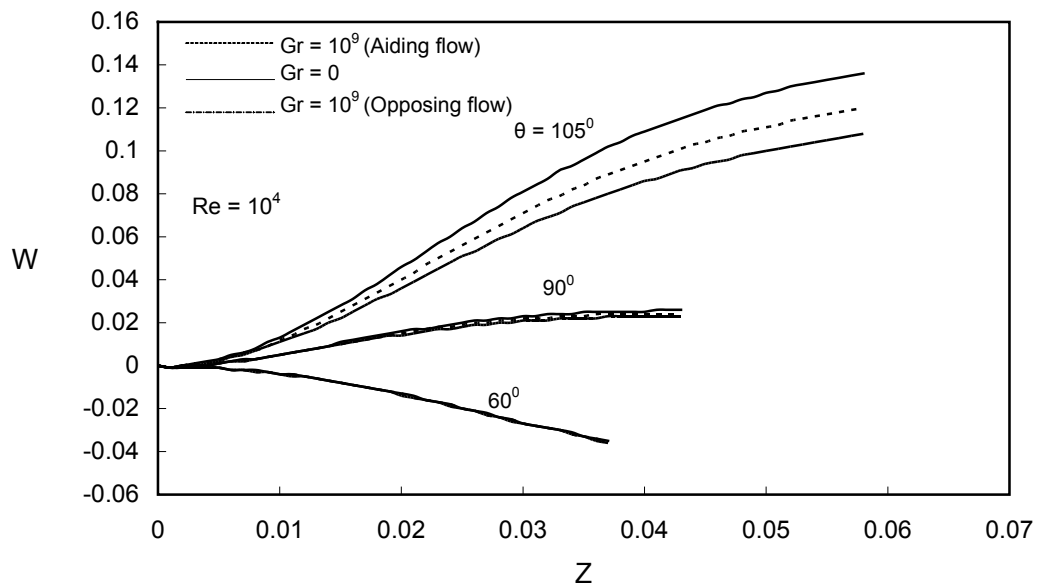


Fig 7-23: Radial velocity profile for different Grashof number at different radial locations

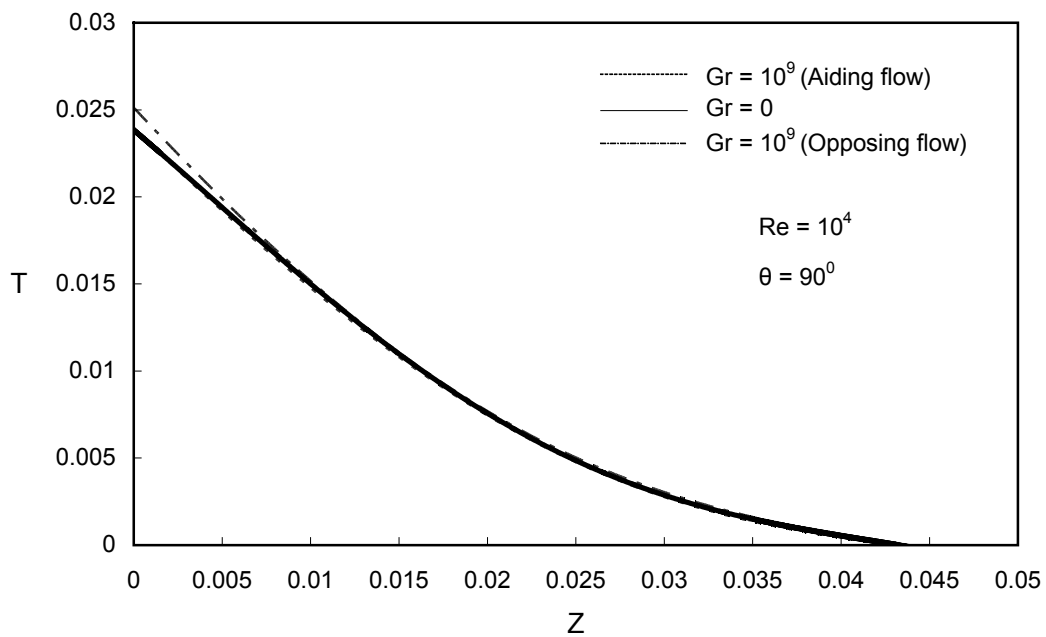


Fig 7-24: Temperature profile for different Grashof number at given meridional station

7.3.3: Local and overall average entropy generation profiles:

Figure 7.25 shows the variation of dimensionless local heat transfer entropy generation with radial distance for different Grashof numbers. The temperature profiles decrease as we move in Z-direction from sphere surface, resulting in a decrease in the thermal boundary layer and hence an increase in the temperature gradients near the sphere surface than far away. In addition, the aiding free convection results in higher temperature gradients compared with the pure forced convection ($Gr = 0$). The opposing flow has an opposite effect which results in low heat transfer and hence low entropy generation due to heat transfer. It can be noted here that the superimposed free convection is not much noticeable near the stagnation point, but as we move away from the front stagnation point, the effect is increasingly remarkable. The same effect is seen in Fig 7.26, which shows the local Heat transfer entropy generation profile for different Reynolds and Grashof numbers along Z-direction. Higher Reynolds number dominates the effect of Grashof number because of which the aiding and opposing free convection has little effect on the heat transfer entropy generation.

Figure 7.27 shows the variation of dimensionless heat transfer entropy generation along radial direction for few selected Grashof numbers and at a particular meridional location ($\theta = 90^\circ$). It is clear from the graph that, lower values of Grashof number have less effect over the entropy generation since effect of Reynolds number is dominating.

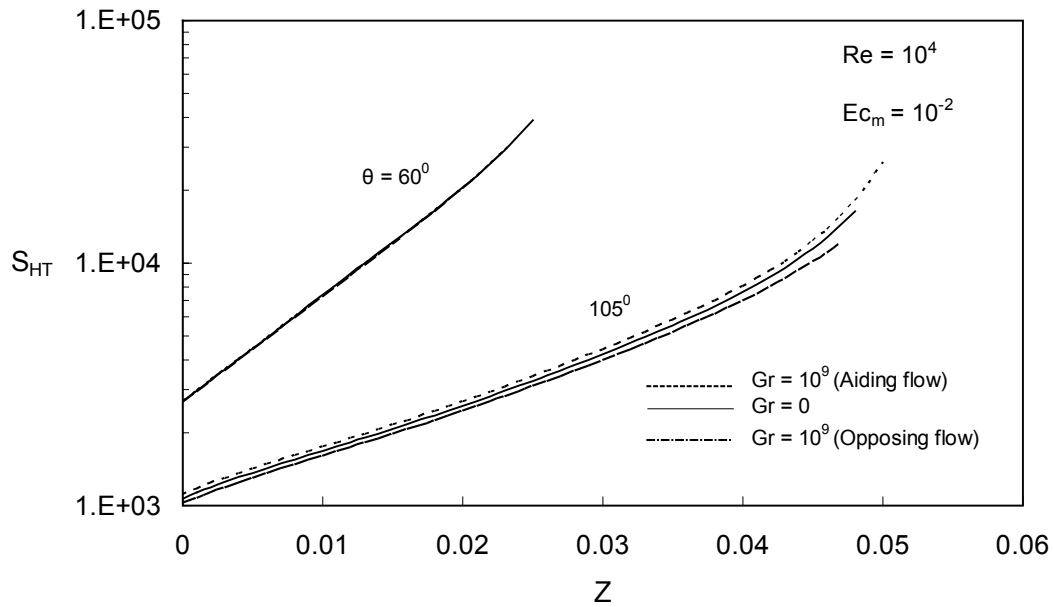


Fig 7-25: Variation of local heat transfer entropy generation for different Grashof numbers

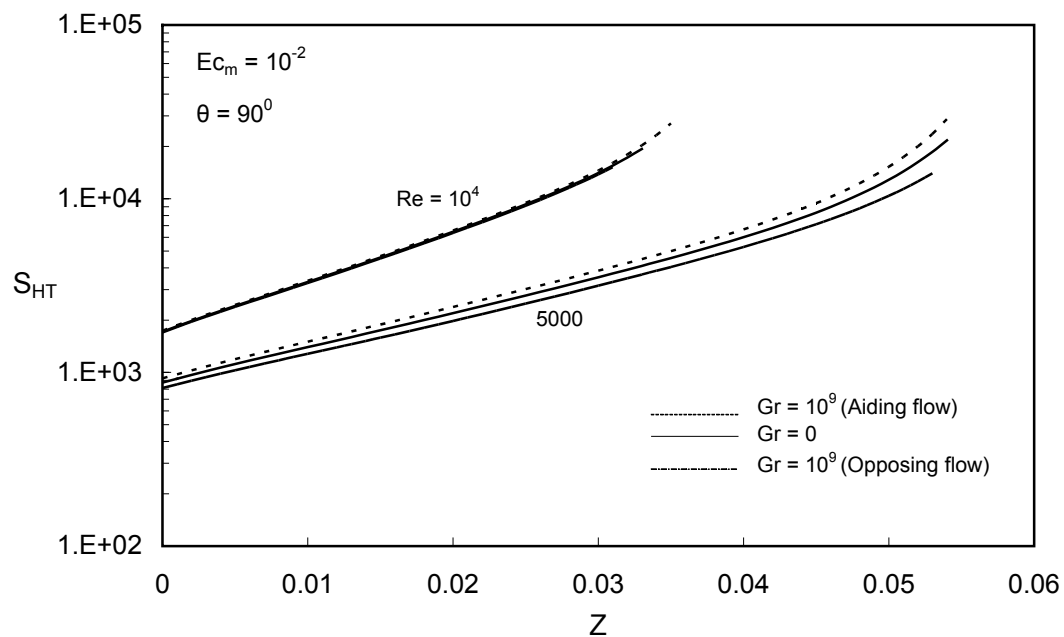


Fig 7-26: Variation of local heat transfer entropy generation for different Reynolds and Grashof numbers

Figure 7.28 shows the variation of local fluid friction entropy generation with radial distance at two selected meridional stations ($\theta = 60^\circ, 105^\circ$). This figure shows that entropy generation due to fluid friction is high on the sphere surface and decreases as we reach the edge of boundary layer, this is because the velocity gradients decrease as we move away from the sphere surface, hence decreasing the entropy generation. As discussed earlier, the aiding free convection causes the meridional and azimuthal velocity components to be higher; the velocity gradients are also higher resulting in an increase in the fluid friction entropy generation. This can be attributed to the higher kinetic energy of the fluid particles away from the sphere surface. Also it can be seen that meridional locations far away from stagnation point have comparatively less fluid friction at the sphere surface. The opposing flow causes the fluid velocity to decrease and hence decreasing the velocity gradients compared with the pure forced convection. It is also clear that the effect of aiding or opposing flow is more pronounced far away from the front stagnation point.

Figure 7.29 shows the variation of total entropy generation and at two meridional stations ($\theta = 60^\circ, 105^\circ$) and a given Reynolds number ($Re = 10^4$). It can be seen that the total entropy generation has the same behavior as the heat transfer entropy generation alone, because the fluid friction is having the magnitude of 10^3 less when compared with heat transfer entropy term and hence has a negligible effect on total entropy generation. It is also clear from the figure 7.25, the aiding flow has the tendency to increase the velocity and temperature gradients by decreasing the thermal boundary layer thickness, and hence increasing the total entropy generation.

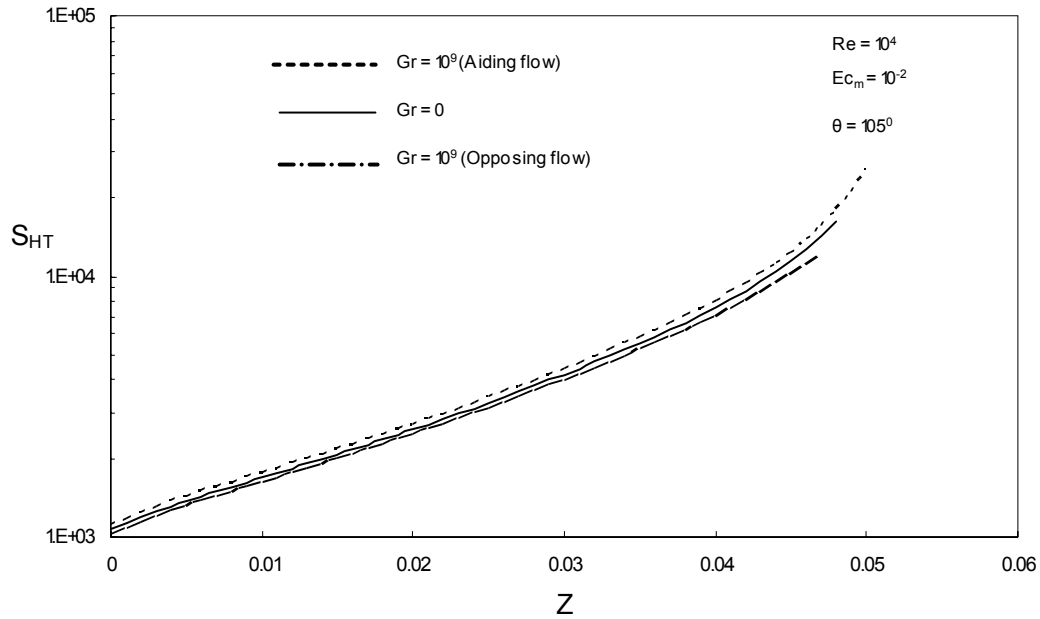


Fig 7-27: Variation of heat transfer entropy generation along radial direction for different Grashof numbers

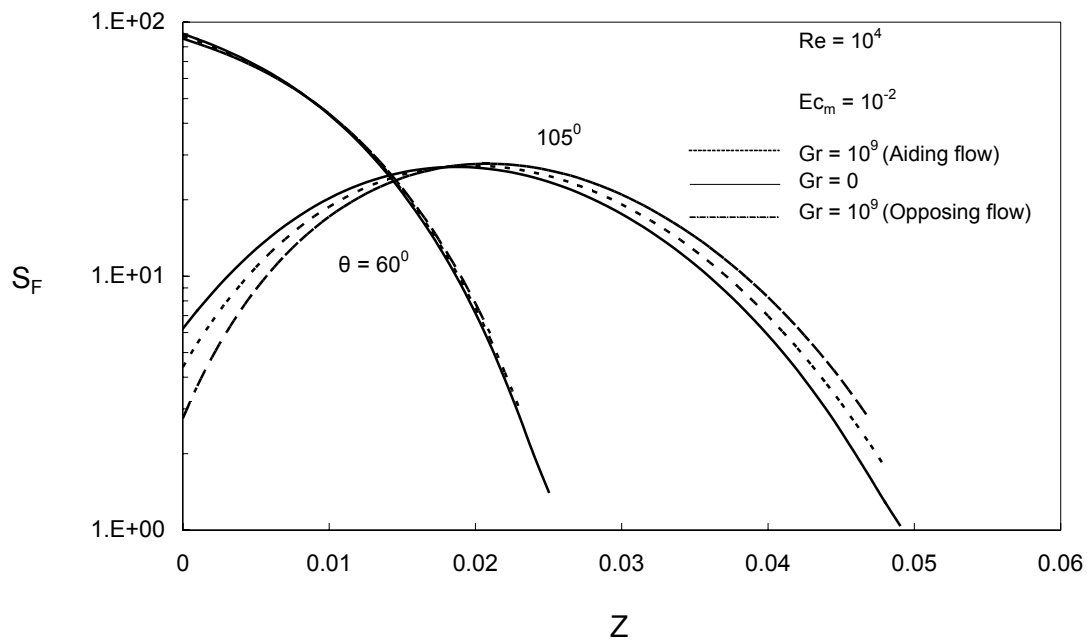


Fig 7-28: Variation of local fluid friction entropy generation at two different meridional stations

The opposing flow (negative Grashof number) decreases the temperature and velocity gradients and hence decreases the total entropy generation.

Figure 7.30 shows the total entropy generation profile along radial direction for different Grashof numbers. Similar to heat transfer entropy profile in figure 7.27, total entropy is also showing that the low Gr number value has less effect on the entropy generation.

Figure 7.31 is a cross plot of the figure 7.29, where total entropy generation is plotted for some selected values of dimensionless radial distance from the wall (Z) for some of the investigated values of Gr. The entropy generation increases as the thermal boundary layer increases from the front stagnation point and again decreases as we move towards the separation point.

Figure 7.32 shows the comparison between entropy generation due to heat transfer and fluid friction. Similar to the case in the previous chapter, the entropy generation due to heat transfer is of very high magnitude in comparison with fluid friction entropy generation, both for aiding free convection and opposing free convection. Hence for most of the practical analysis cases for Uniform heat flux, the fluid friction entropy generation can be neglected.

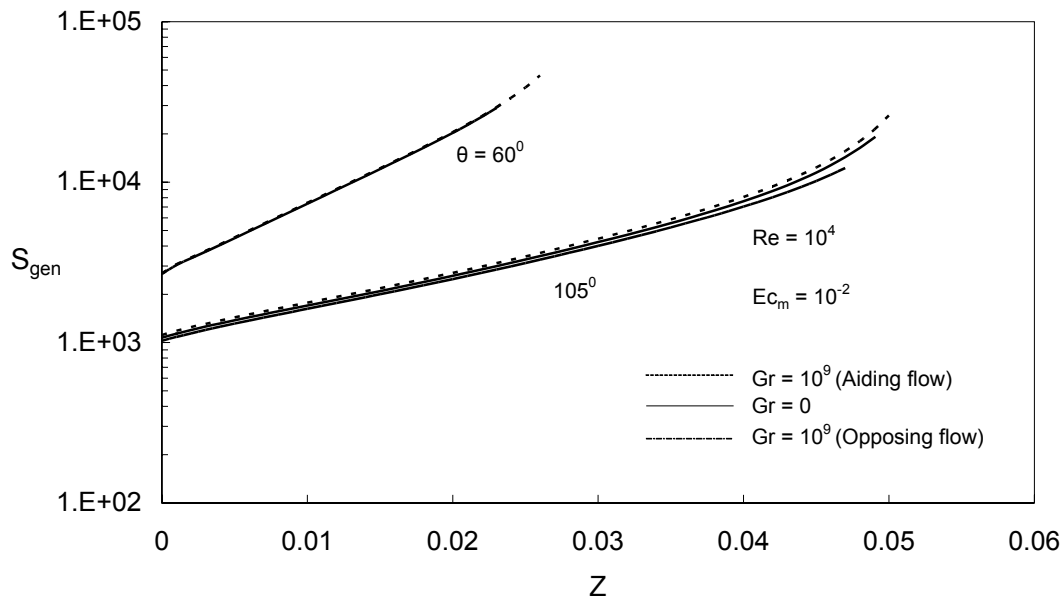


Fig 7-29: Variation of local entropy generation for different Grashof numbers

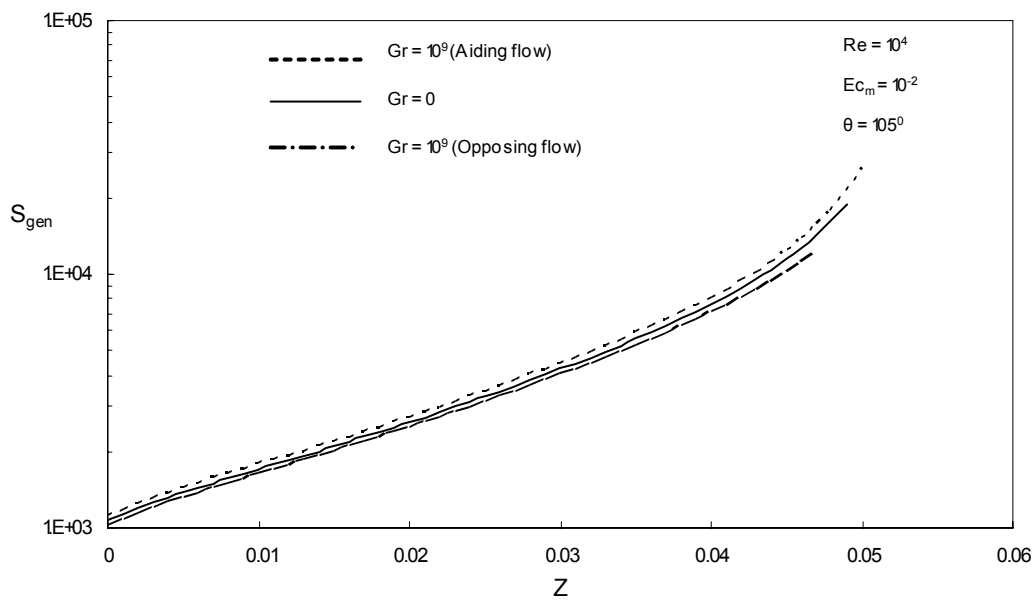


Fig 7-30: Variation of local entropy generation along radial direction for different Grashof numbers

7.3.4: Local and overall average entropy generation profiles:

It can be seen from the Figure 7.33 that higher fluid friction at certain meridional locations over the sphere causes the Fluid friction entropy generation to be considerably high. This is mainly due to fluid particles over the sphere that accelerate in the region $0 \leq \theta \leq 90^\circ$ and decelerate in the region where $\theta > 90^\circ$, hence the pressure decreases in the accelerated region and then increases in the decelerated region. Since the external pressure is imposed at the boundary layer, the transformation of the pressure into kinetic energy takes place in the accelerated region and a great deal of the kinetic energy of the particles adjacent to the wall is consumed to move against the friction forces. This can also be related to the velocity gradients, which are high in accelerating region of flow and less in decelerating region of fluid flow. The heat transfer entropy generation is having a dominant effect in total entropy generation as can be seen from the graph. Moreover, it can be seen that the positive Grashof number, i.e. the aiding flow tends to increase the entropy generation than the opposing flows.

Figure 7.34 shows the local average entropy generation over the sphere surface for different Reynolds number and some selected values of Grashof number. We can notice that at higher Re, entropy generation is higher due to small viscous and thermal boundary layer at higher Reynolds number, which results in higher velocity and temperature gradients and hence higher heat transfer, but at the expense of higher entropy

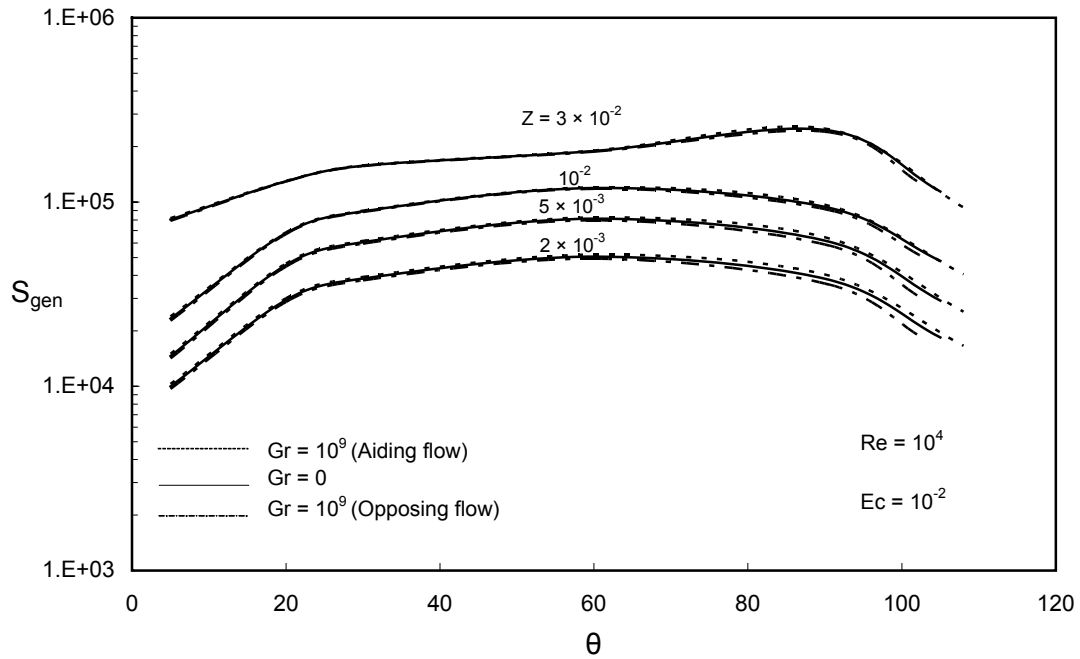


Fig 7-31: Variation of local average entropy generation for different Grashof number

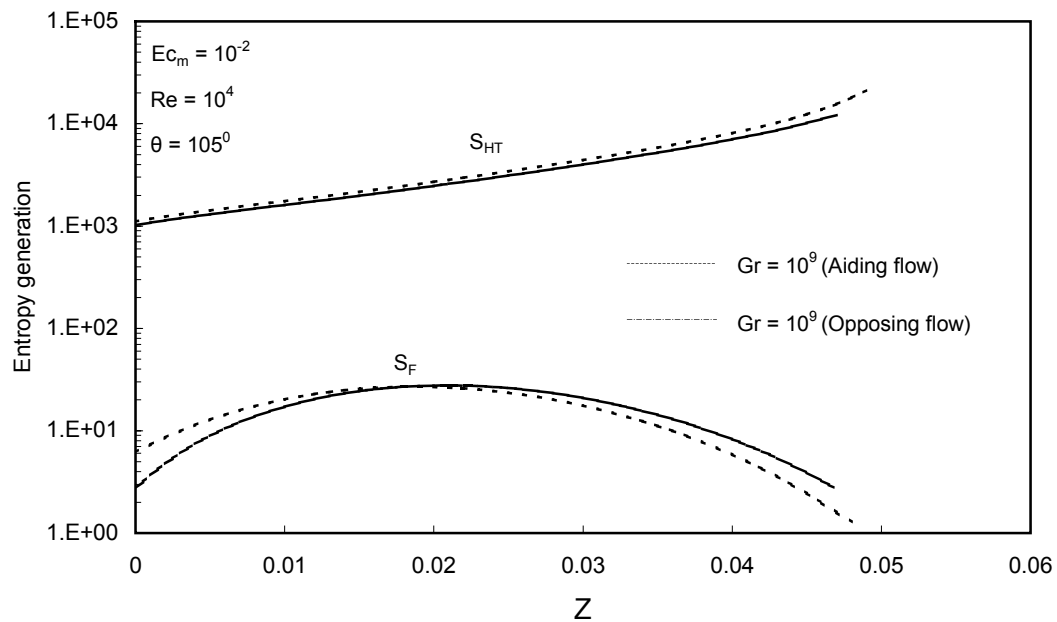


Fig 7-32: Comparing heat transfer and fluid friction entropy generation for different Grashof numbers

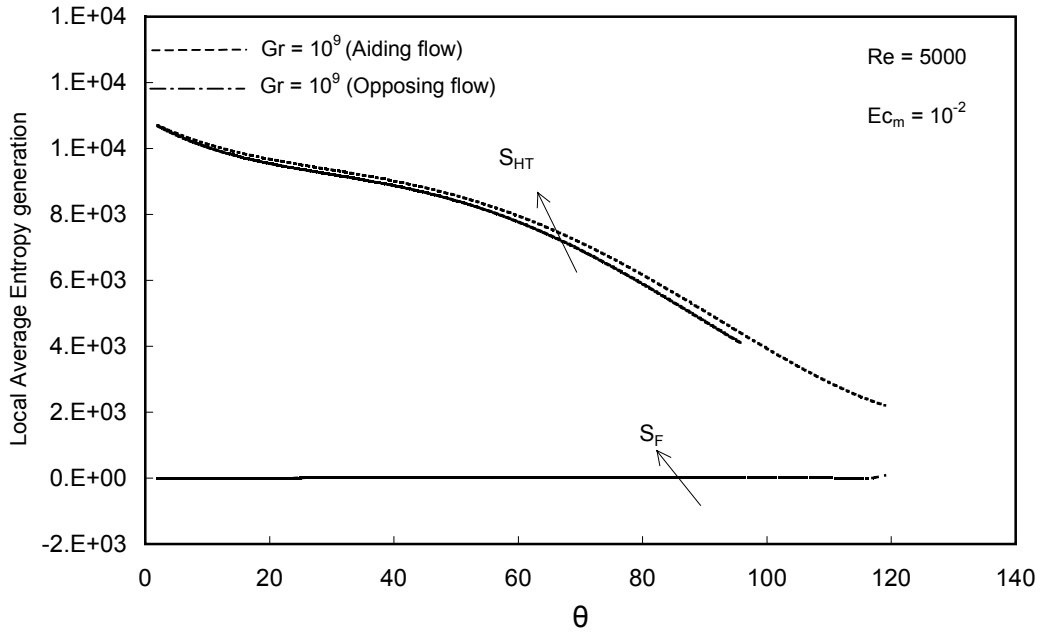


Fig 7-33: Variation of local average entropy generation over the sphere surface for a given Reynolds and Eckert number

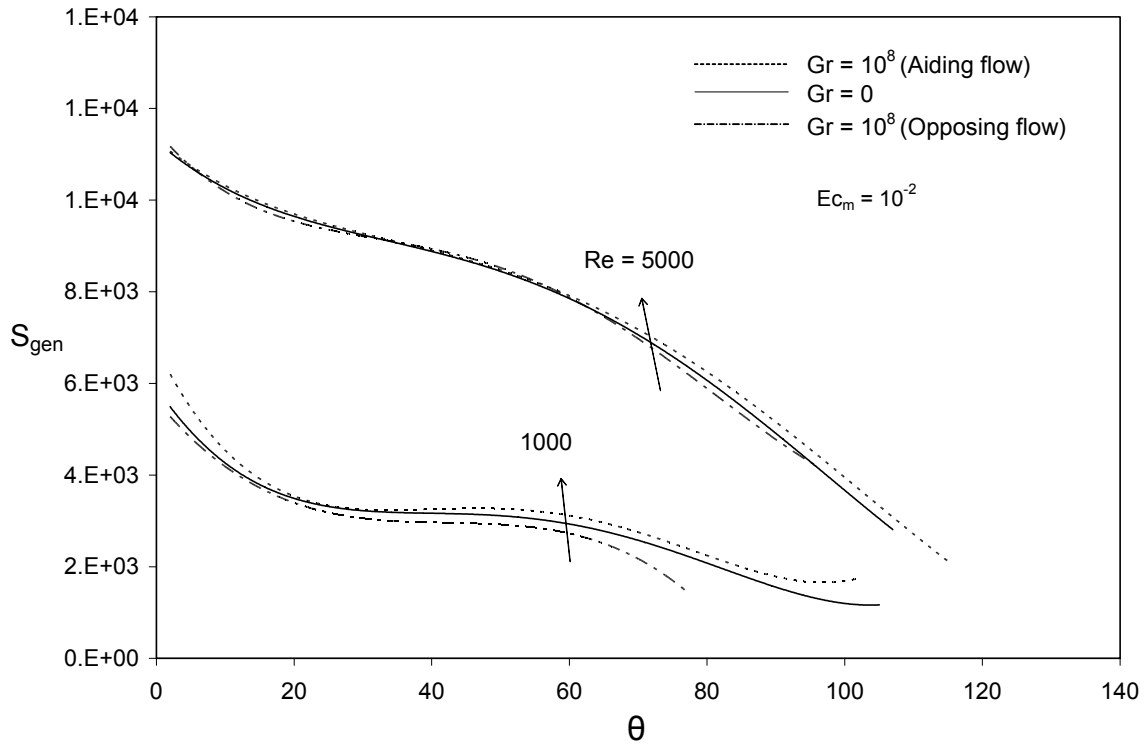


Fig 7-34: Comparing local average entropy generation profile for different Reynolds numbers and Grashof numbers for a given Eckert number

generation. Further more positive Grashof number tends to decrease the thermal boundary layer and increase the temperature and velocity gradients resulting in higher entropy generation.

Figure 7.35 shows the local average entropy generation profile for different Grashof numbers. Similar to the previous graphs the entropy generation along the meridional direction over the sphere is decreasing and lower values of Grashof number has less effect on the entropy generation as compared to the higher values.

Figure 7.36 shows the effect of Reynolds number on total entropy generation for the case of mixed convection for some selected values of Grashof number. As the Reynolds number increases, the Grashof number has minor effect on the flow and temperature fields. This is clear from the graph, which shows that for low Reynolds number, and high Grashof number (aiding or opposing) the Entropy generation change is remarkable and as the Reynolds number increases, the same magnitude of Grashof number has very little effect on the entropy generation change. We can also see that the minimum entropy generation for this case can also be found. Low Reynolds number (<1000) results in less entropy generation and Aiding flow further causes a decrease in entropy generation.

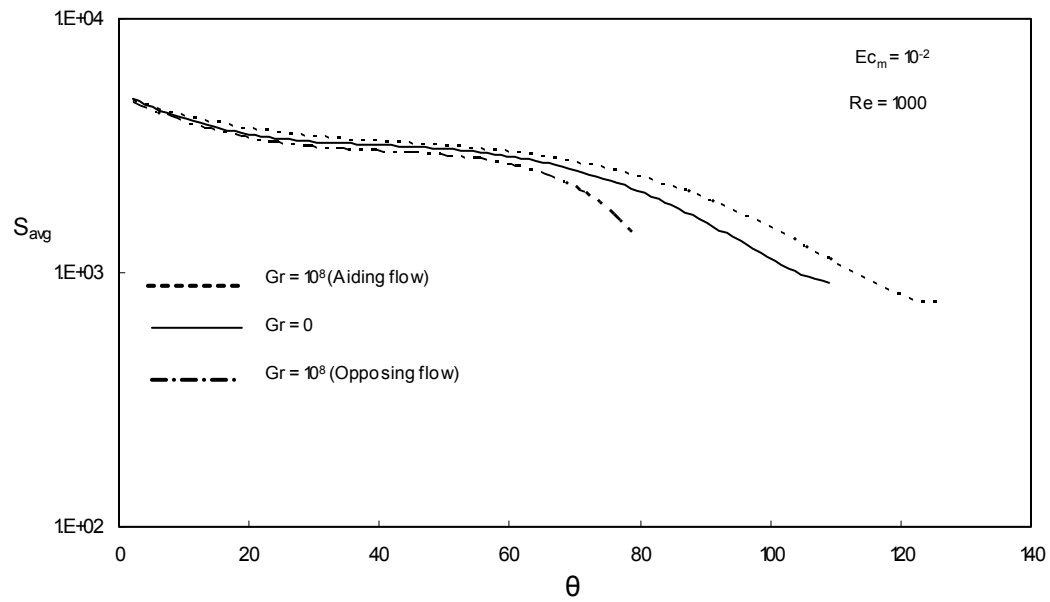


Fig 7-35: Variation of local average entropy generation for different Grashof numbers

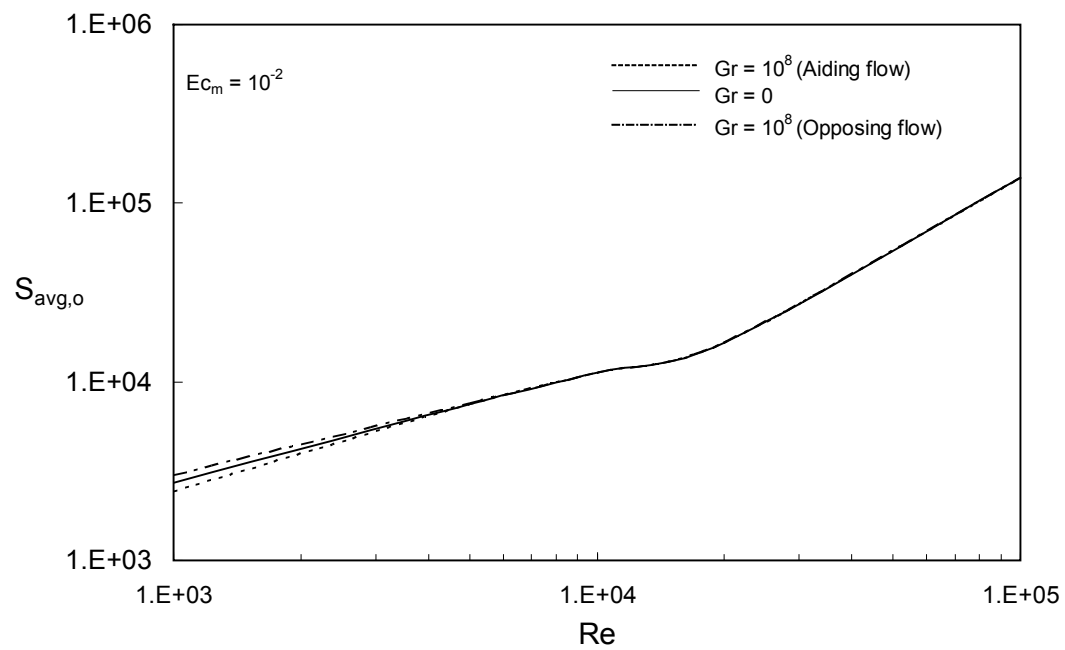


Fig 7-36: Effect of Reynolds number on overall average entropy generation for different Grashof number

7.3.5 Bejan number and Irreversibility Ratio:

Figure 7.37 shows the effect of Reynolds number on Irreversibility ratio for different Grashof number. It can be seen from this figure that as the Reynolds number increases, the irreversibility ratio is continuously increasing, although this increase is of very small in magnitude.

Similarly, figure 7.38 shows the effect of Reynolds number on Bejan number for different Grashof number, it can be seen that as the Reynolds number is increased, Bejan number decreases steadily, although this decrease is of very small magnitude.

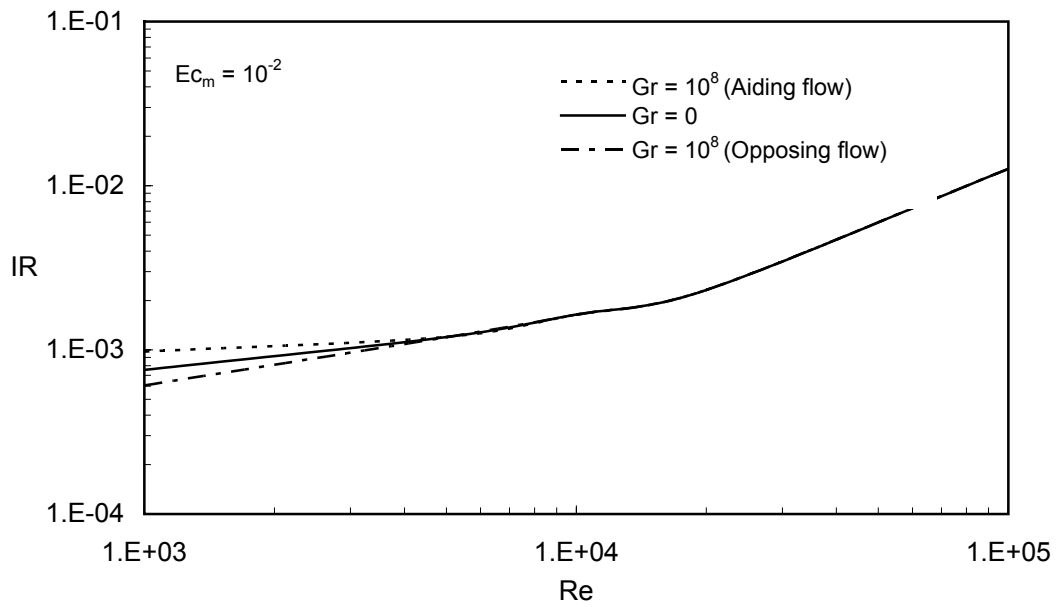


Fig 7-37: Effect of Reynolds number on irreversibility ratio for different Grashof numbers

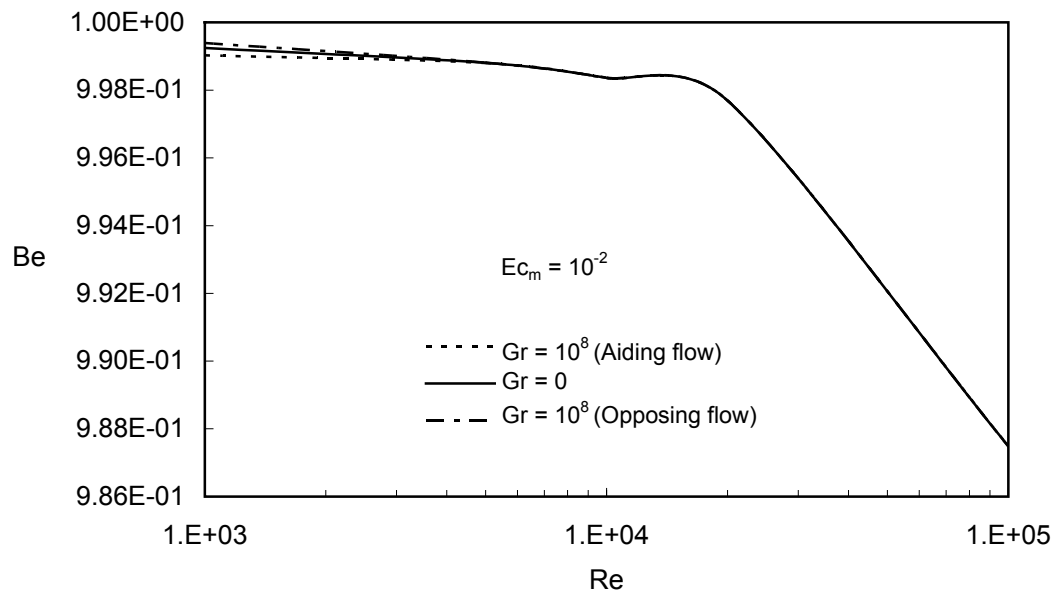


Fig 7-38: Effect of Reynolds number on Bejan number for different Grashof numbers

CHAPTER VIII

CONCLUSIONS AND RECOMMENDATIONS

8.1 Conclusions

A simple, linearized and non-iterative finite difference scheme has been developed and successfully used to solve the boundary layer equations governing the laminar flow around the sphere and the entropy generation was investigated for two boundary conditions, namely Uniform wall temperature and Uniform heat flux. The effect of controlling parameters like Reynolds number (Re), Grashof number (Gr) and Eckert number on the velocity components as well as the temperature within the boundary layer was investigated for both Forced and Mixed Convection. The entropy generation was calculated for both Forced and Mixed Convection and for the two boundary conditions mentioned earlier. In both the cases, the effects of various Controlling parameters like Reynolds number (Re), Grashof number (Gr) and Eckert number on entropy generation was investigated successfully.

From this work, the following conclusions can be drawn:

1. Entropy generation due to fluid friction is not negligible in some cases and has considerable contribution to over all entropy generation in most of the heat transfer processes.
2. For the case of forced convection, the rate of entropy generation was higher at the sphere surface due to high temperature and velocity gradients at the wall.
3. Average fluid friction entropy generation increased with increasing Eckert number for a given Reynolds number in both uniform wall temperature and uniform heat flux cases
4. Average entropy generation for UWT was found to be decreasing with increasing Re until some particular value which was found to be about $Re = 2000$ and then increased and became almost constant with further increase in Reynolds number, hence the minimum entropy generation was obtained for $Re = 2000$. For UHF case, average entropy generation was found to be increasing with increasing Reynolds number, indicating that less the Re, the less is the value of entropy generation.
5. Average entropy generation increases with increasing Eckert number for a given Reynolds number, for both uniform wall temperature and uniform heat flux cases
6. Irreversibility distribution ratio was calculated for each case and the effect of Reynolds number and Eckert number was studied
7. It was found that the irreversibility ratio increased with increasing Eckert number for both UWT and UHF cases

8. Bejan number was found to be decreasing with increasing Eckert number for both UWT and UHF cases, indicating that the fluid friction entropy has considerable contribution to overall entropy generation as Eckert number is increased.
9. For the case of mixed convection, similar trend was observed in the results as for the case of forced convection. Moreover the aiding flow tends to increase the entropy generation due to more heat transfer which is desired phenomena in some of the thermal devices where heat should be removed.
10. Hence aiding flows are desired phenomena in systems where heat transfer is of prime importance and opposing flows are desired where entropy generation is to be kept at the minimum so as to reduce the irreversibility.

8.2 Recommendations for future work

It is recommended that the present work be extended to account for:

1. Flow over multiple spheres.
2. Flow with fluids of different properties.
3. Unsteady flow.
4. Turbulent flow.
5. High temperature and pressure environments.

Appendix

Entropy Generation Equation

A.1 Introduction

In this appendix, the derivation and transformation of entropy generation from spherical coordinates to orthogonal curvilinear coordinates is presented using the assumptions stated in Chapter III. Non-dimensional parameters are then introduced and the equations for the two cases, namely uniform wall temperature and uniform heat flux are derived to the final dimensionless form. An order of magnitude analysis is then carried out and the final entropy generation equations are reached. These equations are then compared with those of full entropy generation equations with out neglecting any term of less magnitude. And a conclusion is reached why we are not using the equations reached after performing order of magnitude analysis and instead using the whole entropy generation equation in our present study.

A.2. Transforming entropy generation equation from spherical to orthogonal curvilinear coordinates:

The entropy generation is a result of both heat transfer and viscous dissipation. Viscous dissipation should be considered for the cases where it is not negligible. Hence in the present study both the heat transfer and viscous entropy generation will be considered. The entropy generation per unit volume as given by Bejan for the case with both heat transfer and viscous dissipation is expressed as:

$$\begin{aligned}
\dot{S}_{gen}''' = & \frac{k}{t^2} \left[\left(\frac{\partial t}{\partial r} \right)^2 + \left(\frac{1}{r} \frac{\partial t}{\partial \theta} \right)^2 + \left(\frac{1}{r \sin \theta} \frac{\partial t}{\partial \phi} \right)^2 \right] \\
& + \frac{\mu}{t} \left\{ \begin{aligned} & 2 \left[\left(\frac{\partial w}{\partial r} \right)^2 + \left(\frac{1}{r} \left(\frac{\partial u}{\partial \theta} \right) + \frac{w}{r} \right)^2 + \left(\frac{w}{r} + \frac{u \cot \theta}{r} \right)^2 \right] \\ & + \left[r \frac{\partial}{\partial r} \left(\frac{u}{r} \right) + \frac{1}{r} \frac{\partial w}{\partial \theta} \right]^2 + \\ & \left[r \frac{\partial}{\partial r} \left(\frac{v}{r} \right) \right]^2 + \left[\frac{\sin \theta}{r} \frac{\partial}{\partial \theta} \left(\frac{v}{\sin \theta} \right) \right]^2 \end{aligned} \right\} \quad (A.1)
\end{aligned}$$

Because of the axisymmetry, $\frac{\partial}{\partial \phi} = 0$ and the velocity in the ϕ direction is also zero,

hence removing these terms in equation (A.1) we get:

$$\begin{aligned}
\dot{S}_{gen}''' = & \frac{k}{t^2} \left[\left(\frac{\partial t}{\partial r} \right)^2 + \left(\frac{1}{r} \frac{\partial t}{\partial \theta} \right)^2 \right] \\
& + \frac{\mu}{t} \left\{ \begin{aligned} & 2 \left[\left(\frac{\partial w}{\partial r} \right)^2 + \left(\frac{1}{r} \left(\frac{\partial u}{\partial \theta} \right) + \frac{w}{r} \right)^2 + \left(\frac{w}{r} + \frac{u \cot \theta}{r} \right)^2 \right] \\ & + \left[r \frac{\partial}{\partial r} \left(\frac{u}{r} \right) + \frac{1}{r} \frac{\partial w}{\partial \theta} \right]^2 \end{aligned} \right\} \quad (A.2)
\end{aligned}$$

Now transforming this equation in to curvilinear coordinate system, we can define the following:

$$\frac{\partial}{\partial \theta} = r \frac{\partial}{\partial x} \quad \text{since } x = r\theta$$

$$\Rightarrow \frac{\partial x}{\partial \theta} = r$$

$$r = a + z \quad \Rightarrow \frac{\partial r}{\partial z} = 1$$

$$\frac{\partial}{\partial r} = \frac{\partial}{\partial z}$$

$$\frac{\partial^2}{\partial r^2} = \frac{\partial}{\partial r} \left(\frac{\partial}{\partial r} \right) = \frac{\partial}{\partial z} \left(\frac{\partial}{\partial r} \right) \frac{\partial z}{\partial r} = \frac{\partial^2}{\partial z^2}$$

Hence the equation (A.2) becomes,

$$\begin{aligned} \Rightarrow \dot{s}_{gen}''' = & \frac{k}{t^2} \left[\left(\frac{\partial t}{\partial z} \right)^2 + \left(\frac{\partial t}{\partial x} \right)^2 \right] \\ & + \frac{\mu}{t} \left\{ 2 \left[\left(\frac{\partial w}{\partial z} \right)^2 + \left(\frac{\partial u}{\partial x} + \frac{w}{a+z} \right)^2 + \left(\frac{w}{a+z} + \frac{u \cot \theta}{a+z} \right)^2 \right] \right. \\ & \left. + \left[(a+z) \frac{\partial}{\partial z} \left(\frac{u}{a+z} \right) + \frac{\partial w}{\partial x} \right]^2 \right\} \end{aligned} \quad (A.3)$$

A.3 Dimensionless form of the equation:

Now non-dimensionalising the above equation by using the following dimensionless parameters:

$$\begin{aligned}
 z = aZ & \qquad \frac{\partial t}{\partial z} = \frac{\partial t}{a\partial Z} \\
 X = \frac{2x}{a \operatorname{Re}} & \qquad \frac{\partial t}{\partial x} = \frac{2}{a \operatorname{Re}} \frac{\partial t}{\partial X} \\
 U = \frac{u}{U_\infty} & \qquad \frac{\partial u}{\partial x} = \frac{2U_\infty}{a \operatorname{Re}} \frac{\partial U}{\partial X} \qquad \frac{\partial w}{\partial x} = \frac{2U_\infty}{a \operatorname{Re}} \frac{\partial W}{\partial X} \\
 w = WU_\infty & \qquad \frac{\partial w}{\partial z} = \frac{U_\infty \partial W}{a\partial Z} \\
 \frac{w}{a+z} = \frac{U_\infty W}{a(1+Z)} & \qquad \frac{u}{a+z} = \frac{U_\infty U}{a(1+Z)}
 \end{aligned} \tag{A.4}$$

Substituting all the terms from (4) in equation (3), we get:

$$\begin{aligned}
 \Rightarrow \dot{s}_{gen} &= \frac{k}{t^2} \left[\left(\frac{\partial t}{a\partial Z} \right)^2 + \left(\frac{2}{a \operatorname{Re}} \frac{\partial t}{\partial X} \right)^2 \right] \\
 &+ \frac{\mu}{t} \left\{ 2 \left[\frac{U_\infty^2}{a^2} \left(\frac{\partial W}{\partial Z} \right)^2 + \left(\frac{2U_\infty}{a \operatorname{Re}} \frac{\partial U}{\partial X} + \frac{U_\infty W}{a(1+Z)} \right)^2 + \left(\frac{U_\infty W}{a(1+Z)} + \frac{U_\infty U \cot \theta}{a(1+Z)} \right)^2 \right] \right. \\
 &\left. + \left[a(1+Z) \frac{1}{a} \frac{\partial}{\partial Z} \left(\frac{U_\infty U}{a(1+Z)} \right) + \frac{2U_\infty}{a \operatorname{Re}} \frac{\partial W}{\partial X} \right]^2 \right\}
 \end{aligned} \tag{A.5}$$

In the above equation, the temperature term, 't' is kept as it is, and it will be later replaced according to the boundary condition. Considering the viscous term alone from here onwards, we have,

$$s_{vis}''' = \frac{\mu}{t} \left\{ \begin{aligned} & 2 \left[\frac{U_\infty^2}{a^2} \left(\frac{\partial W}{\partial Z} \right)^2 + \left(\frac{2U_\infty}{a \operatorname{Re}} \frac{\partial U}{\partial X} + \frac{U_\infty W}{a(1+Z)} \right)^2 + \left(\frac{U_\infty W}{a(1+Z)} + \frac{U_\infty U \cot \theta}{a(1+Z)} \right)^2 \right] \\ & + \left[a(1+Z) \frac{1}{a} \frac{\partial}{\partial Z} \left(\frac{U_\infty U}{a(1+Z)} \right) + \frac{2U_\infty}{a \operatorname{Re}} \frac{\partial W}{\partial X} \right]^2 \end{aligned} \right\} \quad (\text{A.6})$$

taking $\frac{U_\infty^2}{a^2}$ term outside, and expanding the square brackets, we get,

$$\Rightarrow s_{vis}''' = \frac{U_\infty^2}{a^2} \frac{\mu}{t} \left\{ \begin{aligned} & 2 \left[\left(\frac{\partial W}{\partial Z} \right)^2 + \frac{4}{\operatorname{Re}^2} \left(\frac{\partial U}{\partial X} \right)^2 + \frac{W^2}{(1+Z)^2} + \frac{4}{\operatorname{Re}} \left(\frac{\partial U}{\partial X} \right) \frac{W}{(1+Z)} + \frac{W^2}{(1+Z)^2} \right. \\ & \left. + \frac{U^2 \cot^2 \theta}{(1+Z)^2} + \frac{2WU \cot \theta}{(1+Z)^2} \right] \\ & + (1+Z)^2 \left(\frac{\partial}{\partial Z} \left(\frac{U}{(1+Z)} \right) \right)^2 + \frac{4}{\operatorname{Re}^2} \left(\frac{\partial W}{\partial X} \right)^2 + \frac{4}{\operatorname{Re}} \frac{\partial}{\partial Z} \left(\frac{U}{(1+Z)} \right) \left(\frac{\partial W}{\partial X} \right) \end{aligned} \right\}$$

$$\Rightarrow s_{vis}''' = \frac{U_{\infty}^2 \mu}{a^2 t} \left\{ \begin{aligned} & 2 \left[\left(\frac{\partial W}{\partial Z} \right)^2 + \frac{4}{\text{Re}^2} \left(\frac{\partial U}{\partial X} \right)^2 + \frac{W^2}{(1+Z)^2} + \frac{4}{\text{Re}} \left(\frac{\partial U}{\partial X} \right) \frac{W}{(1+Z)} + \frac{W^2}{(1+Z)^2} \right. \\ & \left. + \frac{U^2 \text{Cot}^2 \theta}{(1+Z)^2} + \frac{2WUCot\theta}{(1+Z)^2} \right] \\ & + (1+Z)^2 \left(\frac{\partial U}{\partial Z} \frac{1}{1+Z} - \frac{U}{(1+Z)^2} \right)^2 + \frac{4}{\text{Re}^2} \left(\frac{\partial W}{\partial X} \right)^2 \\ & + \frac{4}{\text{Re}} \left(\frac{\partial U}{\partial Z} \frac{1}{1+Z} - \frac{U}{(1+Z)^2} \right) \left(\frac{\partial W}{\partial X} \right) \end{aligned} \right\}$$

$$\Rightarrow s_{vis}''' = \frac{U_{\infty}^2 \mu}{a^2 t} \left\{ \begin{aligned} & 2 \left[\left(\frac{\partial W}{\partial Z} \right)^2 + \frac{4}{\text{Re}^2} \left(\frac{\partial U}{\partial X} \right)^2 + \frac{W^2}{(1+Z)^2} + \frac{4}{\text{Re}} \left(\frac{\partial U}{\partial X} \right) \frac{W}{(1+Z)} + \frac{W^2}{(1+Z)^2} \right. \\ & \left. + \frac{U^2 \text{Cot}^2 \theta}{(1+Z)^2} + \frac{2WUCot\theta}{(1+Z)^2} \right] \\ & + \left(\left(\frac{\partial U}{\partial Z} \right)^2 + \frac{U^2}{(1+Z)^2} - 2U \frac{\partial U}{\partial Z} \frac{1}{1+Z} \right) + \frac{4}{\text{Re}^2} \left(\frac{\partial W}{\partial X} \right)^2 \\ & + \frac{4}{\text{Re}} \left(\frac{\partial U}{\partial Z} \frac{1}{1+Z} - \frac{U}{(1+Z)^2} \right) \left(\frac{\partial W}{\partial X} \right) \end{aligned} \right\}$$

(A.7)

A.4 Order of magnitude Analysis:

Now performing the order of magnitude analysis using the following terms:

$$\text{Re} \gg 1 \quad , \quad \delta \ll 1$$

$$U = \frac{u}{U_\infty} \approx O(1) \quad , \quad W = \frac{w}{U_\infty} \approx O(\delta)$$

$$Z = \frac{z}{a} \approx O(\delta) \quad , \quad X = \frac{2x}{a \text{Re}} \approx O\left(\frac{1}{\text{Re}}\right)$$

$$\frac{\partial}{\partial X} \approx O(\text{Re}) \quad , \quad \frac{\partial^2}{\partial X^2} \approx O(\text{Re}^2)$$

$$\frac{\partial}{\partial Z} \approx O\left(\frac{1}{\delta}\right) \quad , \quad \frac{\partial^2}{\partial Z^2} \approx O\left(\frac{1}{\delta^2}\right)$$

$$\text{Re} \approx O\left(\frac{1}{\delta^2}\right)$$

equation (A.7) becomes :

$$\Rightarrow s_{vis}''' = \frac{U_\infty^2 \mu}{a^2 t} \left\{ \begin{array}{l} 2 \left[\left(\frac{\partial W}{\partial Z} \right)^2 + \frac{4}{\text{Re}^2} \left(\frac{\partial U}{\partial X} \right)^2 \right] \\ + \left(\frac{\partial U}{\partial Z} \right)^2 + \frac{U^2}{(1+Z)^2} - 2U \frac{\partial U}{\partial Z} \frac{1}{1+Z} \end{array} \right\} \quad (\text{A.8})$$

Hence the resulting volumetric entropy generation equation with heat transfer and viscous terms is given by:

$$s_{gen}^{\bullet} = \frac{k}{t^2} \left[\left(\frac{\partial t}{a \partial Z} \right)^2 + \left(\frac{2}{a \text{Re}} \frac{\partial t}{\partial X} \right)^2 \right] + \frac{U_{\infty}^2 \mu}{a^2 t} \left\{ \begin{array}{l} 2 \left[\left(\frac{\partial W}{\partial Z} \right)^2 + \frac{4}{\text{Re}^2} \left(\frac{\partial U}{\partial X} \right)^2 \right] \\ + \left(\frac{\partial U}{\partial Z} \right)^2 + \frac{U^2}{(1+Z)^2} - 2U \frac{\partial U}{\partial Z} \frac{1}{1+Z} \end{array} \right\} \quad (\text{A.9})$$

In the above order of magnitude analysis of entropy generation equation, the terms in the heat transfer and viscous dissipation having magnitude of the order of δ and less have been neglected.

A.5 Uniform wall temperature case:

$$\text{Consider that } T = \frac{t}{t_w} \quad \text{then} \quad \frac{\partial t}{\partial z} = t_w \frac{\partial T}{\partial z} \quad \text{and} \quad \frac{\partial t}{\partial x} = t_w \frac{\partial T}{\partial x} \quad (\text{A.10})$$

Using the other non-dimensional parameters defined in the equation (4), we get:

$$\frac{\partial t}{\partial z} = \frac{t_w}{a} \frac{\partial T}{\partial Z}, \quad \frac{\partial t}{\partial x} = \frac{2t_w}{a \text{Re}} \frac{\partial T}{\partial X} \quad \text{and} \quad \frac{\partial u}{\partial z} = \frac{U_{\infty}}{a} \frac{\partial U}{\partial Z} \quad (\text{A.11})$$

Substituting into (A.9) we get,

$$\dot{s}_{gen}''' = \frac{k}{T^2 a^2} \left[\left(\frac{\partial T}{\partial Z} \right)^2 + \frac{4}{\text{Re}^2} \left(\frac{\partial T}{\partial X} \right)^2 \right] + \frac{U_\infty^2 \mu}{a^2 t_w T} \left\{ \begin{array}{l} 2 \left[\left(\frac{\partial W}{\partial Z} \right)^2 + \frac{4}{\text{Re}^2} \left(\frac{\partial U}{\partial X} \right)^2 \right] \\ + \left(\frac{\partial U}{\partial Z} \right)^2 + \frac{U^2}{(1+Z)^2} \\ - 2U \frac{\partial U}{\partial Z} \frac{1}{1+Z} \end{array} \right\} \quad (\text{A.12})$$

Now, trying to introduce dimensionless terms in viscous part of the equation (A.12),

$$\dot{s}_{gen}''' = \frac{k}{T^2 a^2} \left[\left(\frac{\partial T}{\partial Z} \right)^2 + \frac{4}{\text{Re}^2} \left(\frac{\partial T}{\partial X} \right)^2 \right] + \frac{\mu C_p k U_\infty^2}{k C_p t_w a^2 T} \left\{ \begin{array}{l} 2 \left[\left(\frac{\partial W}{\partial Z} \right)^2 + \frac{4}{\text{Re}^2} \left(\frac{\partial U}{\partial X} \right)^2 \right] \\ + \left(\frac{\partial U}{\partial Z} \right)^2 + \frac{U^2}{(1+Z)^2} - 2U \frac{\partial U}{\partial Z} \frac{1}{1+Z} \end{array} \right\}$$

taking a^2/k on left hand side of equation, and introducing,

$$Ec_m = \frac{U_\infty^2}{C_p t_w}, \quad \text{Pr} = \frac{\mu C_p}{k}$$

The above entropy generation equation in simplified form is expressed as:

$$\dot{S}_{gen}''' = \dot{s}_{gen}''' \frac{a^2}{k} = \frac{1}{T^2} \left[\left(\frac{\partial T}{\partial Z} \right)^2 + \frac{4}{\text{Re}^2} \left(\frac{\partial T}{\partial X} \right)^2 \right] + \frac{\text{Pr} Ec_m}{T} \left\{ \begin{array}{l} 2 \left[\left(\frac{\partial W}{\partial Z} \right)^2 + \frac{4}{\text{Re}^2} \left(\frac{\partial U}{\partial X} \right)^2 \right] \\ + \left(\frac{\partial U}{\partial Z} \right)^2 + \frac{U^2}{(1+Z)^2} \\ - 2U \frac{\partial U}{\partial Z} \frac{1}{1+Z} \end{array} \right\} \quad (\text{A.13})$$

where Ec_m is modified Eckert number as given by **Haddad et al [26]** .

A.6 Uniform heat flux case:

Considering again equation (A.9), we have,

$$\dot{S}_{gen}''' = \frac{k}{t^2} \left[\left(\frac{\partial t}{a \partial Z} \right)^2 + \left(\frac{2}{a \text{Re}} \frac{\partial t}{\partial X} \right)^2 \right] + \frac{U_\infty^2 \mu}{a^2 t} \left\{ \begin{array}{l} 2 \left[\left(\frac{\partial W}{\partial Z} \right)^2 + \frac{4}{\text{Re}^2} \left(\frac{\partial U}{\partial X} \right)^2 \right] \\ + \left(\frac{\partial U}{\partial Z} \right)^2 + \frac{U^2}{(1+Z)^2} - 2U \frac{\partial U}{\partial Z} \frac{1}{1+Z} \end{array} \right\}$$

Using the dimensionless temperature for uniform heat flux case,

$$T = \frac{kt}{aq}, \quad \text{i.e.} \quad t = \frac{aqT}{k},$$

equation (A.9) can be rewritten as

$$\dot{S}_{gen}''' = \frac{k}{a^2 T^2} \left[\left(\frac{\partial T}{\partial Z} \right)^2 + \left(\frac{4}{\text{Re}^2} \frac{\partial T}{\partial X} \right)^2 \right] + \frac{\mu k U_\infty^2}{T a^3 q} \left\{ \begin{array}{l} 2 \left[\left(\frac{\partial W}{\partial Z} \right)^2 + \frac{4}{\text{Re}^2} \left(\frac{\partial U}{\partial X} \right)^2 \right] \\ + \left(\frac{\partial U}{\partial Z} \right)^2 + \frac{U^2}{(1+Z)^2} - 2U \frac{\partial U}{\partial Z} \frac{1}{1+Z} \end{array} \right\}$$

Hence, the entropy generation equation per unit volume upon solving and introducing the dimensionless term as earlier will give:

$$\dot{S}_{gen}''' = \dot{S}_{gen}''' \frac{a^2}{k} = \frac{1}{T^2} \left[\left(\frac{\partial T}{\partial Z} \right)^2 + \frac{4}{\text{Re}^2} \left(\frac{\partial T}{\partial X} \right)^2 \right] + \frac{\text{Pr} E c_m T_w}{T} \left\{ \begin{array}{l} 2 \left[\left(\frac{\partial W}{\partial Z} \right)^2 + \frac{4}{\text{Re}^2} \left(\frac{\partial U}{\partial X} \right)^2 \right] \\ + \left(\frac{\partial U}{\partial Z} \right)^2 + \frac{U^2}{(1+Z)^2} \\ - 2U \frac{\partial U}{\partial Z} \frac{1}{1+Z} \end{array} \right\} \quad (\text{A.14})$$

This as a result of selection of dimensionless parameters is similar to equation (A.13).

A.7. Writing the above entropy equation in finite difference form:

$$\begin{aligned}
 \frac{\partial U}{\partial X} &= \frac{U_{i,j+1} - U_{i,j}}{\Delta X_i} & ; & & U = U_{i,j} \\
 \frac{\partial U}{\partial Z} &= \frac{U_{i,j+1} - U_{i-1,j+1}}{\Delta Z} & ; & & \frac{U}{1+Z} = \frac{U_{i,j}}{1+Z_i} \\
 \frac{\partial W}{\partial X} &= \frac{W_{i,j+1} - W_{i,j}}{\Delta X_i} & ; & & W = W_{i,j} \\
 \frac{\partial W}{\partial Z} &= \frac{W_{i+1,j+1} - W_{i,j+1}}{\Delta Z} & ; & & \\
 \frac{\partial T}{\partial X} &= \frac{T_{i,j+1} - T_{i,j}}{\Delta X_i} & ; & & \frac{\partial T}{\partial Z} = \frac{T_{i+1,j+1} - T_{i,j+1}}{\Delta Z}
 \end{aligned}
 \tag{A.15}$$

The simplified entropy generation equation (A.13) now can be written as:

$$\dot{S}_{gen}''' = \frac{1}{T^2} \left[\left(\frac{\partial T}{\partial Z} \right)^2 + \frac{4}{\text{Re}^2} \left(\frac{\partial T}{\partial X} \right)^2 \right] + \frac{\text{Pr} Ec_m}{T} \left\{ 2 \left[\left(\frac{\partial W}{\partial Z} \right)^2 + \frac{4}{\text{Re}^2} \left(\frac{\partial U}{\partial X} \right)^2 \right] + \left(\frac{\partial U}{\partial Z} \right)^2 + \frac{U^2}{(1+Z)^2} - 2U \frac{\partial U}{\partial Z} \frac{1}{1+Z} \right\}$$

$$\begin{aligned}
\dot{S}_{gen}''' = & \frac{1}{T_{i,j}^2} \left[\left(\frac{T_{i+1,j+1} - T_{i,j+1}}{\Delta Z} \right)^2 + \frac{4}{\text{Re}^2} \left(\frac{T_{i,j+1} - T_{i,j}}{\Delta X_i} \right)^2 \right] \\
& + \frac{\text{Pr}Ec_m}{T_{i,j}} \left\{ \begin{aligned} & 2 \left[\left(\frac{W_{i+1,j+1} - W_{i,j+1}}{\Delta Z} \right)^2 + \frac{4}{\text{Re}^2} \left(\frac{U_{i,j+1} - U_{i,j}}{\Delta X_i} \right)^2 \right] \\ & + \left(\frac{U_{i,j+1} - U_{i-1,j+1}}{\Delta Z} \right)^2 + \frac{U_{i,j}^2}{(1+Z_i)^2} \\ & - 2U_{i,j} \left(\frac{U_{i,j+1} - U_{i-1,j+1}}{\Delta Z} \right) \frac{1}{1+Z_i} \end{aligned} \right\} \quad (\text{A.16})
\end{aligned}$$

Similarly the entropy generation equation (A.14) for the constant heat flux case can be written as:

$$\begin{aligned}
\dot{S}_{gen}''' = & \frac{1}{T_{i,j}^2} \left[\left(\frac{T_{i+1,j+1} - T_{i,j+1}}{\Delta Z} \right)^2 + \frac{4}{\text{Re}^2} \left(\frac{T_{i,j+1} - T_{i,j}}{\Delta X_i} \right)^2 \right] \\
& + \frac{\text{Pr}Ec_m T_{wi,j}}{T_{i,j}} \left\{ \begin{aligned} & 2 \left[\left(\frac{W_{i+1,j+1} - W_{i,j+1}}{\Delta Z} \right)^2 + \frac{4}{\text{Re}^2} \left(\frac{U_{i,j+1} - U_{i,j}}{\Delta X_i} \right)^2 \right] \\ & + \left(\frac{U_{i,j+1} - U_{i-1,j+1}}{\Delta Z} \right)^2 + \frac{U_{i,j}^2}{(1+Z_i)^2} \\ & - 2U_{i,j} \left(\frac{U_{i,j+1} - U_{i-1,j+1}}{\Delta Z} \right) \frac{1}{1+Z_i} \end{aligned} \right\} \quad (\text{A.17})
\end{aligned}$$

A.8. The entropy equation with out performing order of magnitude analysis:

In order to see the complete effect of all the velocity and temperature gradients, it is interesting to include all the terms with out performing order of magnitude analysis. In this section, the whole un-simplified entropy generation equation is compared with the simplified equation obtained in section A.7.

The entropy equation with out performing order of magnitude analysis is given by:

$$\Rightarrow \dot{S}_{gen}''' = \frac{1}{T^2} \left[\left(\frac{\partial T}{\partial Z} \right)^2 + \frac{4}{\text{Re}^2} \left(\frac{\partial T}{\partial X} \right)^2 \right] + \left\{ \begin{array}{l} 2 \left[\left(\frac{\partial W}{\partial Z} \right)^2 + \frac{4}{\text{Re}^2} \left(\frac{\partial U}{\partial X} \right)^2 + \frac{W^2}{(1+Z)^2} + \frac{4}{\text{Re}} \left(\frac{\partial U}{\partial X} \right) \frac{W}{(1+Z)} + \frac{W^2}{(1+Z)^2} \right. \\ \left. + \frac{U^2 \text{Cot}^2 \theta}{(1+Z)^2} + \frac{2WUCot\theta}{(1+Z)^2} \right] \\ \frac{U_\infty^2 \mu}{a^2 t} \left\{ \left(\frac{\partial U}{\partial Z} \right)^2 + \frac{U^2}{(1+Z)^2} - 2U \frac{\partial U}{\partial Z} \frac{1}{1+Z} \right\} + \frac{4}{\text{Re}^2} \left(\frac{\partial W}{\partial X} \right)^2 \\ \left. + \frac{4}{\text{Re}} \left(\frac{\partial U}{\partial Z} \frac{1}{1+Z} - \frac{U}{(1+Z)^2} \right) \left(\frac{\partial W}{\partial X} \right) \right\} \end{array} \right.$$

this equation for uniform wall temperature case can be given as

$$\Rightarrow \dot{S}_{gen}''' = \frac{1}{T^2} \left[\left(\frac{\partial T}{\partial Z} \right)^2 + \frac{4}{\text{Re}^2} \left(\frac{\partial T}{\partial X} \right)^2 \right] +$$

$$\left. \begin{aligned} & 2 \left[\left(\frac{\partial W}{\partial Z} \right)^2 + \frac{4}{\text{Re}^2} \left(\frac{\partial U}{\partial X} \right)^2 + \frac{W^2}{(1+Z)^2} + \frac{4}{\text{Re}} \left(\frac{\partial U}{\partial X} \right) \frac{W}{(1+Z)} + \frac{W^2}{(1+Z)^2} \right. \\ & \left. + \frac{U^2 \text{Cot}^2 \theta}{(1+Z)^2} + \frac{2WUCot\theta}{(1+Z)^2} \right] \\ & \frac{\text{Pr}Ec_m}{T} \left\{ + \left(\left(\frac{\partial U}{\partial Z} \right)^2 + \frac{U^2}{(1+Z)^2} - 2U \frac{\partial U}{\partial Z} \frac{1}{1+Z} \right) + \frac{4}{\text{Re}^2} \left(\frac{\partial W}{\partial X} \right)^2 \right. \\ & \left. + \frac{4}{\text{Re}} \left(\frac{\partial U}{\partial Z} \frac{1}{1+Z} - \frac{U}{(1+Z)^2} \right) \left(\frac{\partial W}{\partial X} \right) \right\} \end{aligned} \right]$$

writing the above equation in finite difference form using the terms in equation (A.15) we get:

$$\begin{aligned}
\dot{S}_{gen}^m &= \frac{1}{T_{i,j}^2} \left[\left(\frac{T_{i+1,j+1} - T_{i,j+1}}{\Delta Z} \right)^2 + \frac{4}{\text{Re}^2} \left(\frac{T_{i,j+1} - T_{i,j}}{\Delta X_i} \right)^2 \right] \\
&+ \frac{\text{Pr} Ec_m}{T_{i,j}} \left\{ \begin{aligned}
&\left[\left(\frac{W_{i+1,j+1} - W_{i,j+1}}{\Delta Z} \right)^2 + \frac{4}{\text{Re}^2} \left(\frac{U_{i,j+1} - U_{i,j}}{\Delta X_i} \right)^2 + \frac{2W_{i,j}^2}{(1+Z_{i,j})^2} \right. \\
&+ \frac{4}{\text{Re}} \left(\frac{U_{i,j+1} - U_{i,j}}{\Delta X_i} \right) \frac{W_{i,j}}{(1+Z_{i,j})} \\
&+ \frac{U_{i,j}^2 \text{Cot}^2(J\Delta\theta)}{(1+Z_{i,j})^2} + \frac{2W_{i,j}U_{i,j} \text{Cot}(J\Delta\theta)}{(1+Z_{i,j})^2} \\
&\left. + \left(\frac{U_{i,j+1} - U_{i-1,j+1}}{\Delta Z} \right)^2 + \frac{U_{i,j}^2}{(1+Z_{i,j})^2} \right. \\
&- 2U_{i,j} \left(\frac{U_{i,j+1} - U_{i-1,j+1}}{\Delta Z} \right) \frac{1}{1+Z_{i,j}} + \frac{4}{\text{Re}^2} \left(\frac{W_{i,j+1} - W_{i,j}}{\Delta X_i} \right)^2 \\
&\left. + \frac{4}{\text{Re}} \left(\left(\frac{U_{i,j+1} - U_{i-1,j+1}}{\Delta Z} \right) \frac{1}{1+Z_{i,j}} - \frac{U_{i,j}}{(1+Z_{i,j})^2} \right) \left(\frac{W_{i,j+1} - W_{i,j}}{\Delta X_i} \right) \right\}
\end{aligned} \right. \tag{A.18}
\end{aligned}$$

similarly we can write for uniform heat flux case in non-dimensional form as:

$$\Rightarrow \dot{S}_{gen}''' = \frac{1}{T^2} \left[\left(\frac{\partial T}{\partial Z} \right)^2 + \frac{4}{\text{Re}^2} \left(\frac{\partial T}{\partial X} \right)^2 \right]$$

$$+ \frac{\text{Pr} Ec_m T_w}{T} \left\{ \begin{aligned} & 2 \left[\left(\frac{\partial W}{\partial Z} \right)^2 + \frac{4}{\text{Re}^2} \left(\frac{\partial U}{\partial X} \right)^2 + \frac{W^2}{(1+Z)^2} + \frac{4}{\text{Re}} \left(\frac{\partial U}{\partial X} \right) \frac{W}{(1+Z)} + \frac{W^2}{(1+Z)^2} \right. \\ & \left. + \frac{U^2 \text{Cot}^2 \theta}{(1+Z)^2} + \frac{2WUC \text{ot} \theta}{(1+Z)^2} \right] \\ & + \left(\left(\frac{\partial U}{\partial Z} \right)^2 + \frac{U^2}{(1+Z)^2} - 2U \frac{\partial U}{\partial Z} \frac{1}{1+Z} \right) + \frac{4}{\text{Re}^2} \left(\frac{\partial W}{\partial X} \right)^2 \\ & + \frac{4}{\text{Re}} \left(\frac{\partial U}{\partial Z} \frac{1}{1+Z} - \frac{U}{(1+Z)^2} \right) \left(\frac{\partial W}{\partial X} \right) \end{aligned} \right\}$$

In finite difference form the above equation can be written as:

$$\begin{aligned}
\dot{S}_{gen}''' = & \frac{1}{T_{i,j}^2} \left[\left(\frac{T_{i+1,j+1} - T_{i,j+1}}{\Delta Z} \right)^2 + \frac{4}{\text{Re}^2} \left(\frac{T_{i,j+1} - T_{i,j}}{\Delta X_i} \right)^2 \right] \\
& + \frac{\text{Pr} Ec_m T_{wi,j}}{T_{i,j}} \left\{ \left[\left(\frac{W_{i+1,j+1} - W_{i,j+1}}{\Delta Z} \right)^2 + \frac{4}{\text{Re}^2} \left(\frac{U_{i,j+1} - U_{i,j}}{\Delta X_i} \right)^2 + \frac{2W_{i,j}^2}{(1+Z_{i,j})^2} \right. \right. \\
& \left. \left. + \frac{4}{\text{Re}} \left(\frac{U_{i,j+1} - U_{i,j}}{\Delta X_i} \right) \frac{W_{i,j}}{(1+Z_{i,j})} \right. \right. \\
& \left. \left. + \frac{U_{i,j}^2 \text{Cot}^2(J\Delta\theta)}{(1+Z_{i,j})^2} + \frac{2W_{i,j}U_{i,j} \text{Cot}(J\Delta\theta)}{(1+Z_{i,j})^2} \right] \right. \\
& \left. + \left(\frac{U_{i,j+1} - U_{i-1,j+1}}{\Delta Z} \right)^2 + \frac{U_{i,j}^2}{(1+Z_{i,j})^2} \right. \\
& \left. - 2U_{i,j} \left(\frac{U_{i,j+1} - U_{i-1,j+1}}{\Delta Z} \right) \frac{1}{1+Z_{i,j}} + \frac{4}{\text{Re}^2} \left(\frac{W_{i,j+1} - W_{i,j}}{\Delta X_i} \right)^2 \right. \\
& \left. + \frac{4}{\text{Re}} \left(\left(\frac{U_{i,j+1} - U_{i-1,j+1}}{\Delta Z} \right) \frac{1}{1+Z_{i,j}} - \frac{U_{i,j}}{(1+Z_{i,j})^2} \right) \left(\frac{W_{i,j+1} - W_{i,j}}{\Delta X_i} \right) \right\} \quad (\text{A.19})
\end{aligned}$$

The table which shows the comparison between the simplified and un-simplified entropy generation equations for $\text{Re} = 10^4$ are given in table A-1. As seen from the table, the percentage variation at some nodes is quite high, so the use of simplified equation is not justified. Hence in this study the whole entropy generation equation without simplifying is used.

Table A-1: Comparing Simplified and Un-Simplified entropy generation equation:

With out Order of Magnitude Analysis (OMA)				With OMA					
30 DEG		60 DEG		30 DEG		60 DEG		% variation for $\theta=30^{\circ}$	% variation for $\theta=60^{\circ}$
Z	S _{GEN}	Z	S _{GEN}	Z	S _{GEN}	Z	S _{GEN}		
0	38881.01	0	51488.63	0	38881.01	0	51488.63	0	0
0.001	46684.28	0.001	62510.7	0.001	46684.27	0.001	62510.7	2.142E-05	0
0.002	54092.21	0.002	72920.88	0.002	54092.18	0.002	72920.88	5.546E-05	0
0.003	61085.87	0.003	82715.11	0.003	61085.79	0.003	82715.09	0.000131	2.418E-05
0.004	67664.85	0.004	91923.89	0.004	67664.7	0.004	91923.85	0.0002217	4.351E-05
0.005	73838.54	0.005	100599	0.005	73838.28	0.005	100598.9	0.0003521	9.94E-05
0.006	79621.91	0.006	108806.8	0.006	79621.47	0.006	108806.6	0.0005526	0.0001838
0.007	85033.24	0.007	116627.1	0.007	85032.49	0.007	116626.8	0.000882	0.0002572
0.008	90092.48	0.008	124152	0.008	90091.25	0.008	124151.5	0.0013653	0.0004027
0.009	94820.79	0.009	131485.5	0.009	94818.8	0.009	131484.5	0.0020987	0.0007605
0.01	99239.64	0.01	138742.6	0.01	99236.46	0.01	138741	0.0032044	0.0011532
0.011	103370.4	0.011	146047.1	0.011	103365.4	0.011	146044.3	0.004837	0.0019172
0.012	107234.4	0.012	153526	0.012	107226.5	0.012	153521	0.007367	0.0032568
0.013	110852.8	0.013	161300.4	0.013	110840.4	0.013	161291.9	0.011186	0.0052697
0.014	114247.4	0.014	169472.7	0.014	114227.9	0.014	169458.1	0.0170682	0.008615
0.015	117441.5	0.015	178106.3	0.015	117411.1	0.015	178081.4	0.0258852	0.0139804
0.016	120462.6	0.016	187201.9	0.016	120415.3	0.016	187159.4	0.0392653	0.0227028
0.017	123346	0.017	196666.8	0.017	123272.3	0.017	196594.3	0.0597506	0.0368644
0.018	126140.4	0.018	206282.2	0.018	126025.5	0.018	206158.7	0.091089	0.0598694
0.019	128917.4	0.019	215674.6	0.019	128738.1	0.019	215464.7	0.1390813	0.0973225
0.02	131786.3	0.02	224305.6	0.02	131505.9	0.02	223948.9	0.2127687	0.1590241
0.021	134917.4	0.021	231491.7	0.021	134478.2	0.021	230885.6	0.3255325	0.2618236
0.022	138580.8	0.022	236503.7	0.022	137890.7	0.022	235473.9	0.4979766	0.4354266
0.023	143208	0.023	238805.4	0.023	142120.3	0.023	2.37E+05	0.7595246	0.732898
0.024	149495.4	0.024	238557	0.024	147774.5	0.024	2.36E+05	1.1511391	1.2475425
0.025	158574.6	0.025	237550.4	0.025	155841.2	0.025	2.32E+05	1.7237313	2.1320107
0.026	172297.7	0.026	241002.6	0.026	167937.5	0.026	2.32E+05	2.53062	3.5797124
0.027	193715.8	0.027	260747.8	0.027	186729	0.027	246034.2	3.606727	5.6428472
0.028	227890.2	0.028	320990	0.028	216640.3	0.028	295861.2	4.936544	7.8285305
0.029	283283.3	0.029	468536	0.029	265075.4	0.029	425550.9	6.4274527	9.1743431
0.03	374177.2	0.03	790963.6	0.03	344542.5	0.03	717298	7.9199641	9.3133995
0.031	525004.9	0.031	1449159	0.031	476460.9	0.031	1322632	9.2463899	8.731064
0.032	778526.9	0.032	2736794	0.032	698364.5	0.032	2518801	10.296677	7.9652689

References

1. Jia H., Gogos G.: "Laminar isothermal convection heat transfer from isothermal spheres"; *Int.J.Heat and mass transfer*, Vol 39, N8, pp 1603-1615, 1996.
2. Nazar R., Amin N., Pop I.: "On the mixed Convection boundary layer flow about a solid sphere with constant surface temperature"; *The Arabian journal for Science and Engineering*"; Vol 27, N 2C, pp 117-135, 2002.
3. Pruppacher H.R., Le Clair B.P; and Hamielec A.E.: "Some relations between drag and flow pattern of viscous flow past a sphere and cylinder at low and intermediate Reynolds numbers"; *Journal of Fluid Mechanics*, Vol: 44, part 4, pp 781-790, 1970.
4. El-Bedeawi S.A.: "The boundary layer flow on a rotating body"; *Ph.D. Thesis* Mechanical Engineering Department, Al-Azhar University, Cairo, Egypt, 1985.
5. El-Shaarawi M.A.I., El-Rafaie M.F. and El-Bedeawi S.A.: "Numerical Solution of laminar boundary layer flow about a rotating sphere in an axial stream"; *Journal of fluid mechanics*, Vol: 107, pp 97-104, 1985
6. El-Shaarawi M.A.I., Ahmad N.T., and Kodah Z.: "Mixed convection about a rotating sphere in an axial stream"; *Numerical heat transfer, Part A*, Vol 18, 1990, pp 71-93
7. Lepalec G.L. and Daguinet M.: "Laminar three dimensional mixed convection about a rotating sphere in a stream"; *Int. J. Heat and Mass Transfer*, Vol: 30, No: 7, pp 1511-1523, 1987.

8. Lepalec G.L. and Dagenet M.: "Mixed convection about a sphere rotating in a forced axial flow"; *Int. Chemical Engineering*, Vol: 30, No: 4, pp 683-690, 1990.
9. Yuge T.: "Experiments on heat transfer from spheres including combined natural and forced convection", *J. Heat transfer*, Vol: 82, pp 214-220, 1960.
10. Chen T.S. and Mucoglu A.: "Analysis of mixed forced and free convection about a sphere"; *Int.J.Heat Mass Transfer*, Vol: 20, pp 867-875, 1977.
11. Chen T.S. and Mucoglu A.: "Mixed convection about a sphere with uniform surface heat flux"; *J. Heat Transfer*, Vol: 100, pp 542-544, 1978.
12. Tang L. and Johnson A.T.: "Flow visualization of mixed convection about a sphere"; *Int.Comm.Heat Mass Transfer*, Vol: 17, pp 67-77, 1990.
13. Antar M., El-Shaarawi M.: "Mixed convection around a sphere in an air stream"; *Heat and mass transfer*, Vol 38, 2002 , pp 419-422.
14. Alassar R.S. and Badr H.M.: "Oscillating viscous flow over a sphere"; *Computers and fluids*, Vol: 26, N 7 , pp 661-682, 1997.
15. Bejan A.: "Study of entropy generation in fundamental convective heat transfer"; *Journal of heat transfer*; Vol: 101, pp 718-725, November-1979.
16. Shohel M., Roydon A. F.: "The second law analysis in fundamental convective heat transfer problems"; *International journal of thermal sciences*, V42, pp177-186, 2003
17. Haddad O.M., Alkam M.K., Khasawneh M.T.: "Entropy generation due to laminar forced convection in the entrance region of a concentric annulus"; *Energy*, V29, 2004, pp 35-55

18. Hassen Abbassi, Mourad Magherbi, Ammar Ben Brahim: "Entropy generation in Poiseuille-Benard channel flow"; *International journal of Thermal Sciences*, V42, 2003, pp 1081-1088
19. Tasnim S. H., Shohel M.: "Mixed convection and entropy generation in a vertical annular space"; *Exergy, an International Journal*; V2, 2002, pp 373-379
20. Sahin A.Z.: "Second law analysis of laminar viscous flow through a duct subjected to constant wall temperature"; *Journal of heat transfer*, Vol: 120, feb 1998, pp 76-83
21. Sahin A.Z.: "The entropy generation in turbulent flow through a smooth duct subjected to constant wall temperature"; *International journal of Heat and Mass Transfer*, Vol: 43, 2000, pp 1469-1478
22. San J.Y., Worek W.M., Lavan Z.: "Entropy generation in combined heat and mass transfer"; *International journal of heat and mass transfer*, V30, n7, pp1359-1369, 1987
23. Tasnim S. H., Shohel M.: "Entropy generation in a vertical concentric channel with temperature dependent viscosity"; *Int. Comm. Heat and Mass transfer*, Vol. 29, No.7, pp 907-918,2002
24. Chin-Hsiang Cheng and Wei-Ping Ma, Wen-Hsiung Huang : "Numerical predictions of entropy generation for mixed convective flows in a vertical channel with transverse fin array"; *International Comm. In Heat and Mass Transfer*, Vol.21, N4, 1994, pp 519-530

25. Sara O.N., Yapici S., Yilmaz M., Pekdermir T. : “Second law analysis of rectangular channels with square pin-fins”; *International Comm. in Heat and Mass Transfer*, Vol.28, N5, pp 617-630,2001
26. Shohel M., Roydon A. F.: “Analysis of mixed convection-radiation in a vertical channel: entropy generation”; *Exergy, an International journal*, V2, 2002, pp 330-339
27. Shohel M., Roydon A. F.: “Thermodynamic analysis of flow and heat transfer inside channel with two parallel plates”; *Exergy, an International journal*, V2, 2002, pp 140-146
28. Yilbas B.S., Shuja S.Z, Gbadebo S.A, Abu Al-Hamayel H.I, and Boran K.: “Natural Convection and entropy generation in a square cavity”; *International Journal of Energy Research*, V22, pp 1275-1290, 1998.
29. Baytas A.C.: “ Entropy generation for natural convection in an inclined porous cavity”; *Int Journal of Heat and Mass transfer*, Vol. 43, 2000, pp 2089-2099.
30. Shuja S.Z., Yilbas B.S., and Iqbal M.O.: “Mixed convection in a square cavity due to heat generating rectangular body, effect of exit port locations”; *Int journal of Numerical methods for Heat and Fluid flow*, Vol.10, No.8,2000, pp 824-841.
31. Magherbi M, Abbassi H, Ben Brahim A: “Entropy generation at the onset of natural convection”; *Int Journal of Heat and Mass transfer*, V 46,2003, pp 3441-3450.
32. Shohel M., Sadrul Islam A.K.M.: “Laminar free convection and entropy generation inside an inclined wavy enclosure”; *Int Journal of Thermal Sciences*, V42, 2003, pp 1003-1012.

33. Budair M.O: “Entropy analysis of unsteady flow on flat plate”; *International journal of Energy Research*, V25, 2001, pp 519-524.
34. Bassam A/K Abu-Hijleh: “Entropy generation in laminar convective from an isothermal cylinder in cross flow”; *Energy*, V23 n10, pp 851-871, 1998.
35. Abu Hijleh B. A/K, Abu Qudais M. And Abu Nada E.: “Entropy generation due to laminar natural convection from a horizontal isothermal cylinder”; *Journal of heat transfer*, V120, pp 1089-1090, November-1998.
36. Bassam A.K. Abu Hijleh, Waleed N. Heilen: “Entropy generation due to laminar natural convection over a heated rotating cylinder”; *International journal of heat and mass transfer*, V42 pp 4225-4233, 1999.
37. Abu-Hijleh B. A/K: “Entropy generation due to cross flow heat transfer from a cylinder covered with an orthotropic porous layer”; *Heat and mass transfer*, V39, pp 27-40, 2002.
38. Bassam A/K Abu-Hijleh: “Optimised use of baffles for reduced natural convection heat transfer from a horizonatal cylinder”; *International journal of Thermal Sciences*, V42, 2003, pp 1061-1071.
39. Haddad O.M., Abu-Qudias M. and Abu-Hijleh B.A/K, Maqableh A.M.: “Entropy generation due to laminar forced convection flow past a parabolic cylinder”; *International journal of numerical methods for heat and fluid flow*, V10 n7, pp 770-779, 2000.
40. Ishwar K.Puri: “Second law analysis of convective droplet burning”; *Journal of Heat and mass Transfer*, V35, n10, pp 2571-2578, 1992.

41. Carrington C.G. And Sun Z.F.: “Second law analysis of combined heat and mass transfer in internal and external flows”; *International journal of heat and fluid flow*, V13, n1, March 1992.
42. Shuja S.Z., Yilbas B.S., Budair M.O and Hussaini I.S.: “Entropy analysis of a flow past a heat generated bluff body”; *International journal of energy research*, V23, pp1133-1142, 1999.
43. Shuja S.Z, Yilbas B.S. and Budair M.O.: “Vortex shedding over a rectangular cylinder with ground effect: flow and heat transfer characteristics”; *International journal of numerical methods for heat and fluid flow*, V12, n8, pp916-939, 2002.
44. Lin W.W and Lee D.J.: “Second law analysis on a flat plate-fin array under crossflow”; *Int. Comm. Heat and Mass transfer*, Vol.27, Issue 2, 2000, pp 179-190.
45. Shuja S.Z., Yilbas B.X., Iqbal M.O., Budair M.O. : “Flow through a protruding bluff body- heat and irreversibility analysis”; *Exergy, an international Journal*, Vol 1, N 3, 2001, pp 209-215.
46. Antar M.A.: “Analysis of fluid flow and heat transfer around and inside a liquid sphere”; *Ph.D. dissertation*, KFUPM, 1996.
47. Bejan A.: “Entropy generation minimization”; *CRC Press Inc*, 1995.
48. Milne-Thomson L.M., “Theoretical Hydrodynamics”, fifth edition, *Macmillan and Co.*, London,1968.
49. Schlichting, “Boundary layer theory”, seventh edition, McGraw Hill, 1987

50. Bejan A., Fowler A.J.: "Correlation of optimal sizes of bodies with external forced convection heat transfer"; Int comm. Heat and mass transfer, Vol 21, 1994, pp17-27.
51. Paoletti S., Rispoli F., Sciubba E.: "Calculation of exergetic losses in compact heat exchanger passages"; ASME AES 10, 1989, pp 21-29.

Curriculum Vitae

Name: Mohammed Gayazullah

Place of Birth: Hyderabad, India

Date of Birth: 03 Dec, 1979

Religion: Islam

Major Field: Mechanical Engineering

Date of Bachelors Degree: May, 2001

Date of Masters Degree: December, 2004